Search for Lepton Flavour Violation with the H1 Experiment at HERA

Dissertation

zur

Erlangung der naturwissenschaftlichen Doktorwürde
(Dr. sc. nat.)

vorgelegt der

Mathematisch-naturwissenschaftlichen Fakultät

der

Universität Zürich

von

Linus Lindfeld

aus

Deutschland

Promotionskomitee

Prof. Dr.	Peter Truöl	(Vorsitz)
Prof. Dr.	Ulrich Straumann	(Leitung der Dissertation)
Dr.	Katharina Müller	
Dr.	Stefan Schmitt	

Zürich, 2006

Kurzfassung

Diese Arbeit stellt eine Suche nach einer Verletzung der im Standardmodell verankerten Leptonen-Familienzahlerhaltung durch Leptoquarks in Elektron-Proton-Streuung mit einer Schwerpunktsenergie von $319\,\mathrm{GeV}$ bei HERA vor. Hierbei werden Endzustände mit einem Muon oder Tau Lepton und einem hadronischen Jet in einem Datensatz gesucht, der in den Jahren 1998-2000 mit dem H1 Experiment aufgezeichnet wurde und einer Luminostät von $66.5\,\mathrm{pb}^{-1}$ für e^+p Kollisionen und $13.7\,\mathrm{pb}^{-1}$ for e^-p Kollisionen entspricht. Es wurde keine signifikante Abweichung vom Standardmodell durch eine Verletzung der Leptonen-Familienzahlerhaltung entdeckt. Daraufhin konnten Ausschlussgrenzen für die Kopplung von Leptoquarks an ein Muon-Quark- oder Tau-Quark-Paar innerhalb einer Erweiterung des effektiven Modells von Buchmüller-Rückl-Wyler gesetzt werden. Kopplungen, entsprechend der elektromagnetischen Kopplung von der Stärke 0.3, zwischen einem Leptoquark mit einer Masse bis zu $453\,\mathrm{GeV}$ $(371\,\mathrm{GeV})$ und einem Muon-Quark-Paar (Tau-Quark-Paar) können, abhängig vom Leptoquarktyp, zu 95% ausgeschlossen werden.

Abstract

This thesis presents a search for lepton flavour violating processes mediated by leptoquarks in electron-proton collisions at a centre-of-mass energy of $319\,\mathrm{GeV}$ with the H1 experiment at HERA. Final states with a muon or a tau and a hadronic jet are searched for in a data sample collected in the period 1998-2000 corresponding to an integrated luminosity of $66.5\,\mathrm{pb}^{-1}$ for e^+p collisions and $13.7\,\mathrm{pb}^{-1}$ for e^-p collisions. No evidence for lepton flavour violation is found. Limits are derived on the coupling of leptoquarks to a muon or tau and a light quark in an extension of the Buchmüller-Rückl-Wyler effective model. Models with leptoquark masses up to $453\,\mathrm{GeV}$ $(371\,\mathrm{GeV})$ and a coupling of electromagnetic strength ($\lambda = 0.3$) between a leptoquark and a muon-quark pair (tau-quark pair) can be excluded at 95% confidence level depending on the leptoquark type.

Contents

Chapter 1

Introduction

During the 1970's, the most successful theory describing almost all phenomena in particle physics that were known at that time was developed, the so-called *Standard Model* (SM) of particle physics. With the SM particle physicists had been able to predict the outcome of a large variety of experiments which were performed in the meantime. Except for the predicted Higgs boson, all particles included in the SM have been discovered and no "exotic" particle has been found so far. The SM is still the theory of our current understanding of fundamental particles and their interactions. It is a quantum field theory consistent with both quantum mechanics and special relativity incorporating strong, weak, and electromagnetic fundamental forces.

However, there is one large piece completely missing, the gravitational force. The SM also holds some principle deficiencies and unexplained symmetries. One of these unaccounted symmetries corresponds to lepton flavour conservation which is experimentally observed but not supported by an underlying gauge symmetry. It is also unclear why quarks and leptons both come in three flavours and why quarks have fractional lepton charges of $1/3$ or $2/3$.

As a consequence, the SM is believed to be an effective theory of some superior concept. Since the outcome of the SM, many theories extending the SM have been developed, e.g. grand unified theories (GUT), technicolour or composite models. All these theories give up lepton flavour conservation in one way or another and incorporate new particles interrelating quarks and leptons which will be called *leptoquarks* in this thesis. Leptoquarks must be very heavy, because a light leptoquark would induce a rapid decay of the stable proton. If they exist, they may induce lepton flavour violation (LFV). Although LFV has been observed in neutrino oscillations already, a direct observation of LFV in rare processes at a high-energy collider would clearly represent evidence for new physical phenomena beyond the SM.

Numerous searches for these heavy exotic particles have been performed so far without having discovered a hint for leptoquarks yet. This thesis presents a search for LFV processes which are mediated by leptoquarks in ep collisions at the high-energy collider HERA at DESY in Hamburg, Germany. The HERA collider, as the only electron-proton collider in the world, is ideally suited to search for leptoquarks which might be resonantly produced in the hard scattering subprocess between the electron and a quark of the proton.

The data analysed in this work are recorded with the H1 detector and cover an integrated luminosity of $66.5\,\mathrm{pb}^{-1}$ for e^+p collisions and $13.7\,\mathrm{pb}^{-1}$ for e^-p collisions. This data is the first HERA data that was taken at a centre-of-mass energy of $319\,\mathrm{GeV}$. The increased centre-of-mass energy and the significantly higher luminosity compared to the previous data taking periods guarantee a unique sensitivity for very high leptoquark masses. The analysis of both e^+p and e^-p collisions is sensitive for all leptoquark types which are classified in the Buchmüller-Rückl-Wyler (BRW) effective model.

This search concentrates on two scenarios in which a leptoquark decays into either a muon-quark pair or a tau-quark pair. In the former case a LFV transition $e \to \mu$ is mediated and a high-p_T muon and a high-p_T jet are expected in the final state. Transitions of $e \to \tau$ require a more sophisticated study as tau leptons are very short-lived and decay before reaching active detector components. The tau channel is therefore split up into an electronic, a muonic and a hadronic subchannel corresponding to the main tau decay modes in which the individual characteristic topologies are searched for.

The results of this analysis compete with results from low-energy experiments and other collider experiments such as LEP and TEVATRON. In particular the results are compared with those from previous searches at the HERA experiments H1 and ZEUS. With increased luminosity and higher centre-of-mass energy in combination with improved analysis methods the results of this work supercede limits derived in previous searches for LFV at the H1 experiment.

The outline of this thesis is as follows:

- The basic concepts of the SM are introduced with a focus on ep collisions in Ch. 2. The phenomenology of leptoquarks that may be resonantly produced in ep collisions and may mediate LFV is explained here in detail.
- The setup of the H1 experiment at the ep collider HERA is described in Ch. 3.
- Ch. 4 explains the general data analysis that is performed in preparation for the dedicated search. Data quality, trigger selection and efficiencies, reconstruction, calibration and the simulation of SM background and LFV signal processes are covered aspects here.
- Ch. 5 bears the performed selection steps to search for muon-quark pairs in ep collisions. The results are given and the signal selection efficiency is studied in detail.
- The most challenging part of the analysis, the efficient identification of tau leptons in ep collisions, is presented in Ch. 6. The search results for tau-quark pairs and selection efficiencies can be found in three exclusive tau decay channels.
- The interpretation of the search results in terms of exclusion limits is given in Ch. 7. Exclusion limits for various scenarios of ep processes including a leptoquark which induces LFV are determined.

Chapter 2

Theory

This chapter starts with a brief overview of the theoretical description of particle physics in the framework of the Standard Model (SM). After an introduction to the elementary particles and their interactions, attention is turned to the SM processes in ep collisions. Despite the remarkably successful description of nature by the SM some deficiencies are presented which provide motivation for searches for new physics. Theoretical concepts beyond the SM are introduced potentially solving problems and insufficiencies of the SM. All these theories incorporate leptoquarks and lepton flavour violation in one way or another. The attributes of leptoquarks are discussed in the general effective model by Buchmüller-Rückl-Wyler [1]. The last part of this chapter deals with the hypothetical existence of a leptoquark mediating lepton flavour violation and its consequences for ep scattering. Finally, existing limits on lepton flavour violating processes from dedicated low-energy experiments are presented.

2.1 Fundamentals of the Standard Model

2.1.1 Symmetries

Nowhere more than in the theoretical understanding of particle physics are symmetries and conservation laws of more importance. The invariance of physical laws under several operations is closely related to the concept of symmetry. Therefore, a physical system is characterised by the ensemble of transformations that leave it invariant. Equivalently, the corresponding set of conservation laws describes a system.

For example, the translational and rotational invariance in our space-time symmetric world implies the conservation of linear and angular momentum respectively. Concerning operations on elementary particles, there are also the discrete symmetries C (charge conjugation, i.e. particle↔antiparticle), P (parity, i.e. $\vec{x} \leftrightarrow -\vec{x}$) or T (time reversal, $t \leftrightarrow -t$). Known as the CPT-theorem, it is a basic principle of quantum field theory that physics is invariant under transformations through the product CPT. On the other hand, violations of individual symmetries like C, P or even CP are important ingredients of the SM. Further abstract transformations that leave the physical system invariant arose in numerous experiments to exhibit *internal* symmetries. The conservation of leptonic flavour number (LF) or baryon number (B) are examples of such internal symmetries.

2.1.2 Gauge invariance

Our current understanding of the fundamental interactions between elementary particles is described by quantum field theories (QFT). These QFTs, namely quantum electro dynamics (QED) and quantum chromo dynamics (QCD), make use of the concept of local gauge symmetry or invariance. Here, Lagrangians describing the theory must possess local symmetries valid in a particular region of space-time without affecting another region. For example, in QED one takes it as a fundamental assumption that the theory must be invariant under gauge transformations of the form

$$\Psi(\vec{x},t) \rightarrow \Psi'(\vec{x},t) = e^{iq\alpha(\vec{x},t)}\Psi(\vec{x},t), \tag{2.1}$$

where $\Psi(\vec{x},t)$ is the wavefunction of a particle of charge $\sqrt{\varepsilon_0}q$ and $\alpha(\vec{x},t)$ is an arbitrary continuous function. The solution of the equation of motion under gauge invariance requires the existence of an interaction. This approach, in which the form of the interaction terms needed to make the equation of motion gauge invariant, is called the *principle of minimal gauge invariance*, or the *gauge principle* for short. As a consequence of this, an extra massless quantum field is added to the Lagrangian in QED which describes the gauge boson called the photon.

In the SM, the electromagnetic, weak and strong interactions are explained by a mediation of gauge bosons, i.e. vector particles, corresponding to a gauge symmetry. Comparatively small at subatomic scales, the gravitational force is the only known fundamental interaction that is not incorporated in the SM.

The gauge symmetry group $SU(2)_L \times U(1)_{Y^W}$ unifies the electromagnetic and weak interactions (*electroweak*), where L is the weak isospin and Y^W is the weak hypercharge. As an adjoint representation of $SU(2)_L \times U(1)_{Y^W}$ the intermediate weak bosons $W_\mu^\pm$, W_μ^0 ($SU(2)_L$) and B_μ ($U(1)_{Y^W}$) arise and mix via the Weinberg angle θ_W to form the massive weak bosons $W^\pm$, Z^0 and the massless electromagnetic photon γ. The broken symmetry due to the mass differences between these bosons is discussed below.

The exact $SU(3)_C$ symmetry (C stands for colour) describes the strong interaction introducing 8 different massless gluons as carriers of the strong force. The SM symmetry group is therefore often referred to as

$$SU(3)_C \times SU(2)_L \times U(1)_Y. \tag{2.2}$$

fermions	generation			Rep. []	Rep. []	Q	Y^W	T	T_3
	1	2	3	$SU(3)_C$	$SU(2)_L$				
leptons	ν_{eL}	$\nu_{\mu L}$	$\nu_{\tau L}$	1	2	0	-1	1/2	1/2
	e_L	μ_L	τ_L			-1	-1	1/2	$-1/2$
	e_R	μ_R	τ_R	1	1	-1	-2	0	0
quarks	u_L	c_L	t_L	3	2	2/3	1/3	1/2	1/2
	d'_L	s'_L	b'_L	3	2	$-1/3$	1/3	1/2	$-1/2$
	u_R	c_R	t_R	3	1	2/3	4/3	0	0
	d_R	s_R	b_R	3	1	$-1/3$	$-2/3$	0	0

force	bosons	J	Q	m (GeV)
electromagnetic	γ	1	0	0
weak	$W^{\pm}$	1	± 1	80.45
	Z^0	1	0	91.18
strong	gluons g_i $(i=1..8)$	1	0	0
Higgs field	Higgs boson H^0	0	0	> 114.4

TABLE 2.1: Fundamental interactions and particles with their quantum numbers in the SM. For the fermions, Y^W denotes the weak hypercharge, T and T_3 are the weak isospin and its third component respectively. The electrical charge Q is given by $Q = T_3 + \frac{Y}{2}^W$. For the bosons, the mass m and the quantum numbers spin J and electrical charge Q are given. The mass of the Higgs boson refers to a lower limit at 95% confidence level from a direct search [2].

2.1.3 Particles and interactions

The matter itself consists of fermions, i.e. spin 1/2 particles, which form a fundamental representation of the gauge groups in Eq. (2.2). There are two types of fermions, called quarks and leptons, each classified in three generations, also known as *flavours*. Leptons (electrons, muons, taus and neutrinos) do not interact strongly whereas quarks feel the strong force. As the weak interaction violates the symmetry of parity P, left-handed and right-handed representations of the fermions have different quantum numbers. Left-handed fermions are arranged in weak isodoublets whereas right-handed fermions form singlets. Assuming massless neutrinos they have only a left-handed representation. Tab. 2.1 summarises the fundamental interactions and particles with their quantum numbers in the SM.

The existence of flavour changing weak interactions between quarks leads to a non-diagonal unitary quark mixing matrix, the so-called CKM[1] matrix, $V_{\rm CKM}$. By convention, the mixing

---

[1] named after N. **C**abibbo, M. **K**obayashi and T. **M**askawa [3]

acts only on *down-type* quarks:

$$\begin{pmatrix} d' \\ s' \\ b' \end{pmatrix} = V_{\mathrm{CKM}} \begin{pmatrix} d \\ s \\ b \end{pmatrix} = \begin{pmatrix} V_{ud} & V_{us} & V_{ub} \\ V_{cd} & V_{cs} & V_{cb} \\ V_{td} & V_{ts} & V_{tb} \end{pmatrix} \begin{pmatrix} d \\ s \\ b \end{pmatrix} . \tag{2.3}$$

As already mentioned above, the $SU(2)_L$ symmetry is spontaneously broken, because the bosons of the weak interaction $W^{\pm}$ ($m = 80.5\,\mathrm{GeV}$) and Z^0 ($m = 91.2\,\mathrm{GeV}$) are massive in contrast to the massless photon. At energies well below the electroweak unification scale, the electromagnetic and weak interactions are distinguishable. At high energies, the electroweak symmetry is asymptotically restored.

Since mass terms are not invariant under $SU(2)_L$, the SM symmetry must be broken to give masses to the quarks, leptons and massive weak gauge bosons we observe. Therefore, an additional term is added to the Lagrangian which leads to a non-zero vacuum expectation value (vev). The parameters of the vev can be chosen such that a new massive spinless neutral Higgs boson H^0 couples to weak gauge bosons and fermions according to their mass while keeping the massless photon. The last row of Tab. 2.1 holds some characteristics of the Higgs boson.

As the Higgs boson is the only particle in the SM that is not yet directly discovered, the Higgs mass is still a free parameter of the theory. The actual lower limit at 95% confidence level (CL) on the Higgs mass from direct searches at the LEP collider is $114.4\,\mathrm{GeV}$ [4]. Indirect experimental bounds for the SM Higgs boson mass are obtained from fits to precision measurements of electroweak observables, and to the measured top-quark and W masses. The current best value is $m_{H^0} = 96^{+60}_{-36}\,\mathrm{GeV}$, or an upper limit of $m_{H^0} < 219\,\mathrm{GeV}$ at the 95% CL [2].

2.1.4 Lepton flavour

In an elementary particle interaction the lepton number is the number of participating leptons minus the number of participating antileptons, in equation form:

$$L = n_l - n_{\bar{l}}. \tag{2.4}$$

Moreover, the leptonic flavour[2] numbers L_e, L_μ and L_τ are defined as

$$\begin{aligned} L_e &= n_e + n_{\nu_e} - n_{\bar{e}} - n_{\bar{\nu}_e} \\ L_\mu &= n_\mu + n_{\nu_\mu} - n_{\bar{\mu}} - n_{\bar{\nu}_\mu} \\ L_\tau &= n_\tau + n_{\nu_\tau} - n_{\bar{\tau}} - n_{\bar{\nu}_\tau}. \end{aligned} \tag{2.5}$$

As an internal symmetry in the SM, the leptonic flavour numbers are individually conserved for each of the three lepton flavours. The mixing matrix V_{MNS}[3] is therefore the unity matrix.

---

[2] also: family

[3] named after Z. **M**aki, M. **N**akagawa and S. **S**akata [5]

It should be noted that no underlying gauge symmetry could yet be brought into relation with the conservation of lepton flavour. That's why most theories beyond the SM give up lepton flavour as a fundamental quantum number (Sec. 2.4).

In fact, this conservation law in the SM holds only under the assumption of massless neutrinos. Since 1998 [6, 7], there is strong evidence for neutrino oscillations inferring non-zero neutrino masses and a mixing mechanism similar to the CKM mixing. Nevertheless, the smallness of experimental upper bounds on neutrino masses, i.e. $m_{\nu_e} < 3\,\mathrm{eV}$, $m_{\nu_\mu} < 0.19\,\mathrm{MeV}$, $m_{\nu_\tau} < 18.2\,\mathrm{MeV}$ [2], imply very small effects on lepton flavour violation in charge lepton decays [8] as well as in neutral current deep-inelastic scattering (NC DIS, Sec. 2.2). As the lepton flavour violating (LFV) effects due to neutrino mixing are consistent with the experimental upper bounds, a non-unity matrix V_{MNS} is regarded as a SM extension rather than being contradictory to the SM.

Therefore, any direct observation of LFV processes in charged lepton decays or DIS would clearly represent an evidence for new physical phenomena beyond the SM.

2.2 SM processes in ep collisions

Collider experiments like the ones at the electron[4]-proton storage ring HERA[5] investigate matter and its interactions by particle scattering. In electron-proton scattering the beam electron interacts with a parton from the proton by exchange of a gauge boson. If the virtuality, Q^2, of the exchanged gauge boson is large enough to resolve the quark structure of the proton, the process is called deep-inelastic scattering (DIS). In case of a γ or Z^0 boson exchange, the outgoing lepton is the scattered electron and the process is called neutral current (NC) DIS, in charged current (CC) DIS a $W^\pm$ boson is exchanged and an electron-neutrino is the lepton in the final state. Fig. 2.1 illustrates the DIS processes in ep scattering in the form of a Feynman diagram. If a quasi-real photon is exchanged, $Q^2 \approx 0$, the process is usually referred to as photoproduction (γp).

2.2.1 Kinematics

The kinematics of a scattering process is the ensemble of Lorentz-invariant kinematic variables which are used to describe the cross section. In the following the four-momenta of the incident (outgoing) leptons are denoted as k (k'), as can also be seen in Fig. 2.1. If the exchanged gauge boson has a four-momentum of q and the proton enters the interaction with four-momentum

---

[4] here and in the following the term *electron* refers to electrons or positrons as HERA can operate in either mode. Distinction will be made explicit when required.

[5] **H**adron-**E**lektron-**R**ing-**A**nlage

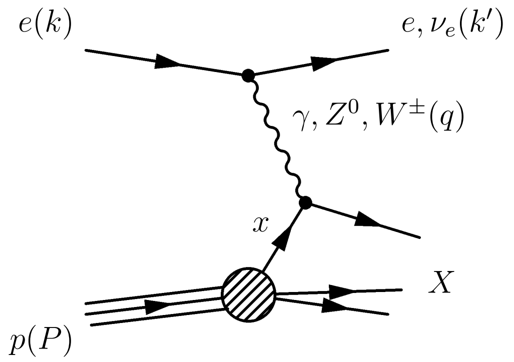

FIGURE 2.1: Tree level Feynman diagram of NC/CC DIS in ep collisions. The four-momenta of the incoming (outgoing) lepton e or ν_e are denoted by k (k'). P is the four-momentum of the proton p and x is the momentum fraction carried by the struck quark. X represents the hadronic final state. The exchanged gauge boson four-momentum is denoted by q.

P, a set of Lorentz-invariant kinematic variables can be defined as:

$$Q^2 = -q^2 = -(k-k')^2 \tag{2.6a}$$

$$W^2 = (P+q)^2 \tag{2.6b}$$

$$s = (P+k)^2 \tag{2.6c}$$

$$x = \frac{Q^2}{2Pq} \tag{2.6d}$$

$$y = \frac{Pq}{Pk} = \frac{1}{2}(1+\cos\theta^*)\ . \tag{2.6e}$$

Here, the negative squared momentum transfer Q^2 represents the virtuality of the gauge boson. W^2 is the squared centre-of-mass energy of the boson-proton subsystem. The ep centre-of-mass energy, $\sqrt{s}$, depends only on the initial particle energies delivered by the storage ring and can be approximated by

$$\sqrt{s} \approx \sqrt{4E_eE_p} \approx \sqrt{4\cdot 27.5\,\mathrm{GeV}\cdot 920\,\mathrm{GeV}} \approx 319\,\mathrm{GeV}\ , \tag{2.7}$$

where mass terms are neglected.

The variable y and the Bjørken scaling variable x are dimensionless and range between 0 and 1. y can be interpreted as the relative energy transfer to the proton in its rest frame and is often referred to as the inelasticity of the process. It can also be expressed by the polar scattering angle θ^* of the electron[6] in the ep centre-of-mass frame[7].

---

[6] at the H1 experiment the polar scattering angle θ is defined with respect to the direction of the initial proton momentum, i.e. the positive z-axis.

[7] in case of inelastic ep scattering the centre-of-mass of the hard subprocess between the electron and the parton from the proton must be considered.

In the Quark-Parton model (QPM) [9], x is understood as the fraction of the proton momentum that is carried by the struck parton or quark. The proton rest frame is interpreted as an infinite momentum frame in which the three quarks share the proton momentum and act as free particles. This mechanism is known as asymptotic freedom [10].

At lowest order, DIS ep scattering is therefore a two-body process between an electron and a quark. Thus, with the constraint of energy conservation two Lorentz-invariant variables are sufficient to describe the kinematics. Usually x and Q^2 are the preferred choice. Neglecting mass terms in comparison to a centre-of-mass energy of $319\,\mathrm{GeV}$, important relations follow:

$$Q^2 = xys \tag{2.8a}$$

$$W^2 = \frac{Q^2}{x} - Q^2 \,. \tag{2.8b}$$

With the help of the uncertainty principle one can interpret the squared momentum transfer as spatial resolution power. The centre-of-mass energy squared s is a kinematical upper limit for Q^2. At HERA, the highest accessible Q^2 domain is $\sim 3 \cdot 10^4\,\mathrm{GeV}^2$ which corresponds to a spatial resolution of $10^{-18}\,\mathrm{m}$. That makes HERA to the top-performing microscope in the world.

2.2.2 The ep cross section

At momentum transfers $Q^2 \ll m^2_{Z^0}$ the propagator terms $1/(Q^2 + m^2_{Z^0})^2$ (pure Z^0 exchange) and $Q^2/(Q^2 + m^2_{Z^0})$ (γ/Z^0 interference) are sufficiently small to consider the γ exchange only. With this approximation, the double differential cross section for NC DIS processes in ep scattering is given by

$$\frac{d^2\sigma^{\pm}_{NC}}{dxdQ^2} = \frac{2\pi\alpha^2}{xQ^4}\left[y^2xF_1 + (1-y)F_2\right], \tag{2.9}$$

where F_1 and F_2 are proton structure functions depending on x and Q^2. α is the fine structure constant. The Callan-Gross relation [11] applies in *leading-log* approximation for spin 1/2 partons like quarks in the QPM:

$$2xF_1 = F_2 \;\Leftrightarrow\; F_L \equiv F_2 - 2xF_1 = 0 \,. \tag{2.10}$$

The parton density function (PDF), often denoted as $q_i(x, Q^2)$, is defined as the probability density of finding a parton of type i with a momentum fraction x at a scale Q^2. The structure functions F_1 and F_2 can be expressed in leading order and for not too small values of Q^2 by sums of quark and antiquark PDFs:

$$F_1(x, Q^2) = \frac{1}{2}\sum_i e_i^2(q_i(x, Q^2) + \bar{q}_i(x, Q^2)) \tag{2.11a}$$

$$F_2(x, Q^2) = x\sum_i e_i^2(q_i(x, Q^2) + \bar{q}_i(x, Q^2)) \,. \tag{2.11b}$$

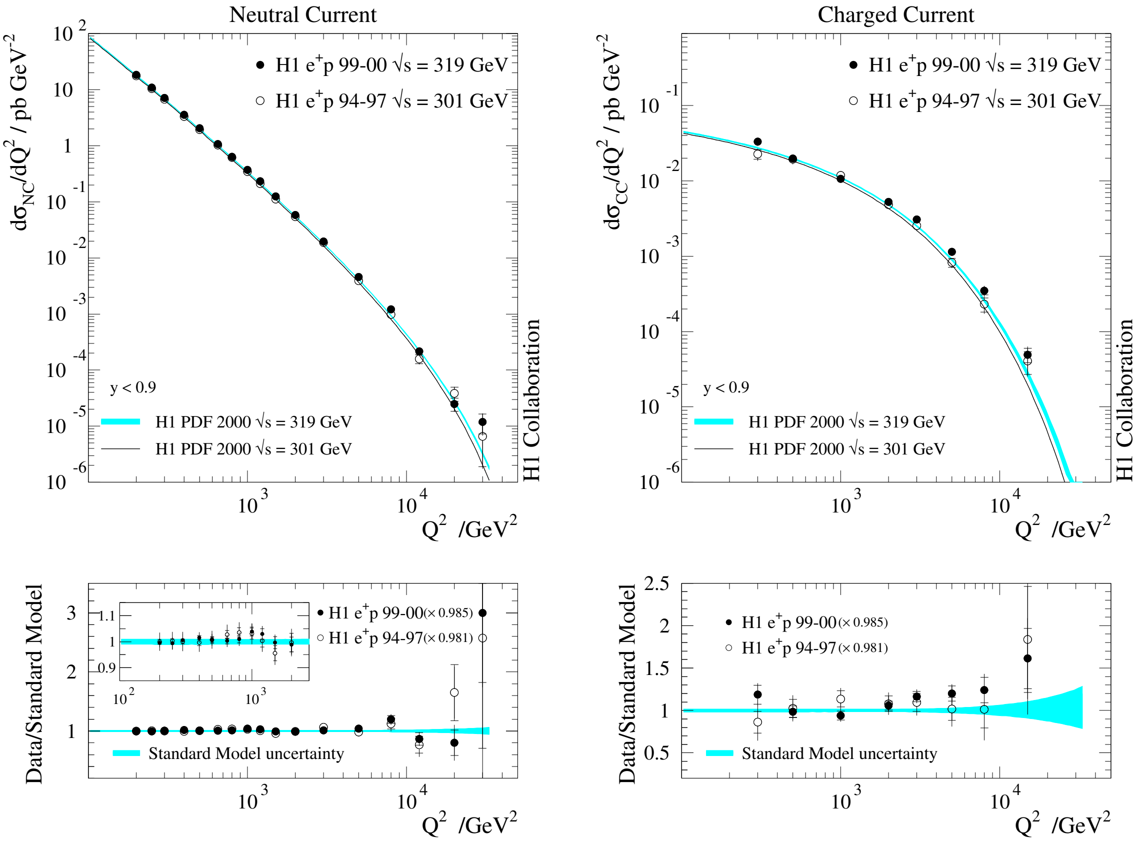

FIGURE 2.2: H1 measurements of NC/CC DIS cross sections [13].

It should be noted that next-to-leading order (NLO) QCD calculations that go beyond the naïve QPM allow for non-zero values of the longitudinal structure function F_L which become noticeable in processes with low Q^2 and high y. For processes with $Q^2 > 5000\,\mathrm{GeV}^2$ the effects of the Z^0 exchange become important and the generalised structure functions $\tilde{F}_2$, $\tilde{F}_3$ and $\tilde{F}_L$ must be used [12].

In analogy to Eq. (2.9), the CC DIS cross section involving the exchange of a massive $W^\pm$ boson can be written double differentially in the QPM with $F_L \equiv 0$ as:

$$\frac{d^2\sigma^{\pm}_{CC}}{dxdQ^2} = \frac{G_F^2}{2\pi x}\left(\frac{m_W^2}{m_W^2+Q^2}\right)^2 \times \begin{cases} x(\bar{u}+\bar{c}) + (1-y)^2 x(d+s) & \text{for } e^+p \\ x(u+c) + (1-y)^2 x(\bar{d}+\bar{s}) & \text{for } e^-p \end{cases}, \tag{2.12}$$

with G_F as Fermi constant and u, c, d, s ($\bar{u}$, $\bar{c}$, $\bar{d}$, $\bar{s}$) as the relevant (anti)quark PDFs[8].

---

[8] No significant contribution from top or bottom content in the proton is assumed. Below the charm threshold, d and $\bar{d}$ (s and $\bar{s}$) in Eq.(2.12) must be multiplied by $\cos^2\theta_c$ ($\sin^2\theta_c$), where θ_c is the Cabibbo mixing angle.

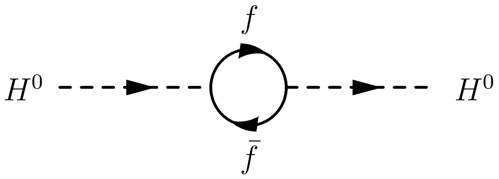

FIGURE 2.3: Feynman diagram for the divergent one-loop correction to the Higgs field. After renormalisation, the Higgs boson mass m_{H^0} depends quadratically on a cut-off scale Λ. The largest contribution comes from top-quark loops.

The measurement of NC and CC cross sections in ep scattering can therefore be used to determine the PDFs in the proton. The most popular theory groups extracting PDFs from cross section measurements are MRS [14] and CTEQ [15].

As an example for a NC and CC DIS cross section measurement, Fig. 2.2 shows results of the H1 experiment at HERA published in 2003 [13]. At low momentum transfers Q^2, the CC cross section is strongly suppressed with respect to the NC cross section. At values of Q^2 above the Z^0 boson mass squared, i.e. $\mathcal{O}(10^4\,\mathrm{GeV}^2)$, the same order in cross section for NC and CC is measured. The good agreement with the SM is shown in the lower plots.

2.3 Limitations of the SM

Despite the tremendous success of the SM in describing a vast range of experimental observations, the SM includes some principle deficiencies. Viewing Tab. 2.1 one can see that the SM depends on a fairly large number of free parameters, namely 18 (neglecting neutrino masses):

- the fine structure constant α, the Fermi constant G_F and the Z^0 mass m_{Z^0}
- the running strong coupling constant $\alpha_S(m_{Z^0})$ or the QCD-scale Λ_{QCD}
- the lepton masses m_e, m_μ, m_τ
- the quark masses m_u, m_d, m_s m_c, m_t, m_b
- the three phases of the CKM matrix and one CP-violating phase
- the Higgs mass m_{H^0}

Further constants in nature are the speed of light c, Planck's constant $\hbar$ and the gravitational constant G. Even with its 18 parameters, 24 fermions[9] and 12 gauge bosons the SM does not make any predictions for the effects of gravity. These become important at the Planck scale $E_{Pl} = \sqrt{\hbar c/G_F} \simeq 10^{19}\,\mathrm{GeV}$ which corresponds to a distance of $10^{-35}\,\mathrm{m}$.

---

[9] taking the quark colour into account

Another insufficiency of the SM is called the *hierarchy problem*. The scalar Higgs field contains divergent one-loop corrections as depicted in Fig. 2.3. After renormalisation, the corrected Higgs mass depends quadratically on a cut-off scale Λ:

$$m_{H^0}^2 = m_0^2 - \frac{|\lambda_f|}{8\pi^2}\Lambda^2 + \mathcal{O}(\ln\frac{\Lambda}{m_f^2}), \tag{2.13}$$

where m_f denotes the fermion mass, the Higgs-fermion coupling is λ_f and m_0 stands for the uncorrected Higgs mass. The hierarchy problem manifests itself in the enormous Higgs mass if a cut-off scale in the range of the Planck scale is used. This is in contradiction with electroweak precision measurements suggesting a Higgs mass m_{H^0} around the electroweak scale.

One could also argue that the first two terms in Eq. (2.13) could cancel to give a low Higgs mass m_{H^0}. For such a cancellation to work, the uncorrected Higgs mass squared m_0^2 would have to equal the second term in the equation at the level of 10^{-24}. This is extremely unlikely and it is in disagreement with the naturalness of the theory (*fine-tuning* or *naturalness problem*).

There are also still experimental observations which cannot be explained by the SM. A variety of cosmological observations suggest the existence of so-called *dark matter* in the universe, but the SM does not comprise a particle candidate for it.

Last but not least, there are unaccounted symmetries between the lepton sector and the quark sector. Although completely separated in the SM, both leptons and quarks come in three families. It is also a remarkable coincidence that the quark charge value is exactly $1/3$ or $2/3$ of the lepton charge. To questions like these the SM may only respond with a truism called the anthropic principle which states that if the properties of nature were different from those we observe, we would not exist such that we could observe them.

2.4 Leptoquarks and LFV

In view of its limitations and open questions, the SM is viewed as a low-energy effective theory of some superior concept. Most relevant here are for example:

- Pati-Salam's $SU(4)_C$ model [16], where lepton number is treated as a fourth colour;
- a grand unified theory (GUT) [17, 18, 19], where the SM gauge group is embedded in a larger symmetry group, e.g. $SU(5)$, $SO(10)$ or E_6;
- Technicolour [20, 21, 22, 23], solving the hierarchy problem by introducing new electroweak doublets and singlets (technifermions) as multiplets of a non-abelian gauge interaction (technicolour);
- Composite, or substructure, models [24, 25, 26] assuming quarks and leptons to be bound states of more fundamental particles (preons).

The symmetries between the quark sector and the lepton sector strongly suggest that in a theory more fundamental than the SM, leptons and quarks should be interrelated. Therefore, in all the SM extensions mentioned above one expects new particles which mediate quark-lepton transitions. Although these particles have sometimes different names in the individual theories, the comprehensive and suitable name *leptoquarks* (LQ) is a good choice.

The name of the leptoquarks is well suited, as they couple to both leptons and quarks via a coupling. In the picture of the SM they carry both baryon and lepton number. As the existence of light leptoquarks would cause a rapid proton decay, they must be heavy, i.e. $m_{\mathrm{LQ}} = \mathcal{O}(100\,\mathrm{GeV})$. For leptoquarks coupling directly to a quark-lepton pair they must be colour triplet bosons carrying fractional charge with either spin 0 (scalar) or spin 1 (vector).

For the description of leptoquarks it is useful to define a new quantum number, the so called *fermion number*, as

$$F \equiv |L + 3B| \,. \tag{2.14}$$

It should be noted that B is the baryon number and L is the lepton number, not to be mixed up with the lepton flavour number L_i. That means that leptoquarks with $F = 0$ couple to antilepton-quark pairs or lepton-antiquark pairs, whereas $F = 2$ leptoquarks couple to lepton-quark pairs and antilepton-antiquark pairs respectively.

It is possible to write down an effective Lagrangian for the fusion of an electron (or neutrino) with a u or d quark to illustrate a possible leptoquark signal at HERA. In this Lagrangian the most general dimensionless, $SU(3)_C \times SU(2)_L \times U(1)_Y$ invariant couplings of scalar (S) and vector (V) leptoquarks satisfy baryon and lepton number conservation [1]:

$$\mathcal{L} = \mathcal{L}_{F=2} + \mathcal{L}_{F=0} \,, \quad \text{with} \tag{2.15a}$$

$$\begin{aligned}\mathcal{L}_{F=2} =& \Big[\Big(\lambda_L^{S_0} \bar{q}_L^c i\tau_2 l_L + \lambda_R^{S_0} \bar{u}_R^c e_R \Big) S_0^\dagger + \Big(\lambda_R^{\tilde{S}_0} \bar{d}_R^c e_R \Big) \tilde{S}_0^\dagger + \\ & \Big(\lambda_L^{\tilde{S}_1} \bar{q}_L^c i\tau_2 \vec{\tau} l_L \Big) \vec{S}_1^\dagger + \\ & \Big(\lambda_L^{V_{1/2}} \bar{d}_R^c \gamma_\mu l_L + \lambda_R^{V_{1/2}} \bar{q}_L^c \gamma_\mu e_R \Big) V_{1/2}^\dagger + \Big(\lambda_L^{\tilde{V}_{1/2}} \bar{u}_R^c \gamma_\mu l_L \Big) \tilde{V}_{1/2}^\dagger \Big] + c.c. \,,\end{aligned} \tag{2.15b}$$

$$\begin{aligned}\mathcal{L}_{F=0} =& \Big[\Big(\lambda_L^{V_0} \bar{q}_L \gamma_\mu l_L + \lambda_R^{V_0} \bar{d}_R \gamma_\mu e_R \Big) V_0^\dagger + \Big(\lambda_R^{\tilde{V}_0} \bar{u}_R \gamma_\mu e_R \Big) \tilde{V}_0^\dagger + \\ & \Big(\lambda_L^{\tilde{V}_1} \bar{q}_L \vec{\tau} \gamma_\mu l_L \Big) \vec{V}_1^\dagger + \\ & \Big(\lambda_L^{S_{1/2}} \bar{u}_R l_L + \lambda_R^{S_{1/2}} \bar{q}_L i\tau_2 e_R \Big) S_{1/2}^\dagger + \Big(\lambda_L^{\tilde{S}_{1/2}} \bar{d}_R l_L \Big) \tilde{S}_{1/2}^\dagger \Big] + c.c. \,.\end{aligned} \tag{2.15c}$$

where rather than the original notation in [1] the so-called *Aachen notation* is used. The $SU(2)$ singlet, doublet and triplet leptoquarks respectively have subscripts 0, 1/2 and 1 according to their weak isospin. Members of each weak isospin doublet or triplet are assumed to be degenerate in mass. The index L/R reflects the lepton chirality, such that $\lambda_R^{S_0}$ is the coupling of S_0 to a right-handed electron and quark for example[10]. q_L and l_L are the left-handed quark and

---

[10] leptoquarks with couplings to both left-handed and right-handed leptons are experimentally constrained from searches for the process $\pi \to e\nu$ [27, 28, 29]

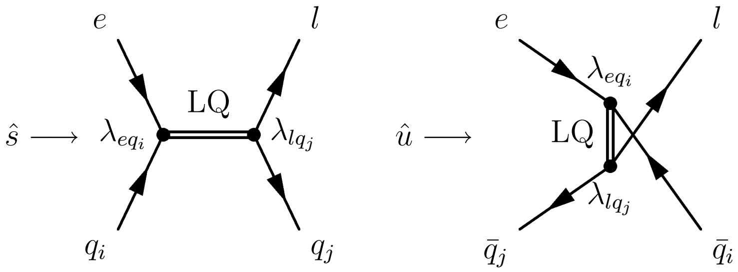

FIGURE 2.4: Left: s-channel resonant leptoquark production and decay to a lepton-quark pair. Right: u-channel exchange of a leptoquark. The indices i and j represent quark generation indices, such that λ_{eq_i} denotes the coupling of an electron to a quark of generation i, and λ_{lq_j} stands for the coupling of the outgoing lepton l to a quark of generation j. In case of of the outgoing lepton l being a muon or tau lepton, the leptoquark mediates LFV.

lepton doublets, and e_R, u_R and d_R are the right-handed electron, u and d quarks, respectively. The superscript c denotes the charge-conjugated fermion field.

One can see in Eqs. (2.15) that there are 10 different types of leptoquarks, of which 4 can have couplings to both lepton chiralities, namely S_0, $V_{1/2}$, V_0 and $S_{1/2}$. Following the Aachen notation, we distinguish between the leptoquarks coupling to a left-handed lepton and those coupling to a right-handed lepton as being of different type. In the following, a superscript corresponding to the lepton chirality is added to the leptoquark type.

In Tab. 2.2 the resulting 14 different leptoquark types are listed with their quantum numbers spin J, fermion number F and electrical charge Q. Also, the dominant production process in ep scattering with the corresponding coupling strength and branching ratio β_l is given. It is important to stress that $\beta_l = \Gamma_l/(\Gamma_l + \Gamma_{\nu_l})$ refers to the fraction of decays into charged leptons for one lepton generation.

The Lagrangian in Eqs.(2.15) can be easily extended such that a leptoquark also couples to another lepton generation. Such an extension would allow for LFV processes in ep collisions. In case of LFV, an additional LFV branching ratio β_{LFV} must be assumed to get an effective branching ratio BR with

$$\mathrm{BR} = \beta_l \times \beta_{LFV} \ , \ \text{ where } \beta_{LFV} = \frac{\Gamma_{\mu,\tau}}{\Gamma_{\mu,\tau} + \Gamma_e} \ . \tag{2.16}$$

The dominant resonant production processes listed in Tab. 2.2 show that $F = 2$ leptoquarks are most likely produced in e^-p collisions, whereas $F = 0$ leptoquarks are dominantly produced in e^+p collisions. The contribution of the charge conjugated processes, e.g. $e^+_L \bar{u}_L \to S^R_0 \to l^+ \bar{u}$, is strongly suppressed by less favourable parton densities of the sea-quarks in the proton.

As the electrical charge of a heavy, short-lived leptoquark is not directly observable at HERA, some leptoquark types can take different values of Q. In these cases, i.e. S^L_1, $V^R_{1/2}$, S^L_1

type	J	F	Q	ep dom. process	coupl.	β_l
S_0^L	0	2	$-1/3$	$e_L^- u_L \to l^- u$	λ_L	1/2
				$\nu_l d$	$-\lambda_L$	1/2
S_0^R	0	2	$-1/3$	$e_R^- u_R \to l^- u$	λ_R	1
$\tilde{S}_0^R$	0	2	$-4/3$	$e_R^- d_R \to l^- d$	λ_R	1
S_1^L	0	2	$-1/3$	$e_L^- u_L \to l^- u$	$-\lambda_L$	1/2
				$\nu_l d$	$-\lambda_L$	1/2
			$-4/3$	$e_L^- d_L \to l^- d$	$-\sqrt{2}\lambda_L$	1
$V_{1/2}^L$	1	2	$-4/3$	$e_L^- d_R \to l^- d$	λ_L	1
$V_{1/2}^R$	1	2	$-1/3$	$e_R^- u_L \to l^- u$	λ_R	1
			$-4/3$	$e_R^- d_L \to l^- d$	λ_R	1
$\tilde{V}_{1/2}^L$	1	2	$-1/3$	$e_L^- u_R \to l^- u$	λ_L	1
V_0^L	1	0	$+2/3$	$e_R^+ d_L \to l^+ d$	λ_L	1/2
				$\bar{\nu}_l u$	λ_L	1/2
V_0^R	1	0	$+2/3$	$e_L^+ d_R \to l^+ d$	λ_R	1
$\tilde{V}_0^R$	1	0	$+5/3$	$e_L^+ u_R \to l^+ u$	λ_R	1
V_1^L	1	0	$+2/3$	$e_R^+ d_L \to l^+ d$	$-\lambda_L$	1/2
				$\bar{\nu}_l u$	λ_L	1/2
			$+5/3$	$e_R^+ u_L \to l^+ u$	$\sqrt{2}\lambda_L$	1
$S_{1/2}^L$	0	0	$+5/3$	$e_R^+ u_R \to l^+ u$	λ_L	1
$S_{1/2}^R$	0	0	$+2/3$	$e_L^+ d_L \to l^+ d$	$-\lambda_R$	1
			$+5/3$	$e_L^+ u_L \to l^+ u$	λ_R	1
$\tilde{S}_{1/2}^L$	0	0	$+2/3$	$e_R^+ d_R \to l^+ d$	λ_L	1

TABLE 2.2: The 14 leptoquark types of the Buchmüller-Rückl-Wyler classification [1] in the Aachen notation. The leptoquark subscripts refer to the weak isospin and the superscripts account for the lepton chirality. Columns 2-4 give spin J, fermion number F and electrical charge Q. Following Eqs. (2.15), the dominant resonant production process in ep scattering and the corresponding coupling can be seen in columns 5 and 6 respectively. Leptoquarks coupling to a left-handed lepton doublet and which allow for a decay into a neutrino-quark pair under charge conservation, have a charged lepton decay branching ratio of $\beta_l = \Gamma_l/(\Gamma_l + \Gamma_{\nu_l}) = 1/2$.

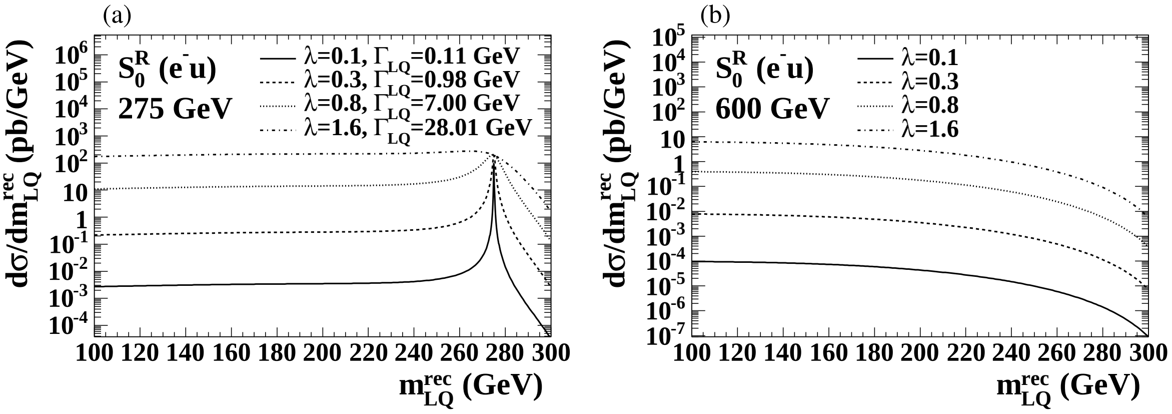

FIGURE 2.5: Examples for the cross section distribution of a scalar leptoquark versus the reconstructed leptoquark mass. (a) resonant production of a 275 GeV S_0^R for different coupling strengths $\lambda = \lambda_{eq} = \lambda_{lq}$. (b) virtual effects on the cross section distribution from a 600 GeV S_0^R.

and $S_{1/2}^R$, couplings to both up-type and down-type quarks exist and the resulting observable decay width for both charge values is equal (see Eq. (2.19)).

In a Feynman graph on the left-hand side of Fig. 2.4 the effective resonant s-channel leptoquark production process in ep scattering is illustrated. It shows only the relevant hard subprocess of the fusion between the electron and the quark of generation i carrying a proton momentum fraction x. Depending on the type of leptoquark a decay to a lepton l and a quark of generation j follows. Fig. 2.4 displays on the right-hand side the corresponding u-channel exchange of the (virtual) leptoquark between the electron and the antiquark of generation j after crossing. In case of of the outgoing lepton l being a muon or tau lepton, the leptoquark mediates LFV. If the outgoing lepton is an electron or electron-neutrino, the processes in Fig. 2.4 must be added to the matrix elements in NC/CC DIS processes as the initial and final states do not differ. This leads to constructive or destructive interference terms. As this analysis searches for LFV processes only, interferences with SM processes do not need to be taken into account. In the following, the outgoing lepton should be understood as a lepton of the second or third generation.

It is useful to define the Lorentz-invariant Mandelstam variables $\hat{s}$ and $\hat{u}$ for the hard subprocess in the s-channel and u-channel respectively:

$$\hat{s} = sx \tag{2.17a}$$

$$\hat{u} = Q^2 - s\ . \tag{2.17b}$$

Following [1] a double differential cross section for the s-channel tree level process can be deduced:

$$\frac{d^2\sigma_\mathrm{s}}{dxdy} = \underbrace{\frac{1}{32\pi\hat{s}}}_{\text{phase space}} \cdot \underbrace{\frac{\lambda_{eq_i}^2 \lambda_{lq_j}^2 \hat{s}^2}{(\hat{s}^2 - m_\mathrm{LQ}^2)^2 + m_\mathrm{LQ}^2 \Gamma_\mathrm{LQ}^2}}_{\text{Breit-Wigner LQ propagator}} \cdot \underbrace{q_i(x,\hat{s})}_{\text{parton density}} \times \begin{cases} \frac{1}{2} & \text{scalar} \\ 2(1-y)^2 & \text{vector} \end{cases}, \tag{2.18}$$

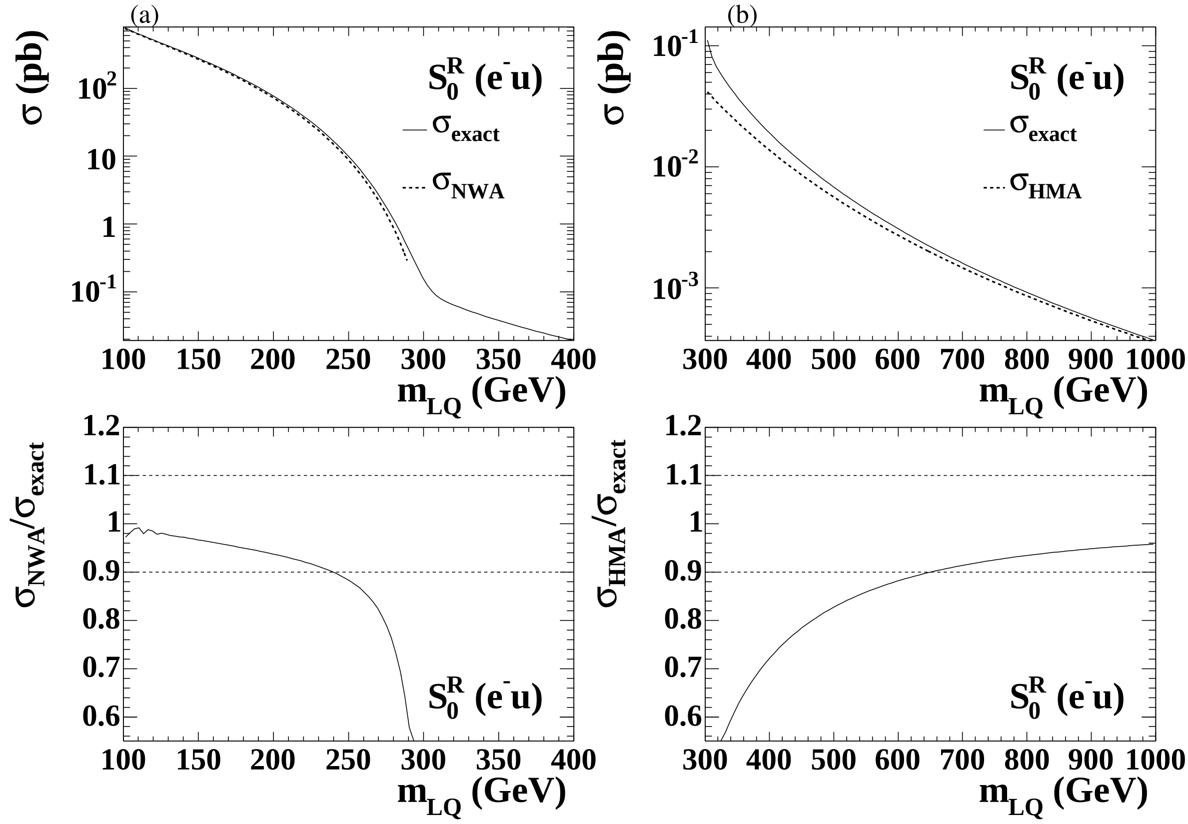

FIGURE 2.6: Total cross section of a scalar leptoquark as a function of the leptoquark mass. The exact cross section of a S_0^R with a coupling strength $\lambda = \lambda_{eq} = \lambda_{lq} = 0.3$ in comparison to the NWA (a) and in comparison to the HMA (b).

where the couplings λ_{eq_i} and λ_{lq_j} refer to the production and decay vertex respectively (see Fig. 2.4). The partial decay width Γ_{lq_j} for one possible final state is given by

$$\Gamma_{lq_j} = m_{\text{LQ}} \lambda_{lq_j}^2 \times \begin{cases} \frac{1}{16\pi} & \text{scalar} \\ \frac{1}{24\pi} & \text{vector} \end{cases} \tag{2.19}$$

with m_{LQ} being the leptoquark mass. The total width Γ_{LQ} is obtained by summing over all possible final states. In analogy to Eq. (2.18) the corresponding cross section for the u-channel exchange can be written down as:

$$\frac{d^2\sigma_{\text{u}}}{dxdy} = \frac{1}{32\pi\hat{s}} \cdot \frac{\lambda_{eq_i}^2 \lambda_{lq_j}^2 \hat{s}^2}{(\hat{u}^2 - m_{\text{LQ}}^2)^2} \cdot \bar{q}_j(x, -\hat{u}) \times \begin{cases} \frac{1}{2}(1-y)^2 & \text{scalar} \\ 2 & \text{vector} \end{cases} . \tag{2.20}$$

From the propagator term in Eq. (2.18) one can see that in case of a resonant leptoquark production a peak taking the form of a Breit-Wigner distribution in the x spectrum at a value

$x_0 = m_{\mathrm{LQ}}^2/s$ is expected (see Fig. 2.5a). In other words, the leptoquark mass can be reconstructed as a resonance with

$$m_{\mathrm{LQ}}^{\mathrm{rec}} = \sqrt{\hat{s}} = \sqrt{xs}\,. \tag{2.21}$$

In addition to the expected resonance in the mass spectrum, the existence of leptoquarks would lead to a characteristic y-spectrum. Scalar leptoquarks produced in the s-channel decay isotropically in their rest frame leading to a flat y-spectrum, whereas the decay of vector leptoquarks would be distributed according to $d\sigma/dy \propto (1-y)^2$. These specific angular distributions are markedly different from the y spectra in NC scattering, namely $d\sigma/dy \propto y^{-2}$ (see Eqs. (2.8a),(2.9),(2.12)).

Vice versa, in case of the u-channel leptoquark exchange the y-spectrum is flat for vector leptoquarks and behaves like $d\sigma/dy \propto (1-y)^2$ in case of scalar leptoquark exchange.

For couplings $\lambda \ll 1$ or low masses m_{LQ} the decay width is very small, such that the variation of the parton density $q_i(x,\hat{s})$ in the x range of size $\Gamma_{\mathrm{LQ}}/m_{\mathrm{LQ}}$ is negligible. As the u-channel contribution scales with λ^4, a total integrated cross section in the narrow width approximation (NWA) is often used:

$$\sigma_{\mathrm{NWA}} = \frac{\pi}{4s}\lambda_{eq_i}^2 \cdot \mathrm{BR} \cdot q_i(x_0 = \frac{m_{\mathrm{LQ}}^2}{s}, m_{\mathrm{LQ}}^2) \times \begin{cases} 1 & \text{scalar} \\ 2 & \text{vector} \end{cases}. \tag{2.22}$$

However, when approaching the kinematic limit where the values of the parton densities are very small, the coupling strengths which can be probed with the actual integrated luminosities are too high for the NWA to be valid (see Fig. 2.6a). The convolution of the steeply falling $q_i(x,\hat{s})$ with the Breit-Wigner distribution of finite width leads to a strong distortion of the leptoquark mass peak, and the mass spectrum shows very large tails towards low mass values (see Fig. 2.5a). As a result, the NWA underestimates the cross section significantly in the s-channel production for leptoquark masses $m_{\mathrm{LQ}} \approx \sqrt{s}$.

In the high-mass limit, i.e. $m_{\mathrm{LQ}} \gg \sqrt{s}$, both u-channel and s-channel diagrams contribute similarly to the cross section. In fact, the propagator term contracts in the high-mass limit to a four-fermion interaction. So, in the high mass approximation (HMA) the integration of Eqs. (2.18),(2.20) yields:

$$\sigma_{\mathrm{HMA}} = \frac{s}{32\pi}\left(\frac{\lambda_{eq_i}\lambda_{lq_j}}{m_{\mathrm{LQ}}^2}\right)^2 \left(\int xq_i(x,\hat{s})f(y)dxdy + \int xq_i(x,-\hat{u})g(y)dxdy\right), \tag{2.23}$$

with

$$f(y) = \overbrace{\begin{cases} \frac{1}{2} & \text{scalar} \\ 2(1-y)^2 & \text{vector} \end{cases}}^{s\text{-channel}} \qquad g(y) = \overbrace{\begin{cases} \frac{1}{2}(1-y)^2 & \text{scalar} \\ 2 & \text{vector} \end{cases}}^{u\text{-channel}}. \tag{2.24}$$

At HERA, the HMA suffers from the fact that it is accurate to better than 10% only for leptoquark masses above 600 GeV (see Fig. 2.6b). In contrast to the resonant production, both

e^+p scattering and e^-p scattering contribute considerably to the virtual effects from high-mass $F=0$ leptoquarks as well as from high-mass $F=2$ leptoquarks (see Fig. 2.5b).

Fig. 2.5 also gives an estimate on the expected rate of the LFV leptoquark events. With a coupling $\lambda=\lambda_{eq}=\lambda_{lq}=0.3$ the resonant production cross section for $275\,\mathrm{GeV}$ leptoquarks is $\mathcal{O}(10\,\mathrm{pb})$. Therefore, a clear signal of a few hundred events can be expected in a data set with a luminosity of $\sim 50\,\mathrm{pb}^{-1}$ for both e^+p scattering and e^-p scattering.

Squarks in R-parity violating Supersymmetry

The concept of Supersymmetry (SUSY) is one of the most appealing extensions of the SM and it predicts particles which can be identified with leptoquarks mediating LFV. SUSY is embedded in most of the serious GUTs solving the hierarchy problem in a very elegant way. Embedded electroweak symmetry breaking and the prediction of SM parameters from electroweak precision measurements are encouraging features of this theory. For a detailed description see [30].

SUSY assigns to each SM fermion a bosonic supersymmetric partner. The symmetry is broken such that the masses of the SUSY particles are out of the current experimental reach. The lightest supersymmetric particle (LSP) serves as a candidate for the dark matter in the universe. A new quantum number R-parity (R_p) is introduced with

$$R_p = (-1)^{3B+L+2S}\,, \tag{2.25}$$

where B is the baryon number, L is the lepton number and S is the spin of a particle. SM particles have $R_p = +1$ whereas SUSY partners have $R_p = -1$. In different SUSY scenarios R_p can be conserved or the R_p conservation can be violated. R_p conservation implies pair production of SUSY particles only, followed by a decay chain ending with the LSP. More interesting for ep scattering are R_p-violating SUSY scenarios as single SUSY particle production is possible. The LSP decays to SM particles which are visible in a detector as multi-lepton and/or multi-jet signatures.

In particular, the resonant production of so-called squarks in ep collisions is allowed by the presence of R_p-violating terms $\lambda' LQ\bar{D}$ in the superpotential

$$W = \frac{1}{2}\lambda_{ijk}L_iL_j\bar{E}_k + \lambda'_{ijk}L_iQ_j\bar{D}_k + \frac{1}{2}\lambda''_{ijk}\bar{U}_i\bar{D}_j\bar{D}_k, \tag{2.26}$$

with the superfields L (lefthanded lepton-like), E (righthanded lepton-like), Q (lefthanded quark-like) and U, D (righthanded up- and down-quark-like). The expansion of the $\lambda' LQ\bar{D}$ term to

$$\begin{aligned}\mathcal{L}_{LQ\bar{D}} = \lambda'_{ijk}\Big[& -\tilde{e}^i_L u^j_L \bar{d}^k_R - e^i_L \tilde{u}^j_L \bar{d}^k_R - \left(\bar{e}^i_L\right)^c u^j_L \tilde{d}^{k*}_R \\ & + \tilde{\nu}^i_L d^j_L \bar{d}^k_R + \nu^i_L \tilde{d}^j_L \bar{d}^k_R + \left(\bar{\nu}^i_L\right)^c d^j_L \tilde{d}^{k*}_R \Big] + c.c.\end{aligned} \tag{2.27}$$

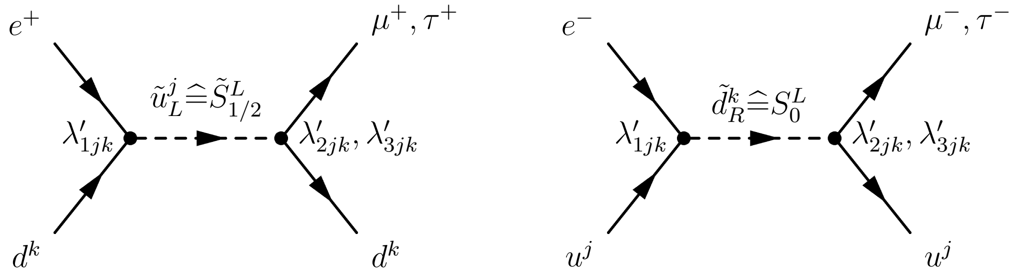

FIGURE 2.7: Feynman diagrams of resonant R_p-violating squark production in ep collisions. Left: Fusion of a positron and a down-type quark into an up-type squark ($\tilde{u}_L$,$\tilde{c}_L$,$\tilde{t}_L$) with R_p-violating coupling $\lambda'_{1jk} \neq 0$. Right: Fusion of an electron and an up-type quark into a down-type squark ($\tilde{d}_R$,$\tilde{s}_R$,$\tilde{b}_R$). With $\lambda'_{2jk} \neq 0$ or $\lambda'_{3jk} \neq 0$ a decay to a muon or tau lepton respectively mediates LFV. The squarks can be interpreted as leptoquarks of type $\tilde{S}^L_{1/2}$ and S^L_0 respectively.

reveals LFV processes as depicted in Fig. 2.7. If there are for example couplings $\lambda'_{1jk} \neq 0$ and $\lambda'_{2jk} \neq 0$, then the fusion of a positron and a down-type quark into an up-type squark ($\tilde{u}_L$,$\tilde{c}_L$,$\tilde{t}_L$) with a subsequent decay to a muon and a down-type quark will be possible in e^+p collisions. The up-type squark can be interpreted as a leptoquark of type $\tilde{S}^L_{1/2}$ mediating LFV. The corresponding dominant process in e^-p scattering is shown on the right-hand side of Fig. 2.7. Therefore, search results for S^L_0 leptoquarks apply for down-type squarks in such R_p-violating SUSY scenarios.

2.4.1 Search for LFV at dedicated low-energy experiments

As lepton flavour is believed to be violated in most of the SM extensions, there is a large variety of experiments where searches for LFV are performed. Not only at high-energy colliders such as LEP, TEVATRON, SLAC or HERA, but in particular at dedicated low-energy experiments the high sensitivity to individual LFV processes is used to find deviations from the SM. Details of those experiments can be found in the following references [31, 32, 33, 2, 34, 35].

As at the time of writing there is no direct evidence for LFV other than neutrino mixing only limits on LFV transitions exist. These 90% CL limits mostly refer to branching ratios of rare and exotic decays like $\mathrm{BR}(\mu^+ \to e^+\gamma) < 1.2 \times 10^{-11}$ [31] from the MEGA collaboration. The most stringent limits on the LFV processes $\tau^- \to e^-\gamma$ and $\tau^- \to \mu^-\gamma$ come from the BABAR collaboration with $\mathrm{BR}(\tau^- \to e^-\gamma) < 1.1 \times 10^{-7}$ [32] and $\mathrm{BR}(\tau^- \to \mu^-\gamma) < 6.8 \times 10^{-8}$ [33]. Limits on searches for rare kaon decays inducing lepton flavour violation are given in Tab. 2.3 [2].

The existence of heavy leptoquarks can induce LFV processes like these and, on the contrary, stringent limits on LFV decay processes can be interpreted as limits on leptoquarks mediating LFV. In the most general renormalisable description effective flavour changing interactions are generated by scalar and vector leptoquarks in analogy to a four-fermion interaction

decay mode	90% CL upper limit on BR	experiment	year
$K^+ \to \pi^+ e^- \mu^+$	1.2×10^{-11}	BNL-865	2003
$K^+ \to \pi^+ e^+ \mu^-$	5.2×10^{-10}	BNL-865	2001
$K_L \to \mu e$	4.7×12^{-11}	BNL-871	1998
$K_L \to \pi^0 \mu e$	3.4×10^{-10}	KTeV (prelim.)	2003

TABLE 2.3: Actual limits on rare kaon decays inducing lepton flavour violation [2].

of the form [34, 35]

$$\text{scalar:} \quad \frac{\lambda_{l_n q_i} \lambda_{l_m q_j}}{m_{\rm LQ}^2} \left(\bar{q}_i P^q q_j\right) \left(\bar{l}_n P^l l_m\right) \tag{2.28a}$$

$$\text{vector:} \quad \frac{\lambda_{l_n q_i} \lambda_{l_m q_j}}{m_{\rm LQ}^2} \left(\bar{q}_i \gamma_\mu P^q q_j\right) \left(\bar{l}_n \gamma_\mu P^l l_m\right) \tag{2.28b}$$

where P^q and P^l are chiral projectors of the quarks and leptons respectively which can be left ($P^L = (1 - \gamma_5)/2)$) or right ($P^R = (1 + \gamma_5)/2)$). Comparison with Eq. (2.23) shows that the cross section dependence on the factor $(\lambda_{l_n q_i} \lambda_{l_m q_j})/m_{\rm LQ}^2$ can be used to set comparable limits on high-mass leptoquarks coupling to first generation quarks and inducing LFV. For example, in [35] the limit

$$\frac{\lambda_{eq_1} \lambda_{\tau q_1}}{m_{\rm LQ}^2} < 2\sqrt{2} G_F \cdot \cos\theta_W \sqrt{\frac{\mathrm{BR}(\tau^- \to \pi^0 l^-)}{\mathrm{BR}(\tau^- \to \pi^- \nu)}} \tag{2.29}$$

is deduced from searches for highly suppressed tau lepton decays. With this the results from direct searches at high-energy colliders expecting virtual effects from high-mass leptoquarks with a cross section of Eq. (2.23) can be compared to limits from low-energy experiments[11].

---

[11] With regard to high-mass leptoquarks with $m_{\rm LQ} \gg \sqrt{s}$ collider machines may as well be denoted as low energy experiments.

Chapter 3

Experiment

This chapter describes the H1 experiment at the electron-proton storage ring HERA[1] as part of the research centre DESY[2] in Hamburg, Germany. The description given here focuses on the components of the H1 detector that are most relevant for this analysis. More details can be found in [36, 37].

3.1 The electron-proton collider HERA

In 1992, HERA started operation as the only electron-proton collider in the world. It represents the latest generation of high energy particle colliders at the DESY laboratory in Hamburg, Germany. An electron synchrotron called DESY started taking data in 1964 and was eponymous for the research site. In the early seventies, the e^+e^--collider DORIS[3] was built and first evidence for excited states of charmonium was found [38]. The next generation of colliders followed in the seventies with PETRA[4] This electron-positron collider of $2.7\,\mathrm{km}$ circumference was the largest at that time and lead in 1979 to the famous discovery of gluons in three jet events [39]. On the way to higher energies, PETRA became a pre-accelerator for HERA which, with a length of $6.3\,\mathrm{km}$, is currently the largest collider ever built at DESY.

HERA accelerates pulses or "bunches" of electrons to an energy of $27.6\,\mathrm{GeV}$ and protons to an energy of $920\,\mathrm{GeV}$ ($820\,\mathrm{GeV}$ before 1998) in two separate storage rings. At two interaction regions (north and south) the bunches are steered into collision at a rate of $10.4\,\mathrm{MHz}$. Around these interaction points the two experiments H1 in the north and ZEUS in the south are constructed to study ep collisions. Furthermore, the two fixed target experiments HERMES in the east and HERA-B in the west make use of the HERA beams. Fig. 3.1 shows the storage ring with the four experiments and an enlarged view of the pre-accelerators.

---

[1] **H**adron-**E**lektron-**R**ing-**A**nlage

[2] **D**eutsches **E**lektronen **Sy**nchrotron

[3] **Do**ppel-**Ri**ng-**S**peicher

[4] **P**ositron-**E**lektron-**T**andem-**R**ing-**A**nlage

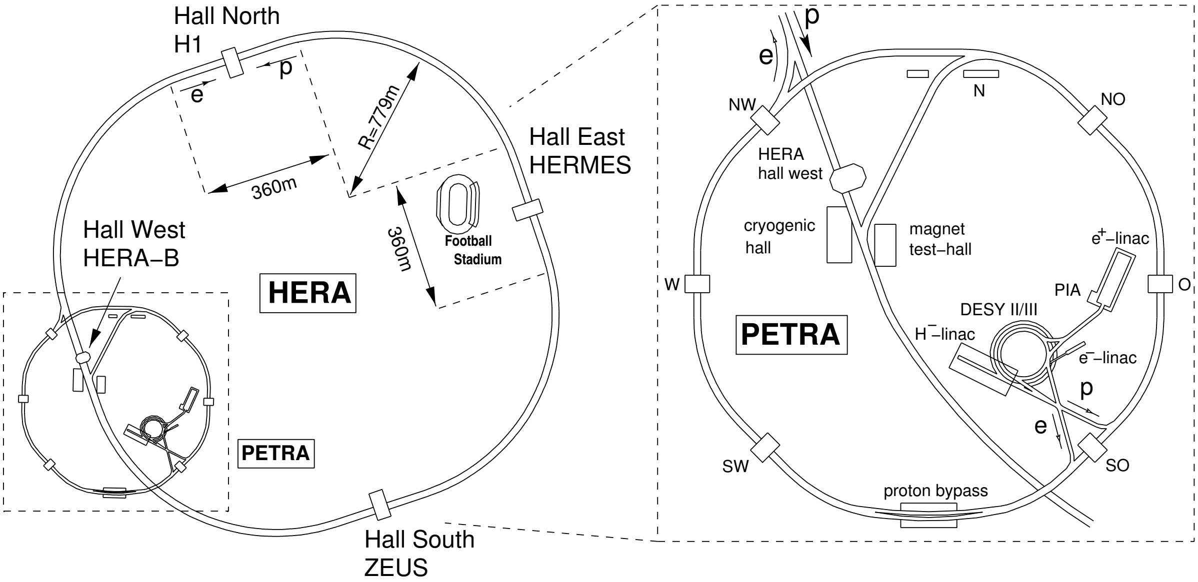

FIGURE 3.1: Schematic top view of the HERA collider. On the right hand side, the pre-accelerator system is depicted enlarged.

3.2 The H1 detector

As one of the two collider experiments at HERA, the multi-purpose detector H1 at the northern beam intersection was designed to measure the direction, energy and charge of particles resulting from ep collisions at its central interaction point. As the detector has been upgraded several times during its lifetime it should be noted that the description given here refers to the period 1998 to 2000 when the data that is analysed in this thesis was taken. The angular acceptance reaches almost hermetic coverage of 4π in solid angle, where mainly the feed through of the beam pipe results in an inevitable acceptance loss.

In Fig. 3.2 the H1 detector is illustrated with its main detector components. Arrows indicate the electrons coming from the left and the protons entering from the right. The right-handed H1 Cartesian coordinate system is defined such that the x-direction points to the centre of the HERA ring, y is the vertically upward direction and z is the direction of the proton beam (forward). The polar angle θ measures up to $180°$ from the positive z direction (forward) and the azimuthal angle ϕ starts from the positive x-axis and is positive for positive values of y. Due to the fact that the centre of mass system in ep collisions is boosted along the proton momentum direction, the detector arrangement is asymmetric with the forward part being more heavily instrumented and further segmented. In the following, the detector components relevant for this analysis are briefly discussed.

The description starts from the innermost point of the detector, the interaction vertex, outwards to the central and forward tracking system. The tracking systems consist of drift cham-

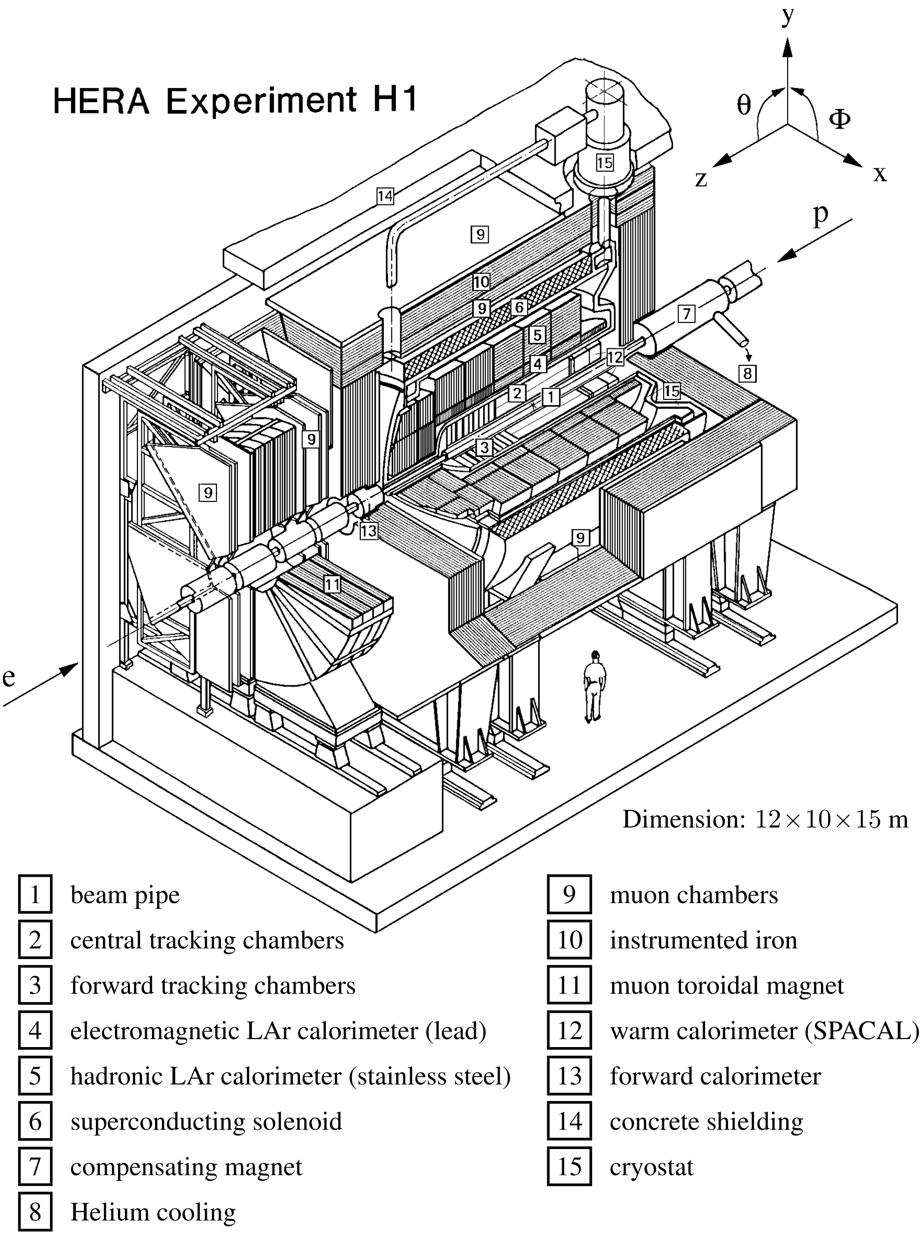

1	beam pipe	9	muon chambers
2	central tracking chambers	10	instrumented iron
3	forward tracking chambers	11	muon toroidal magnet
4	electromagnetic LAr calorimeter (lead)	12	warm calorimeter (SPACAL)
5	hadronic LAr calorimeter (stainless steel)	13	forward calorimeter
6	superconducting solenoid	14	concrete shielding
7	compensating magnet	15	cryostat
8	Helium cooling		

FIGURE 3.2: A 3d view of the the H1 detector with the main detector components.

bers and proportional chambers to measure trajectories and momenta of charged particles.

Further outwards, the LAr calorimeter inside a cryostat encloses the tracking chambers. Consisting of an inner electromagnetic part and an outer hadronic part, the energy and position of neutral or charged particles are determined.

A cylindrical superconducting solenoid surrounds the LAr calorimeter to generate a strong magnetic field of $1.12\,\mathrm{T}$ parallel to the beam axis. This leads to a curvature of trajectories in the tracking system produced by charged particles. Transverse momenta and sign of charge can be determined by this.

The iron return yoke of the magnet is instrumented with streamer tubes to measure hadronic energy leaking through the LAr calorimeter and to identify muon tracks. Further layers of the central muon chambers are positioned around the yoke to give a precise muon track measurement and additional drift chambers positioned at either side of the toroidal magnet detect muons in the forward direction.

3.2.1 Tracking

In the H1 experiment, tracking is performed with drift chambers, multi wire proportional chambers and silicon trackers. Using a combination of all components, track triggering, transverse momentum determination and charged particle identification can be performed in an angular range $5° < \theta < 178°$ with full azimuthal acceptance. Reflecting the asymmetry in ep-collisions, the tracking system is divided into a central and a forward part. Fig. 3.3 gives a schematic view of the rz-plane through all components of the H1 tracking system.

Central Tracking Detectors (CTD)

The angular range $20° < \theta < 178°$ is covered by the central tracking detectors (CTD). All central trackers are cylindrically aligned around the beam pipe.

- The Central Silicon Tracker (CST) is the nearest detector to the interaction point. Two layers of silicon strip detectors with an inner radius of $r_i = 5.75\,\mathrm{cm}$, an outer radius of $r_o = 9.75\,\mathrm{cm}$ and an active length of $35.78\,\mathrm{cm}$ measure hits of track trajectories with very high precision. The accuracy of $\sigma_{r\phi} = 12\,\mu\mathrm{m}$ and $\sigma_z = 22\,\mu\mathrm{m}$ allows for determination of secondary vertices resulting from the decay of long-lived particles with decay lengths of a few hundred micrometers.

- The central inner/outer multi wire proportional chambers (MWPC) CIP/COP detect charge particles with a fine timing resolution of $21\,\mathrm{ns}$. This is mainly used for triggering ep collisions with tracks coming from the nominal interaction vertex.

- The principle part of the tracking are the two concentric drift chambers CJC1 and CJC2. The CJC1 (CJC2) has a length of $2.2\,\mathrm{m}$, an inner radius $r_i = 20.3\,\mathrm{cm}$ ($r_i = 53.0\,\mathrm{cm}$) and outer radius $r_o = 45.1\,\mathrm{cm}$ ($r_o = 84.4\,\mathrm{cm}$). Wires are spanned parallel to the beam axis to

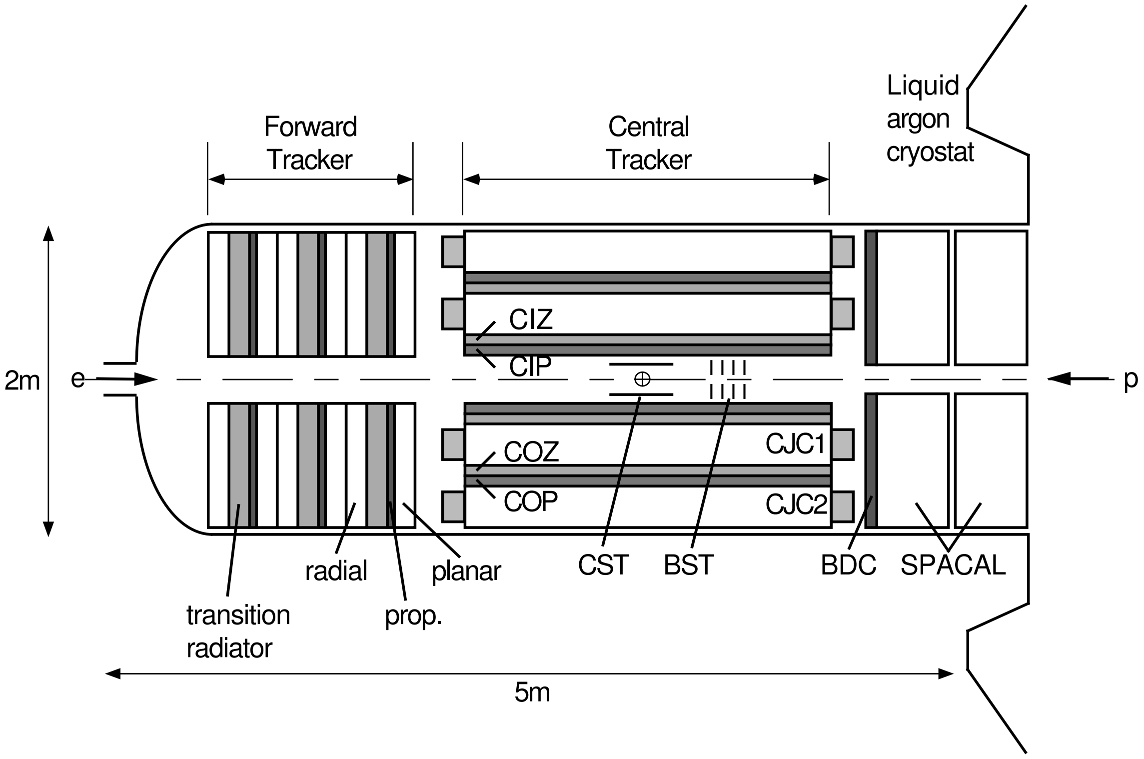

FIGURE 3.3: Schematic view of the rz-plane through the H1 tracking system.

allow a spatial resolution of $140\,\mu\mathrm{m}$ in the $r\phi$-plane. By charge division a z-resolution of $2.2\,\mathrm{cm}$ is achieved. The chambers are divided into 30 (60) drift cells that are inclined by about 30° with respect to the radial direction. This inclination leads to hits in different cells even from stiff tracks and improves the track reconstruction by linking of track segments. From the track curvature measured by all layers of the CJC the combined transverse momentum is determined with an uncertainty of $\sigma(p_T)/p_T = 0.01 \times p_T(\mathrm{GeV})$.

- The z-resolution by charge division in the CJC is significantly enhanced by the central inner/outer z-chambers CIZ/COZ. These thin drift chambers directly adjacent to the inside and outside of the CJC1 have circular strung sense wires with a drift field orthogonal to that of the CJC. This allows for a measurement of the z-position with an accuracy of typically $300\,\mu\mathrm{m}$.

Forward Tracking Detectors (FTD)

The forward tracking system is a set of drift chambers designed to detect tracks in the range $5^\circ < \theta < 25^\circ$. As can be seen on the left of Fig. 3.3, there are three identical *supermodules*, each consisting of three planar drift chambers, a MWPC, a transition radiator and a radial drift chamber. The planar chambers, having good resolution in $r\phi$, are located closest to the CJC in order to facilitate track linking. The MWPC system used for fast triggering is completed by the three MWPC of the forward tracker (FWPC). The transition radiator produces photons which are then in turn detected with an accurate $r\phi$-measurement in the radial drift chamber behind. The supermodules are slightly rotated against each other to improve the reconstruction of forward tracks.

3.2.2 Calorimetry

A variety of particles such as electrons, muons, neutral particles and particles in jets can be identified by measuring the energy deposition in calorimeters. The calorimeter system of the H1 experiment comprises four distinct components. With an asymmetric polar coverage of $4° < \theta < 154°$ and full azimuthal acceptance the Liquid Argon Calorimeter (LAr) is the largest calorimeter at H1. In the forward region close to the beam pipe a small calorimeter called PLUG extends the polar acceptance to angles below $4°$. The backward region is covered by the spaghetti calorimeter (SPACAL). Energy leaking through the LAr is detected by the tail catcher that is part of the instrumented iron which encloses the LAr.

Liquid Argon Calorimeter (LAr)

Covering large parts of the solid angle around the interaction point of ep collisions at H1, the LAr calorimeter is of prime importance for the calorimetry of the experiment. In terms of laboratory pseudorapidity[5] the LAr covers a range of $-1.47 < \eta < 3.35$. It is situated inside the magnetic coil to minimise the passive material before electron recognition and hadronic energy measurement.

Fig. 3.4 depicts the LAr calorimeter with its segmentation inside its cryostat shell. The longitudinal section shows a division in eight *wheels*, i.e. listed by position from the backward BBE, CB1, CB2, CB3, FB1, FB2, OF and IF. With the exception of the BBE, each wheel has an inner electromagnetic section with a fine granularity specialised for detecting electrons and photons. The larger hadronic parts are located further outside with coarse granularity. The transverse cut in Fig. 3.5 shows that each wheel is subdivided into octants where the hadronic sections have faces inclined to each other with respect to the radial direction.

The LAr is a sampling calorimeter where instrumented absorber plates are placed parallel to each other in a liquid Argon bath. The liquid Argon acts as the active material between the high voltage and readout modules on the absorber plates. The absorbers in the electromagnetic section are $2.4\,\mathrm{mm}$ thick lead layers with active gaps of $2.35\,\mathrm{mm}$. The layers add up to 20-30 radiation lengths depending on the impact angle. In contrast to the electromagnetic part, the larger hadronic LAr uses stainless steel as absorbing material. These steel plates are $19\,\mathrm{mm}$

---

[5] $\eta = -\ln(\tan\frac{\theta}{2})$

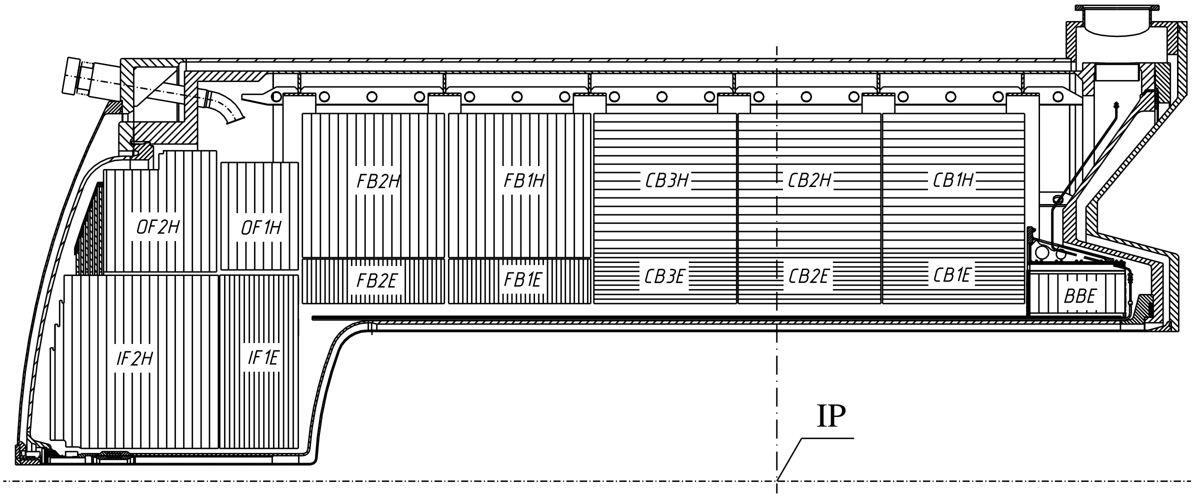

FIGURE 3.4: Longitudinal section of the LAr calorimeter showing the segmentation inside its cryostat shell.

thick with an active $2.4\,\mathrm{mm}$ layer of liquid Argon in between. Including the electromagnetic part, absorption of hadronic particles corresponding to 5-8 nuclear interaction lengths is achieved.

To obtain an impact angle of less than 45° with respect to the absorber plates, the central and backward wheels have orthogonal oriented plates with respect to the radial direction, whereas the layers of the forward wheels lie in the $r\phi$-plane. The rectangular shaped readout cells in the electromagnetic partition have a size of about $3\,\mathrm{cm}$ in the forward wheels and CB3 and about $6\,\mathrm{cm}$ in the more backward wheels. The granularity of the central (forward) hadronic calorimeter amounts to 3 (6) readout cells per layer.

With this granularity a precise spatial measurement of the energy deposition is obtained and electromagnetic showers are clearly seperated from hadronic ones. With test beam measurements [40, 41] an electromagnetic energy resolution of

$$\frac{\sigma_{\mathrm{el}}(E)}{E} = \frac{11\%}{\sqrt{E/\mathrm{GeV}}} \oplus 1\% \tag{3.1}$$

and a hadronic energy resolution of

$$\frac{\sigma_{\mathrm{had}}(E)}{E} = \frac{50\%}{\sqrt{E/\mathrm{GeV}}} \oplus 2\% \tag{3.2}$$

was achieved.

It should be noted that a noticeable fraction of hadronic decays lead to semi-stable final states including neutrons with energy depositions with a delay of up to 10 minutes, whereas electromagnetic interactions are not affected by this. In contrast to the uranium scintillator

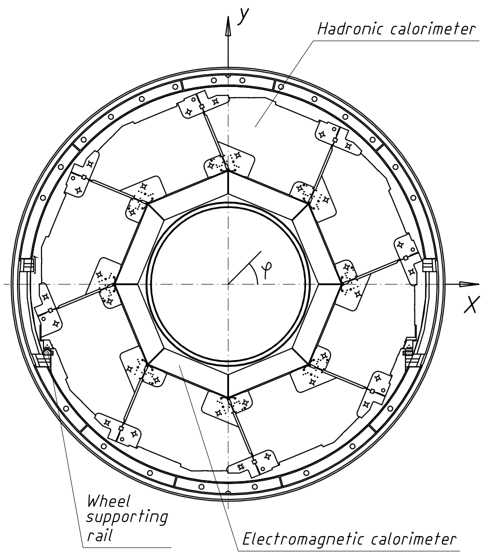

FIGURE 3.5: Transverse section of the LAr calorimeter showing the partitioning into octants.

calorimeter of the ZEUS experiment where neutron interactions with uranium compensate for this discrepancy between the hadronic and electronic energy determination, the H1 LAr calorimeter is *non-compensating*. Offline correction factors taken from a shower shape analysis must be applied here.

Spaghetti Calorimeter (SPACAL)

The backward region $\theta > 154^\circ$ is not covered by the LAr calorimeter to allow the insertion of the tracking system after maintenance or upgrades. Once the tracking system is installed, the scintillating fibre *spaghetti* calorimeter (SPACAL) is plugged into the uncovered backward region of the LAr to perform calorimetry in the range $153^\circ < \theta < 177.8^\circ$. The impression of an opened spaghetti pack when viewed from the interaction point backwards onto the cap of many cylindric submodules gave rise to the name of the calorimeter. Similar to the LAr the finer segmented electromagnetic section is located at the forward side looking towards the interaction point. The 1192 electromagnetic submodules with an active face of $40.5 \times 40.5\,\mathrm{mm}^2$ each consisting of lead absorbers, a fibre bundle and a photomultiplier readout allow an accurate position measurement with an excellent timing resolution. The fact that all photomultipliers are read out in about $1\mathrm{ns}$ permits the reading of time-of-flight information from energy deposits in the SPACAL. The electromagnetic energy is measured with an accuracy of $\sigma_{\mathrm{el}}(E)/E = 7\%/\sqrt{E/\mathrm{GeV}} \oplus 1\%$. The hadronic section behind has 136 channels where each module covers an area of $120 \times 120\,\mathrm{mm}^2$. A hadronic energy resolution of $\sigma_{\mathrm{had}}(E)/E = 13\%/\sqrt{E/\mathrm{GeV}}$ is achieved.

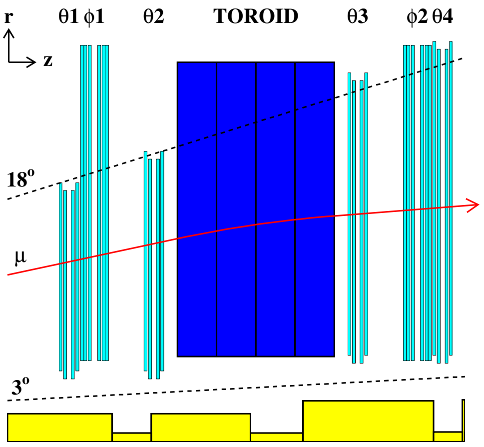

FIGURE 3.6: Schematic view of the Forward Muon Detector with the six drift chambers labelled according to their position measurement θ_0-θ_4 and ϕ_0-ϕ_1.

As the SPACAL mainly detects the scattered electron coming from ep collisions with a squared momentum transfer below $150\,\mathrm{GeV}^2$, it is of minor relevance for this analysis.

3.2.3 Muon system

The identification of muons with an energy and momentum determination is mainly performed in the muon system of the H1 detector. Analogous to the tracking system it is divided into a forward and a central part.

Forward Muon Detector (FMD)

Muons with a polar angle of $3^\circ < \theta < 17^\circ$ and an energy larger than $5\,\mathrm{GeV}$ are detected in the Forward Muon Detector (FMD) of the H1 experiment. The three layers attached to either side of the toroidal magnet are situated outside the main detector region at a z-position of $6.4\,\mathrm{m}$ and $9.4\,\mathrm{m}$ respectively. In order to perform a position determination in ϕ two layers have radially strung wires whereas the wires in four layers are circularly spanned to measure θ (see Fig. 3.6).

Central Muon Detector (CMD)

The Central Muon Detector (CMD) is the outermost hermetic detector at H1 enclosing the inner detectors in form of an octagonal barrel. It has a polar angle coverage of $5^\circ < \theta < 175^\circ$. A part of the system takes the form of streamer tubes inside the iron return yoke for the solenoid. To either side of the iron there are three additional active layers called inner and outer muon boxes to improve the muon tracking and to cover the edges of the detector. In the z-direction,

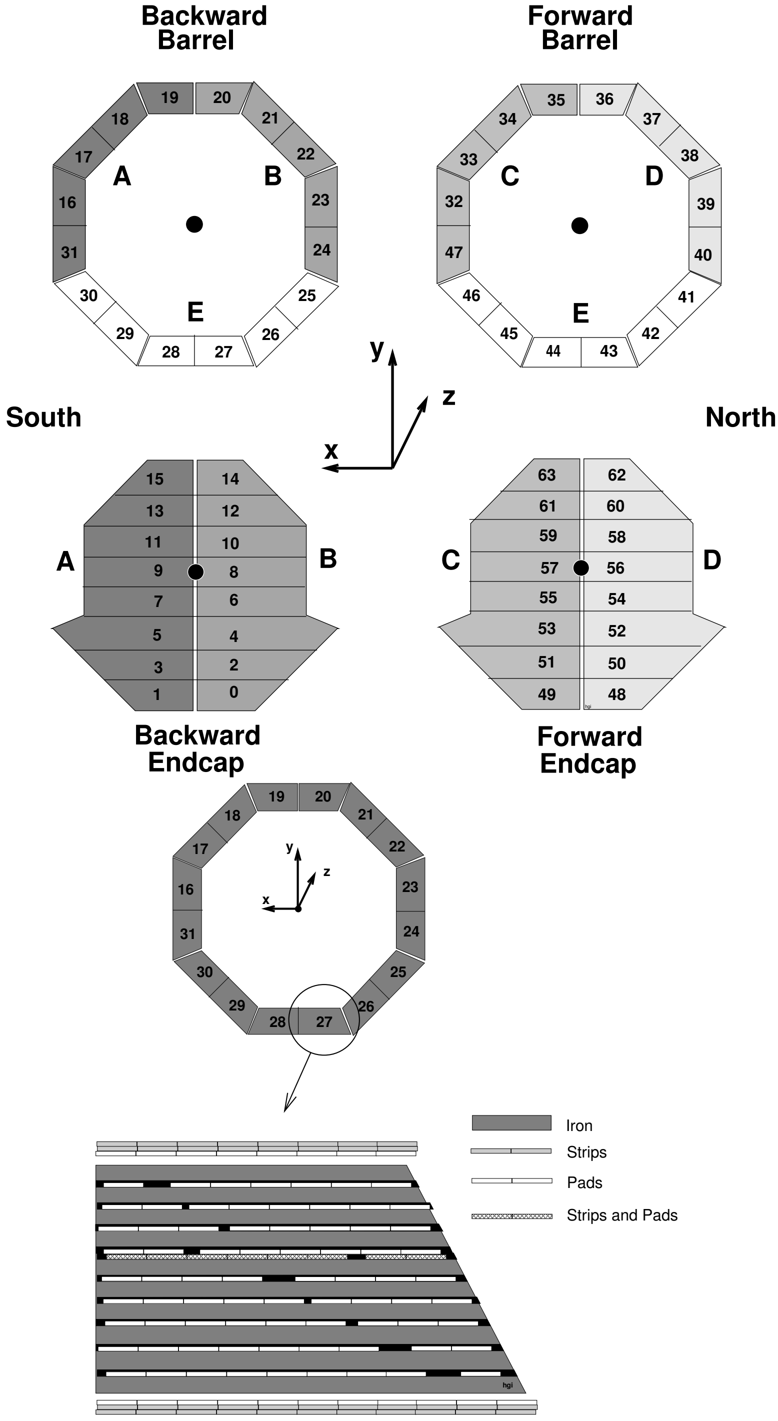

FIGURE 3.7: Layout of the Central Muon Detector with its 64 modules. One exemplary module is illustrated in detail.

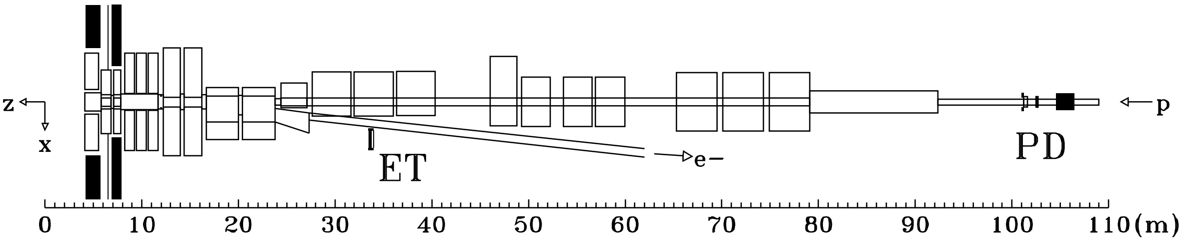

FIGURE 3.8: The H1 luminosity system. Photons and electrons are detected at very small scattering angles with the electron tagger (ET) at $z = -33.9\,\mathrm{m}$ and the photon tagger (PT) at at $z = -102.9\,\mathrm{m}$.

the system is divided into two endcaps, a forward and a central barrel. Each of these partitions itself contains 16 modules with varying shape and orientation as can be seen in Fig. 3.7.

The spatial resolution perpendicular to the streamer tubes is 3-4 mm. Strip electrodes attached to the wires allow a position determination along the direction of the wires with a precision of 10-15 mm. Known as the *tail catcher* some layers have additional pad electrodes to measure the energy that was not already deposited in the LAr. Single layers detect muons with an efficiency of up to 80%, limited by the detector geometry.

3.2.4 Luminosity system

An essential part of all analyses in high-energy physics is the accurate determination of the integrated luminosity corresponding to the amount of accumulated and analysed data.

At HERA, Bethe-Heitler processes, i.e. $ep \rightarrow ep\gamma$, are used as a reference process with a well known cross section calculated from QED. In most of these processes, the scattered electron as well as the radiated photon have extremely small scattering angles and escape the central H1 detector via the backward beam pipe feed through.

Hence, the two parts of the H1 luminosity system are situated far away from the rest of the experiment in the backward direction (see Fig. 3.8), i.e. the electron tagger (ET) at $z = -33.9\,\mathrm{m}$ and the photon tagger (PT) at $z = -102.9\,\mathrm{m}$. Both detectors are located very close to the beam pipe. Counting rates of simultaneous hits in the ET and the PT can be used to determine the luminosity online. As an alternative method, the photon rates above a certain energy threshold can be used for an offline luminosity measurement. To estimate the large background from bremsstrahlung after collisions between electrons and residual gas molecules, i.e. $eA \rightarrow eA\gamma$, the effect from non-colliding bunches (*pilot bunches*) can be studied. With these corrections a luminosity determination to a precision of 1.5% is achieved.

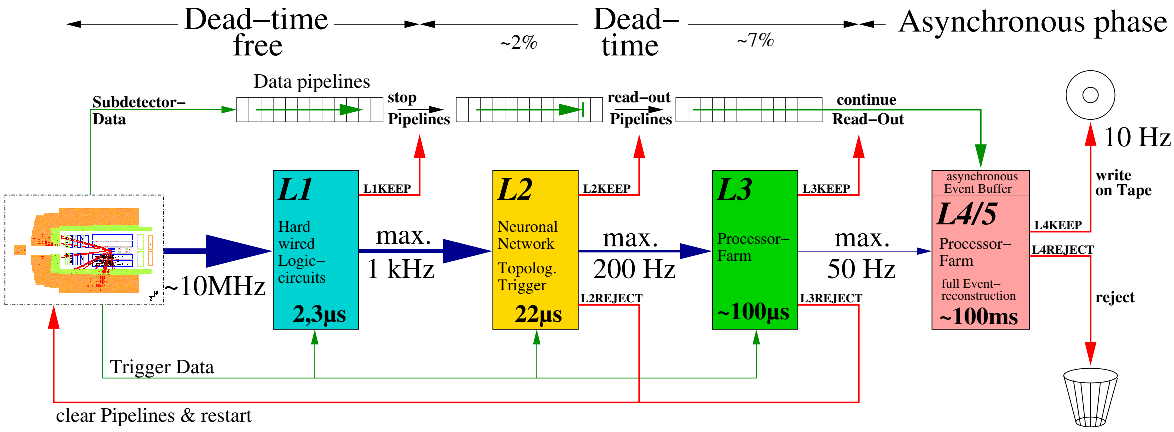

FIGURE 3.9: The data flow through the H1 trigger layout.

3.2.5 Time-of-Flight system (ToF)

The ep collisions at HERA have a strict timing with a period of $96\,\mathrm{ns}$. Other processes that are detected 'out-of-time' are very likely to be background events originating from beam interactions with residual gas or the beam pipe itself. This background can be reduced with the timing information delivered by the Time-of-Flight system (ToF). The ToF system consists of plastic scintillators at various places in the H1 experimental area. In particular the two scintillators of the *veto-wall* at $z = -8.1\,\mathrm{m}$ and $z = -6.5\,\mathrm{m}$ reject events with a timing outside a time window given by the HERA clock as background.

3.3 Trigger and Data Acquisition

One of the major challenges of the H1 experiment is the efficient recording of events of physical interest at the technically feasible rate of about $50\,\mathrm{Hz}$, where significant detector signals come in with typical rates of several $100\,\mathrm{kHz}$. This raw signal rate is clearly dominated by all kinds of background events and detector noise.

To reduce this background a sophisticated trigger system is needed to decide on different levels which events to record and which to reject. During the data taking period relevant for this analysis, there were three online trigger levels active. A schematic view of the H1 Trigger system is illustrated in Fig. 3.9.

On the first trigger level (L1) a fast decision from hardware components is made. During this decision time of $2.3\,\mu\mathrm{s}$ all event information is buffered in pipelines, such that the read-out of all incoming events is still guaranteed. Hence, L1 is a *dead-time free* trigger level. In the central trigger logic (CTL) the coincidence of signals from several detector subsystems are formed to L1 trigger decisions which are concentrated into 128 *subtriggers*. After a positive trigger decision in one of the subtriggers the pipelines are read out and a reduced event information is sent to the second trigger level (L2).

The second trigger level has more time for the event analysis. In a time window of about $22\,\mu\mathrm{s}$ a neural net algorithm (L2NN) and specialised event topologies (L2TT) are used to validate the L1 decision. The topological trigger L2TT handles local coincidences of detector signals and searches for particle patterns or expected topologies. L2NN performs complex cuts in the phase space spanned by the signals from several detector components. An L2 decision to keep the event stops the pipelines and triggers a full event readout. This causes an inevitable total dead time of about $1.5\,\mathrm{ms}$.

Although the trigger level L3 is part of the original H1 trigger design as shown in Fig. 3.9, it was not active at the time when the data analysed in this thesis were recorded.

On the fourth trigger level L4 the event is partially reconstructed and analysed in a parallel processor farm. Events are permanently written to tape if they pass the analysis cuts of the L4 algorithms.

The last selection (L5) is performed offline with full event reconstruction and classification.

The data acquisition is organised in H1 runs in which the readout status and the trigger strategy are stable.

3.4 Detector Response Simulation

In order to compare the recorded data with a theoretical prediction, a deep understanding of the detector response is indispensable. This is obtained by a very detailed simulation of the H1 detector in all aspects using the GEANT [42] simulation tool. This description includes all instrumentations as well as all passive material and delivers a full three-dimensional picture showing geometrical acceptances, intrinsic resolutions or any material affecting the detector response.

Events generated with a Monte Carlo generator incorporate in a first step the intrinsic physical event features such as particle tracks in the magnetic field, secondary particle generation, showering or fragmentations. This is then taken as an input to the simulation of the response of active detector components. Then, the response signals are fed through the same reconstruction process as the data events. These simulated events can be compared with the data to allow for offline detector controlling and data analysis.

Chapter 4

General data analysis

This chapter describes general analysis methods which are applied on the data. The e^-p data from 1998/1999 and the e^+p data from 1999/2000 are analysed separately. The analysis starts with data quality checks. Bad quality data taking runs are excluded from further analysis. Essential detector components must have been fully operational and the applied trigger strategy must have collected the required data efficiently. In order to understand the data by comparison with SM MC simulations, the MC data are adapted to the conditions of the analysed data set. It is also very important to reject background from non-ep collisions. The reconstruction of kinematic variables and the identification of particles and jets is explained in Sec. 4.3. Following the reconstruction, the calibration of the energy measurement for electromagnetic and hadronic energy deposits is checked. The MC simulation of SM background processes and of signal processes with leptoquarks mediating LFV in ep collisions are also described. The chapter closes with a presentation of a NC DIS control sample.

4.1 Data quality

A HERA fill runs for up to 12 hours. As described in Sec. 3.3 the H1 data taking is organised in H1 runs which last approximately 1-2 hours. Corrupted data, detector defects, run aborts or other malfunctions may lead to a run qualification as *poor*. These runs are excluded in this analysis.

The subdetectors of the H1 experiment that are relevant for this analysis must be fully operational during the analysed data taking period. This means that only events with nominal high-voltage (HV) status and correct readout information for CJC1, CJC2, CIP, COP, LAr, SPACAL, Luminosity and ToF system are considered. As described in Ch. 3, these individual components are essential for tracking, triggering, calorimetry, luminosity determination and background rejection.

To reduce background originating from non-ep collisions such as beam gas interactions or collisions with residual gas molecules, the reconstructed z-position of the vertex, z_{vtx}, is

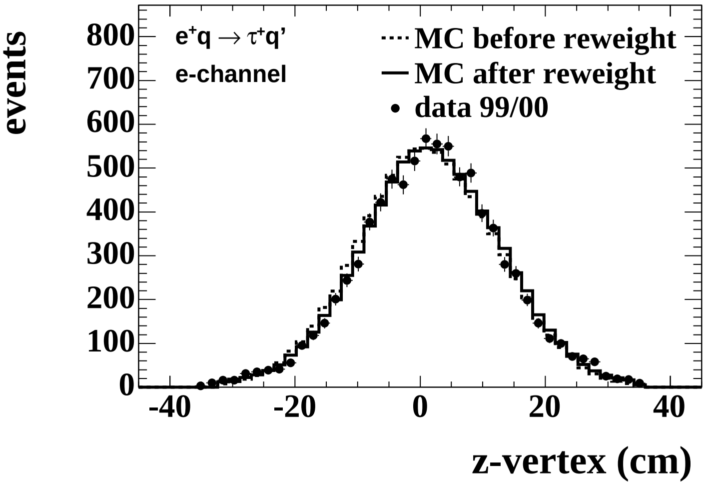

FIGURE 4.1: z_{vtx}-distribution before and after reweighting of the MC simulations to the beam conditions in the 99/00 e^+p data.

required to be in a range of $\pm 35\,\mathrm{cm}$ around the nominal run vertex. As the detector is designed to detect particles from ep-collisions in the centre of the detector, this cut on z_{vtx} enhances the data quality by selecting events in the detector acceptance only.

As the measurement of the polar angle and therefore transverse momenta of particles and jets depend on the reconstruction of the z-position of the vertex, an exact description of the z_{vtx}-distribution by MC simulations of SM background processes is needed. In MC simulations the z-position of the vertex is smeared with a Gaussian distribution. Whereas the mean z_{vtx} changes in the data with different beam conditions over the time of data taking yielding a non-Gaussian superposition for the whole data set. This effect must be corrected for by reweighting the MC simulations according to the beam conditions in the data. The effect of this reweighting for 99/00 e^+p data can be seen in Fig. 4.1. The selection criteria for these events are given in Sec. 4.4. One can see that the description of the z_{vtx} distribution by the MC simulations improves slightly with the reweighting.

The complete data set that is analysed in this analysis after the data quality criteria mentioned above is summarised in Tab. 4.1. The correct determination of the corresponding integrated luminosity depends on the HV and readout requirements as well as on the allowed z_{vtx} range.

In addition to the non-ep background events from collisions with residual gas molecules (*beam-gas*) and beam pipe material (*beam-wall*) near the detector, there is a sizeable amount of events from cosmic rays or beam-halo muons. Beam-halo muons result from decays of charged pions which are produced in beam-gas or beam-wall events at some larger distance to the detector. Although the ToF system (Sec. 3.2.5) efficiently rejects a large amount of these events by timing requirements at the trigger level, further timing cuts are applied to reduce the

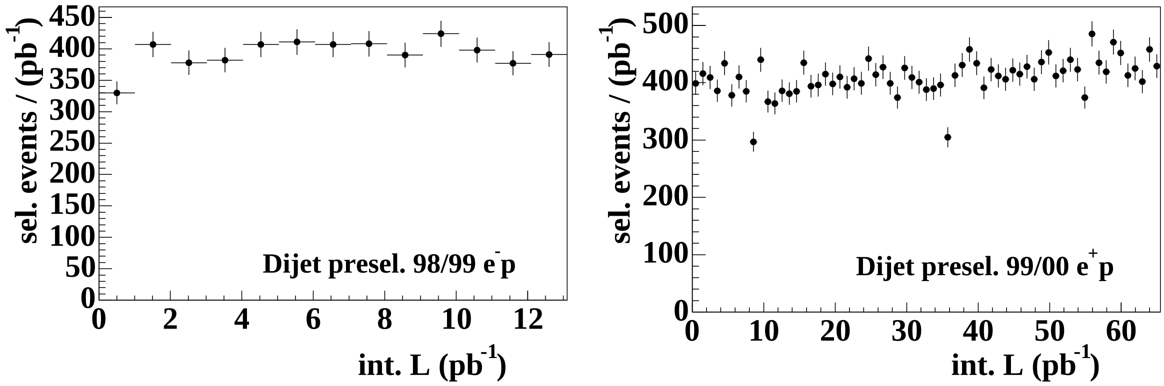

FIGURE 4.2: Event yield for the selection of a dijet sample with $p_{T,\mathrm{jet1}} > 20\,\mathrm{GeV}$ and $p_{T,\mathrm{jet1}} > 15\,\mathrm{GeV}$ (see Sec. 6.4.1).

data set	$\sqrt{s}$	collisions	H1 run range	$\int \mathcal{L}dt$
1998 – 1999	319 GeV	e^-p	218217 – 241649	$13.1\,\mathrm{pb}^{-1}$
1999 – 2000	319 GeV	e^+p	244968 – 279215	$65.5\,\mathrm{pb}^{-1}$

TABLE 4.1: Summary of analysed data sets.

remaining non-ep background. Only events in a time window of $\pm 4.8\,\mathrm{ns}$ around the nominal interaction time of three bunch crossings[1] are selected. The proper event time is reconstructed offline from the drift chamber data.

Background events fulfilling the timing criteria can be further rejected by their characteristic event topology. The H1 experiment provides a set of background finders for the recognition of cosmic events and beam-halo events. Characteristic isolated narrow and long signatures traversing the H1 detector through many subdetectors are searched for by these background finders. In this analysis the so-called *safe* set of background finders [43] are applied and parts of the background finder sets developed in [44, 45] are used. Background finders which classify more than 1% of the LFV signal MC simulation as background are not used.

As a last step of data quality requirements, the H1 event display can be used to visually scan selected events for suspicious characteristics. All selected data with moderate and low statistics after final selection steps are visually scanned.

Fig. 4.2 shows the event yield for the selection of a dijet sample with $p_{T,\mathrm{jet1}} > 20\,\mathrm{GeV}$ and $p_{T,\mathrm{jet1}} > 15\,\mathrm{GeV}$ which is performed to select tau-quark pairs from a leptoquark decay with a subsequent hadronic tau decay (see Sec. 6.4.1). Except for short periods of data taking in the years 99/00 when the detector performance was degraded, the event yield is constant resulting

---

[1] According to the HERA clock every $96\,\mathrm{ns}$ electron and proton bunches cross at the interaction point. The nominal bunch crossing plus the ones before and after are analysed.

in about 400 events per pb^{-1} of integrated luminosity.

4.2 Trigger

As mentioned in Sec. 3.3, the H1 trigger decision on level L1 is built up of 128 subtriggers. As the H1 experiment is a multi-purpose detector, only a distinct set of subtriggers is suitable for a dedicated analysis. This analysis searches for exotic events expected in the high-Q^2 domain. These events are mainly triggered by large energy deposits in the LAr calorimeter. Five subtriggers based on LAr energy deposits are therefore selected:

- *s66*: Large missing transverse energy with forward energy deposits.
- *s67*: Large electronic energy deposits.
- *s71*: Energy deposits in spatial combination with MWPC tracks.
- *s75*: Large localised (L2TT) electronic energy deposits in coincidence with a high-p_T track.
- *s77*: Missing transverse energy.

In addition to electrons and hadronic particles with large transverse momenta, high-p_T muons are expected to trigger events of a leptoquark with $m_{\mathrm{LQ}} = \mathcal{O}(100\,\mathrm{GeV})$ decaying to a muon-quark pair. Therefore, additional five subtriggers based on the muon system are used to select events including a muon in the final state. The selection of the muon subtriggers follows that employed in [46].

- s15: Central muons in the barrel or in the outer endcaps are combined with low track multiplicities.
- s19: Central muons in the barrel in combination with high track multiplicities.
- s22: Central muons in the outer endcaps in combination with high track multiplicities.
- s34: Central muons in the barrel in combination with low track multiplicities.
- s56: Any muon in combination with a SPACAL trigger optimised for electrons.

For further details of the selected subtriggers see [13, 47, 48].

On some of the subtriggers described above, prescale factors are temporarily applied to reduce the recorded data volume. This means, if a subtrigger rate exceeds a given value, only a fraction of triggered events in a given H1 run are recorded, according to the prescale factor. It is therefore necessary to verify that selected data events after final selection steps are not exclusively triggered by prescaled subtriggers.

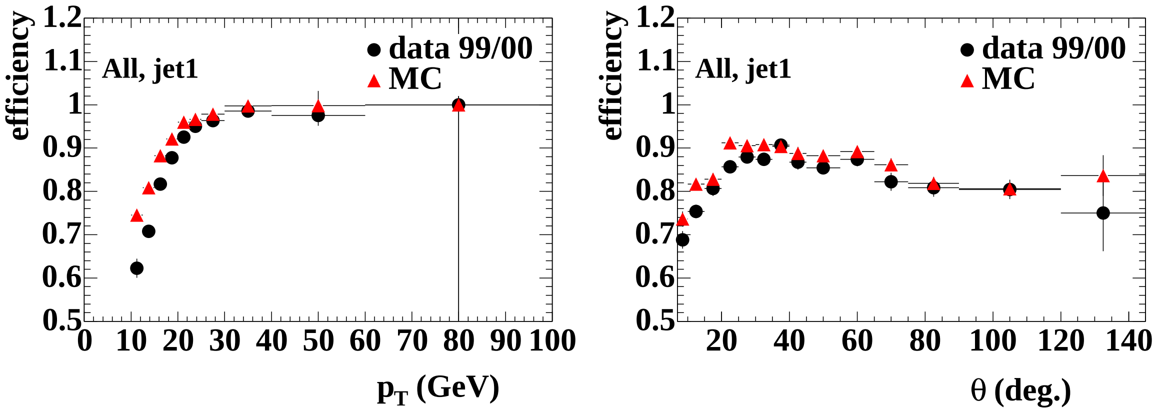

FIGURE 4.3: Efficiency of the combination of subtriggers s66, s67, s71, s75 and s77 in a dijet sample with $p_{T,\mathrm{jets}} > 10\,\mathrm{GeV}$ as a function of the p_T (left) and θ (right) of the highest-p_T jet (jet1).

4.2.1 Trigger efficiency

Events containing a high-p_T electron are mostly triggered by the non-prescaled subtrigger s67. The efficiency of the s67 for triggering events with an electronic energy deposit above $10\,\mathrm{GeV}$ is shown in [49] to be close to 100% . Such electronic energy deposits are expected from a decay of a heavy leptoquark to a tau-quark pair and a subsequent electronic tau decay or a hadronic tau decay with neutral hadrons. In the latter case large fractions of neutral mesons like π^0 deposit electromagnetic energy in form of photon pairs.

It is shown in [48] that high-p_T muons are triggered with an efficiency of more than 90% by the muon subtriggers in combination with the LAr-based subtriggers described above for events with a transverse momentum of the hadronic system $p_{T,\mathrm{HFS}} > 10\,\mathrm{GeV}$ (see Sec. 4.3.1). For large values of $p_{T,\mathrm{HFS}}$ the subtriggers s66 and s77 efficiently trigger the CC-like signature in the calorimeter. Events with medium $p_{T,\mathrm{HFS}}$ and $p_{T,\mu}$ are triggered efficiently by the muon triggers.

In case of a hadronically decaying tau in the event, a dijet signature is expected in the detector. The trigger efficiency of the LAr-based subtriggers for dijet events with $p_{T,\mathrm{jets}} > 10\,\mathrm{GeV}$ is displayed as a function of p_T and θ of the highest-p_T jet (jet1) in Fig. 4.3. For $p_{T,\mathrm{jet1}} > 20\,\mathrm{GeV}$ the trigger efficiency is near to 100% and well described by the MC simulation. For values below $20\,\mathrm{GeV}$, the trigger efficiency drops rapidly and the description by MC simulation is poor. Hence, the search for LFV events with a hadronically decaying tau requires $p_{T,\mathrm{jet1}} > 20\,\mathrm{GeV}$.

4.3 Reconstruction

In this section the reconstruction of particles and the kinematic variables is discussed. Depending on the event topology different methods for the measurement of the kinematic variables

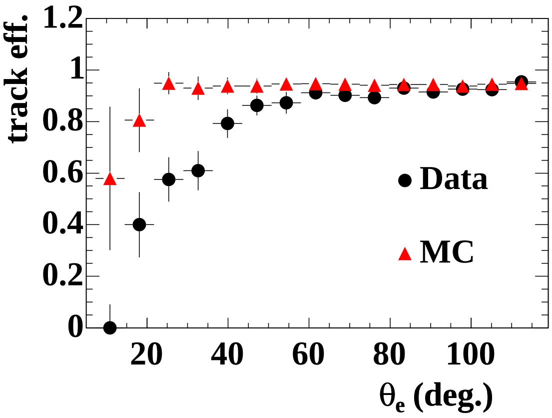

FIGURE 4.4: Efficiency of finding charged tracks with a maximal distance of closest approach (DCA) of $12\,\mathrm{cm}$ to an electron in a high-Q^2 NC DIS sample.

are employed. Eqs. 2.6 show that in NC DIS the determination of both electronic and hadronic energy as well as the electronic and hadronic scattering angles yield a redundancy in information for the reconstruction of the kinematics. Before the discussion of the reconstruction methods the relevant particle identification methods are explained.

4.3.1 Particle identification

Electrons

The H1 standard electron finder QESCAT [50] is used to find compact and isolated electromagnetic clusters. The characteristic shower shapes of electrons and photons are used to distinguish them from showers in the electromagnetic part of the LAr calorimeter induced by hadronic particles. As the decay products of leptoquarks are mainly emitted into the central and forward region, the SPACAL is not used for particle identification.

It should be noted that there is no track requirement for the electron as in most high-Q^2 NC DIS analyses. The reason for the weak tracking criteria can be seen in Fig. 4.4. The tracking efficiency in this data period falls off significantly in the forward detector region. The problems in the description of the FTD by the simulation are known to the H1 collaboration. Nevertheless, if vertex-fitted isolated tracks which can be identified with the electron are found, i.e. with a maximal distance of closest approach (DCA) of $12\,\mathrm{cm}$, they are combined with the electron calorimetry.

The electron polar angle θ_e is reconstructed from the primary vertex and the centre of gravity of the electromagnetic cluster. For low energy clusters the more precise tracking information, if available, is used. It was shown in [51] that the spatial alignment of tracking detectors relative to the LAr is within $1\,\mathrm{mm}$ in all directions.

The geometrical setup of the LAr modules (see Fig. 3.5) results in inactive detector regions between the individual octants and wheels. These detector regions must be excluded for the measurement of electromagnetic energy. A minimal distance of $2°$ in ϕ to a so-called ϕ-crack between the LAr octants is required. From Fig. 3.4 one can see that the z-cracks between wheels CB1/CB2 and CB2/CB3 also point near the interaction vertex. Therefore, the z-component of the electron impact at the calorimeter surface z_{imp} is required to be neither in the region $15\,\mathrm{cm} < z_{\mathrm{imp}} < 25\,\mathrm{cm}$ nor in the region $-65\,\mathrm{cm} < z_{\mathrm{imp}} < -55\,\mathrm{cm}$.

Muons

A muon candidate is identified by a track measured in the inner tracking system geometrically matching with signals in the muon system or a minimal ionising particle pattern in the LAr calorimeter.

Due to their mean bremsstrahlung radiation and low energy loss in nuclear interactions, reconstructed muons with a transverse momentum above $1\ \mathrm{GeV}$ penetrate the central detector components with a maximal energy loss of $5\,\mathrm{GeV}$ in the central calorimeters. The enclosing muon chambers detect muon hits and the muon finder algorithms in the H1 reconstruction software classify muons in quality grades as follows:

- Grade 1 as highest quality grade links a well-measured track in the instrumented iron to a central track by a minimal-χ^2 fit:

  $$\chi^2 = (\vec{p}_{trk} - \vec{p}_{iron})^T V^{-1} (\vec{p}_{trk} - \vec{p}_{iron}) \ , \qquad (4.1)$$

  where V denotes the sum of covariance matrices of the central track and iron track.

- For muons of grade 2 the requirement of a high link probability is replaced by a minimal distance in $\eta\phi$ between an extrapolated central track and an iron track of 0.5.

- Grade 3 muons are detected by the Tail Catcher which measures energy leaking through the LAr calorimeter. For discrimination between hadronic energy leaking and energy from muons certain cuts are implied for grade 3:
  - Maximal distance in $\eta\phi$ between a Tail Catcher cluster and an extrapolated central track of 0.5;
  - At least one associated LAr cluster;
  - Associated LAr cluster energy below $8\,\mathrm{GeV}$;
  - Minimal mean distance of LAr energy deposits to LAr edge of $40\,\mathrm{cm}$.

- Muons with grade 4 are muons which are stopped in the calorimeter before reaching the muon system. These muons are isolated and show a typical minimal ionising particle pattern in the LAr calorimeter. Due to large background from misidentified hadronic energy this muon identification is not used in this analysis.

- Muons identified by the forward muon detector (FMD) are classified as grade 5. An additional matching high quality forward track with $\theta_\mu < 17^\circ$ is required here.

Hadronic final state and jets

The hadronic final state (HFS) is reconstructed from the deposits in the LAr calorimeter in combination with tracking information. All tracks and clusters not associated to an isolated electron or a muon are combined to particles of the HFS [52, 53].

Due to confinement quarks and gluons transform into showers of hadrons through fragmentation. The low transverse momentum of these hadronic daughter particles with respect to the initial parton momentum leads to the production of collimated jets in the detector. In this analysis these jets are reconstructed using a k_T-algorithm [54] with a p_T-weighted recombination scheme where jets are considered to be massless:

$$m_{jet} = 0, \quad E_{T,jet} = p_{T,jet} = \sum_i p_{T,i}, \quad \eta_{jet} = \frac{\sum_i p_{T,i}\eta_i}{\sum_i p_{t,i}}, \quad \phi_{jet} = \frac{\sum_i p_{T,i}\phi_i}{\sum_i p_{t,i}}. \tag{4.2}$$

Here, the sums run over the particles i in a jet-cluster found by the k_T-algorithm with an R_0-value of 1.0 [55, 56].

4.3.2 Kinematic variables

Electron method

Events with a well measured scattered electron are preferably reconstructed with the electron method. Here, the kinematic information is taken from the detection of the scattered electron alone. Eqs. 3.1 and 3.2 show that the measurement of the electronic energy is in principle more accurate than the determination of the hadronic energy. The kinematic variables can be determined by

$$Q_e^2 = 2E_e^0 E_e'(1 + \cos\theta_e) \tag{4.3a}$$

$$y_e = 1 - \frac{E_e'}{2E_e^0}(1 - \cos\theta_e) \, . \tag{4.3b}$$

The error on the variables is given by

$$\frac{\delta Q_e^2}{Q_e^2} = \frac{\delta E_e'}{E_e'} \oplus \tan\frac{\theta_e}{2} \cdot \delta\theta_e \tag{4.4a}$$

$$\frac{\delta y_e}{y_e} = \frac{y_e - 1}{y_e} \cdot \frac{\delta E_e'}{E_e'} \oplus \frac{1 - y_e}{y_e} \cot\frac{\theta_e}{2} \cdot \delta\theta_e \tag{4.4b}$$

$$\frac{\delta x_e}{x_e} = \frac{1}{y_e} \cdot \frac{\delta E_e'}{E_e'} \oplus \left(\tan\frac{\theta_e}{2} + \frac{1 - y_e}{y_e}\cot\frac{\theta_e}{2}\right) \cdot \delta\theta_e \, . \tag{4.4c}$$

It is noticeable that the error on x_e is large for small values of y_e and hence many DIS analyses apply a phase space cut of $y_e > 0.1$.

Hadron method

For CC DIS the hadron method can be used. The kinematics are exclusively determined by the hadronic final state. By summing over all hadronic particles h in the event, Q^2 and y follow as

$$Q^2_H = \frac{\left(\sum_h p^h_x\right)^2 + \left(\sum_h p^h_y\right)^2}{1-y} \equiv \frac{p^2_{T,H}}{1-y} \quad (4.5a)$$

$$y_H = \frac{\sum_h E^h - p^h_z}{2E^0_e} \equiv \frac{(E-p_z)_H}{2E^0_e} \,. \quad (4.5b)$$

In events without a detected scattered electron, the momentum balance with respect to the direction of the incident electron

$$E - p_z \equiv \sum_i E_i(1-\cos\theta_i) \,, \quad (4.6)$$

where the sum runs over all energy deposits i in the detector, is identical to the value of $(E-p_z)_H$. NC DIS events with a well measured electron hence show a peak in the $E-p_z$ distribution at a value of $2E^0_e$, i.e. twice the electron beam energy of $27.6\,\mathrm{GeV}$.

Double-angle method

Alternatively it is also possible to combine information from the leptonic and hadronic parts of the event to reconstruct the kinematics. The double-angle method exploits the scattering angle of the outgoing lepton and the effective angle of the hadronic system. A major advantage of this method is an almost complete insensitivity to the energy scale: calibration uncertainties and energy loss before the calorimeter play no role in first order. One can construct the angle of the hadronic system as follows [57]:

$$\cos\gamma_H = \frac{p^2_{T,H} - (E-p_z)^2_H}{p^2_{T,H} + (E-p_z)^2_H} \quad (4.7)$$

The kinematic event variables expressed in γ_H and the scattering angle of the outgoing lepton are:

$$Q^2_{\mathrm{da}} = 4E^{0\,2}_e \frac{\sin\gamma_H(1+\cos\theta_e)}{\sin\gamma_H + \sin\theta_e - \sin(\theta_e+\gamma_H)} \quad (4.8a)$$

$$y_{\mathrm{da}} = \frac{\sin\theta_e(1-\cos\gamma_H)}{\sin\gamma_H + \sin\theta_e - \sin(\theta_e+\gamma_H)} \,. \quad (4.8b)$$

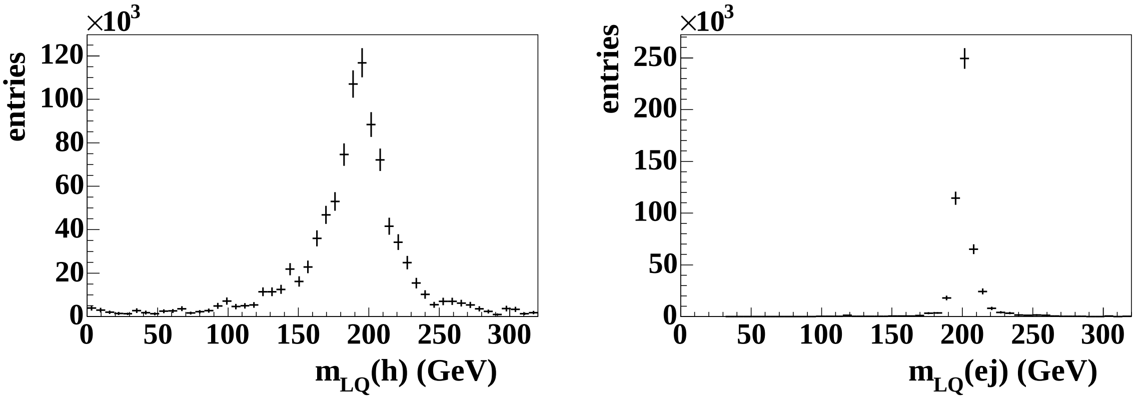

FIGURE 4.5: Reconstructed mass of a 200 GeV $\tilde{S}^L_{1/2}$ with the hadron method $m_{\mathrm{LQ}}(\mathrm{h}) = \sqrt{sx_{\mathrm{H}}}$ (left) and with the double-angle method between the quark-jet and an electron from the tau decay $m_{\mathrm{LQ}}(\mathrm{ej}) = \sqrt{sx_{\mathrm{ej}}}$ (right) after the LFV process $e^+p \rightarrow \tilde{S}^L_{1/2} \rightarrow \tau^+q$. Depicted are generated signal events after reconstruction and simulation of the detector response.

4.3.3 Mass resolution

For this analysis the double-angle method is the preferred reconstruction method. In case of LFV, the outgoing lepton is either a muon or a tau instead of the scattered electron. The energy measurement of a muon is not precise enough to be used for the electron method. Whereas the scattering angles of the muon and the quark jet used in the double-angle method yield the best mass resolution with $m^{\mathrm{rec}}_{LQ} = \sqrt{sx_{\mathrm{da}}}$. In case of a tau lepton in the final state hadronic tau decay products would require a clear separation from the hadronic deposits of the scattered quark and the neutrinos from the tau decay lead to expected missing energy. Hence, the scattering angles of the tau candidate and the quark jet determine the kinematics most accurately through the double-angle method.

Fig. 4.5 illustrates the difference in leptoquark mass resolution for the hadron method compared to the double-angle method between the quark-jet and an electron from the tau decay after the LFV process $e^+p \rightarrow \tilde{S}^L_{1/2} \rightarrow \tau^+q$. After full reconstruction and simulation of the detector response the generated signal events show for a 200 GeV scalar leptoquark a mass resolution of about 5 GeV with the double-angle method whereas the hadron method yields a resolution of more than 20 GeV.

4.4 Calibration

4.4.1 Electromagnetic energy

The electron energy is determined from clusters in the electromagnetic calorimeter. The standard calibration method developed in [51] exploits the over-constrained kinematics in NC DIS

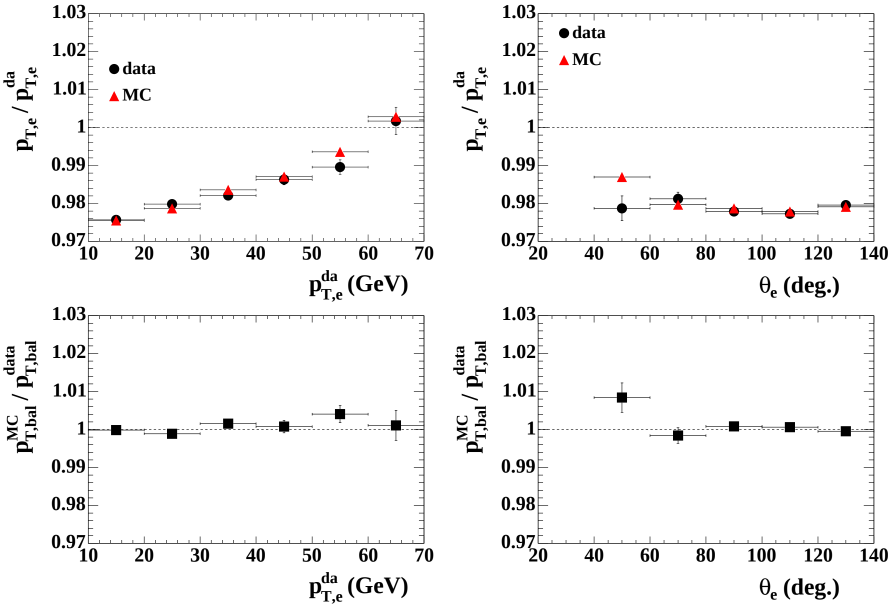

FIGURE 4.6: Electron calibration in a NC DIS sample as a function of the transverse momentum of the electron reconstructed with the double-angle method, $p_{T,e}^{\text{da}} = \sqrt{Q^2_{\text{da}}(1 - y_{\text{da}})}$, and as a function of the electron polar angle θ_e.

events (see Eqs. 2.6). As the double-angle method is nearly independent from the energy calibration, it can be used to calibrate electromagnetic energy. The mean values of E_e/E_e^{da} in fine bins of z and ϕ defined by the impact position of the electron track on the LAr surface yield calibration factors. In addition to the spatial binning the calibration is performed in regions of p_T.

The calibration dependence on θ_e and $p_{T,e}$ was checked in a NC DIS sample with a high-energy electron, i.e. $p_{T,e} > 16\,\text{GeV}$. In Fig. 4.6 the mean value from a truncated Gaussian fit to the $p_{T,\text{bal}} = p_{T,e}/p_{T,e}^{\text{da}}$ distribution is plotted for data and MC simulation as a function of $p_{T,e}^{\text{da}}$ and θ_e. The lower plots show the relative discrepancy in calibration between data and MC simulation. The slight dependencies on $p_{T,e}^{\text{da}}$ and θ_e are described by the MC simulation within 1%. Since the statistics of DIS events in the forward region are limited, this calibration check only covers values of $\theta_e > 40°$. With additional elastic QED Compton events and exclusive two photon e^+e^- production events the calibration in the forward region was shown in [51] to be precise with an error of 3%.

4.4.2 Hadronic energy

The determination of the hadronic energy scale is less accurate than the measurement of electromagnetic energy. Therefore, it can be adjusted by using the precisely measured electron en-

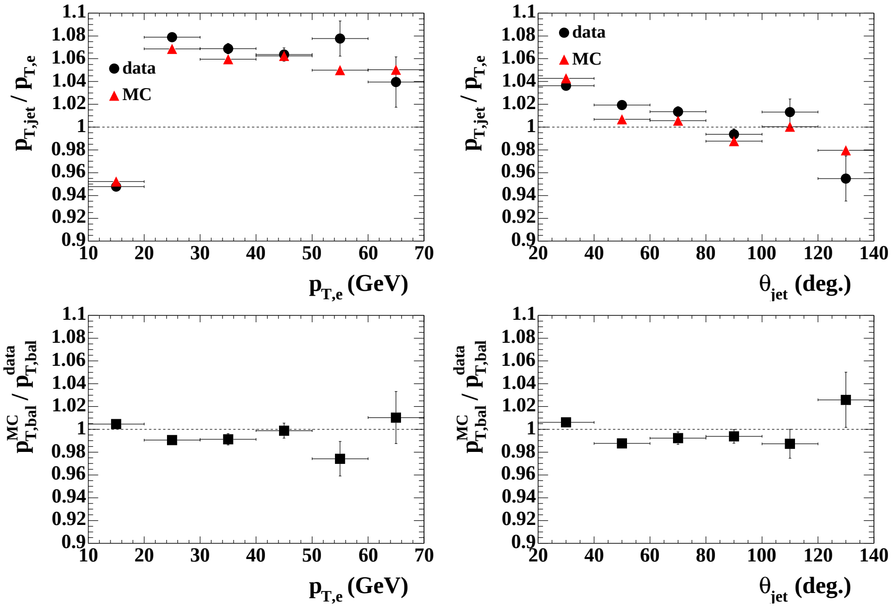

FIGURE 4.7: Jet calibration in a NC DIS sample as a function of the transverse momentum of the electron $p_{T,e}$ and as a function of the jet polar angle θ_{jet}.

ergy in NC DIS events. The HADROO2 package [53] was used here to identify the HFS and to calibrate jets. After removal of central tracks and calorimeter clusters associated to isolated lepton candidates, the algorithm uses the event vertex, non-associated tracks and pre-calibrated clusters as input objects to build the HFS. A high-Q^2 NC DIS sample with $p_{T,e} > 10\,\mathrm{GeV}$, exactly one jet and a precise double-angle determination is used in HADROO2 to adjust the hadronic energy scale in bins of $p^{\mathrm{da}}_{T,e} \approx p^{\mathrm{da}}_{T,jet}$ and θ_{jet}.

Fig. 4.7 shows the mean value from a truncated Gaussian fit to the $p_{T,\mathrm{bal}} = p_{T,jet}/p_{T,e}$ distribution in data and MC simulation as a function of $p_{T,e}$ and θ_{jet}. Deviations between data and MC simulation are well covered by a systematic error of 4% applied to the hadronic energy scale.

4.5 SM background processes

4.5.1 High-Q^2 NC/CC DIS

In Sec. 2.2 the NC/CC DIS cross section is discussed in more detail. In the search for LFV processes with a tau-quark pair in the final state, the misidentification of the scattered electron as a hadronic energy deposit represents a potential background source. Especially near ϕ-cracks or other inefficient parts of the electromagnetic calorimeter such misidentifications must be studied.

For this analysis the NC DIS background samples produced with the event generator RAPGAP [58] are split into phase space regions of Q^2 and y as can be seen in Tab. 4.2. Included in addition is at least one generated hadronic jet or a generated radiated photon with $p_T > 10\,\mathrm{GeV}$. The proton PDFs are parametrised using CTEQ5L [15] and hadronisation is performed using JETSET [59] parton showers with Lund string fragmentation.

The CC DIS events are generated with DJANGO [60] and QCD radiation based on the Colour Dipole Model (CDM) [61, 62].

4.5.2 Photoproduction

Photoproduction (γP) is a scattering process with one of the highest cross sections at HERA ($\sim 150\,\mu\mathrm{b}$). A quasi-real photon ($Q^2 \ll 1\,\mathrm{GeV}$) is emitted from the electron line and couples to a parton from the proton. In Fig. 4.8 first order Feynman diagrams of photoproduction processes leading to a dijet signature are illustrated. In case of the photon interacting directly with the parton the photoproduction is called *direct* (Fig. 4.8a) whereas *resolved* photoproduction (Fig. 4.8b) refers to cases where the photon fluctuates through hadronic pair production before the interaction takes place.

Due to the high cross section these processes are an important background source, especially in the search for tau-quark pairs with a subsequent hadronic tau decay. Additionally, hadrons wrongly identified as a muon might mimic a muon-quark pair signal from a LFV process.

The photoproduction background samples in this analysis are generated with the event generator PYTHIA [63]. CTEQ5L [15] serves here as the proton PDF parametrisation and the photonic parton distribution GRV-LO [64] is applied. As PYTHIA only contains leading order $2 \rightarrow 2$ processes, absolute dijet and 3-jet cross sections are underestimated. As a consequence the total photoproduction background has to be scaled by a factor 1.2 in this analysis [65].

The statistics of the individual samples can be found in Tab. 4.2. The samples are split into different phase space regions of $\hat{p}_T$ which is defined as the lower value of the transverse momenta of the two outgoing partons after the hard subprocess.

4.5.3 Lepton-pair production

Lepton-pair production as depicted in Fig. 4.8c-e contributes as background because they may lead to high momentum leptons in the final state. In particular, inelastic dimuon events with one unidentified muon may fake the LFV signal signature of one high-p_T muon plus hadronic energy.

The samples summarised in Tab. 4.2 include elastic, quasi-elastic and inelastic lepton-pair production. Elastic events $ep \rightarrow el^+l^-X$ only show the two leptons in the final state with the electron and the intact proton escaping the detector through the backward and forward beam pipe. In case of a detected scattered electron due to a large enough value of Q^2 or W the event

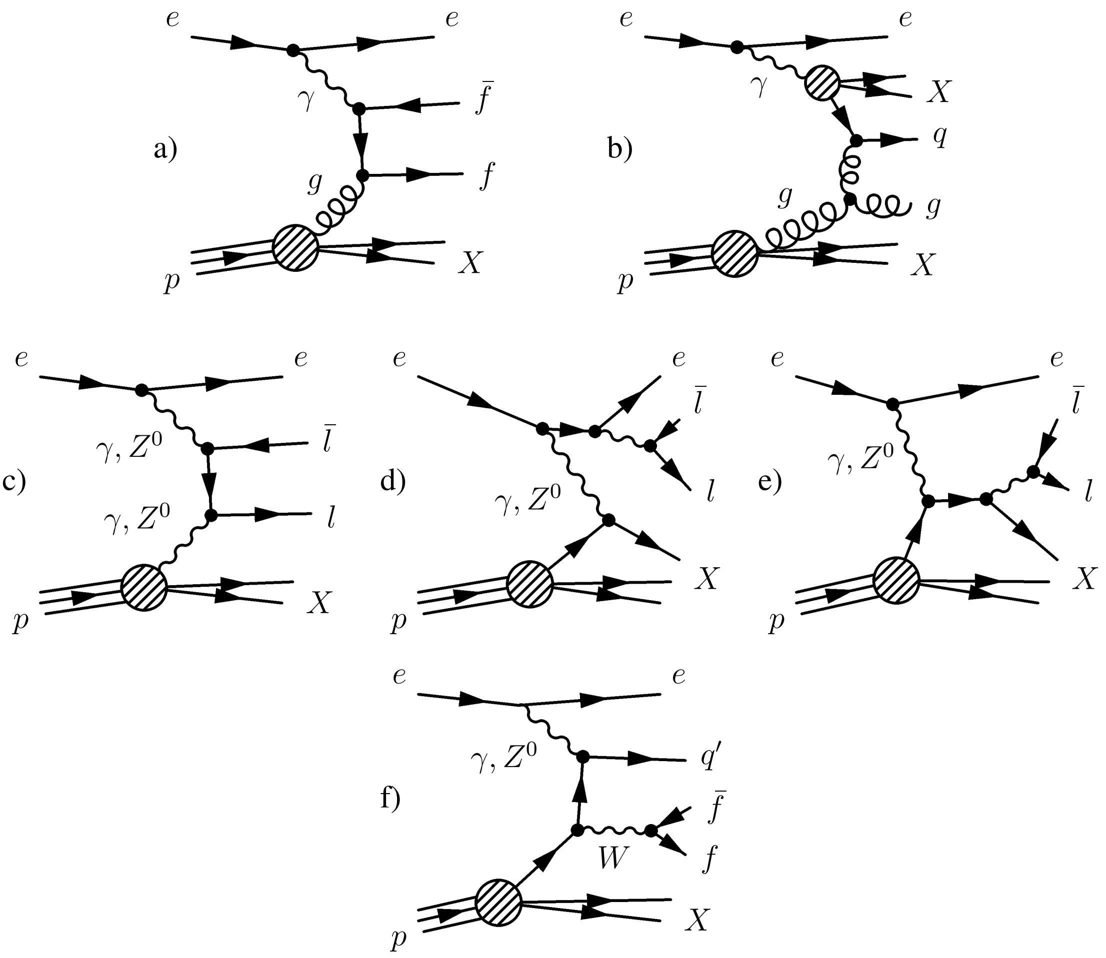

FIGURE 4.8: Dominant tree level Feynman diagrams of SM background processes in addition to NC/CC DIS. a) Dijets in direct photoproduction, b) dijets in resolved photoproduction, c-e) lepton-pair production and f) W-production.

is considered to be inelastic. The proton remnant may be detected in the forward region in quasi-elastic events with $W > m_P$ and $Q^2 < 4\,\mathrm{GeV}$.

The phase space region was chosen such that at least one lepton in the event fulfils the requirements $p_{T,l} > 8\,\mathrm{GeV}$ and $4^\circ < \theta_l < 160^\circ$.

4.5.4 W-production

Another source for isolated high-p_T leptons is W-production. Fig. 4.8f illustrates the dominant W-production process $ep \rightarrow eW^{\pm}X$. The simulated W-production samples are created with the event generator EPVEC [66] and include events with either leptonic ($e\bar{\nu}_e$, $\mu\bar{\nu}_\mu$, $\tau\bar{\nu}_\tau$) and hadronic W decays. Both W charges are considered.

4.5.5 Background summary

All background samples used in this analysis are summarised with statistics and phase space restrictions in Tab. 4.2 for the e^+p sample. Similar background sets are employed for the e^-p analysis.

Generator	SM process	phase space	events	$\int \mathcal{L}dt\,(\mathrm{pb}^-1)$
RAPGAP	NC DIS	$Q^2 > 4\,\mathrm{GeV}^2,\ y > 0.08$	1200000	308.55
		$Q^2 > 100\,\mathrm{GeV}^2,\ y > 0.08$	1000000	220.01
		$Q^2 > 400\,\mathrm{GeV}^2,\ y > 0.08$	800000	879.64
		$Q^2 > 1000\,\mathrm{GeV}^2,\ y > 0.08$	100000	408.94
		$Q^2 > 2500\,\mathrm{GeV}^2,\ y > 0.08$	100000	1757.18
		$Q^2 > 5000\,\mathrm{GeV}^2,\ y > 0.08$	100000	6881.47
		$Q^2 > 10000\,\mathrm{GeV}^2,\ y > 0.08$	100000	35994.80
		$Q^2 > 20000\,\mathrm{GeV}^2,\ y > 0.08$	200000	635107.37
RAPGAP	NC DIS	$Q^2 > 100\,\mathrm{GeV}^2,\ y \leq 0.08$	300000	47.72
		$Q^2 > 400\,\mathrm{GeV}^2,\ y \leq 0.08$	200000	995.75
		$Q^2 > 1000\,\mathrm{GeV}^2,\ y \leq 0.08$	100000	3846.37
DJANGO	CC DIS	$Q^2 > 100\,\mathrm{GeV}^2$	600000	16081.82
		$Q^2 > 10000\,\mathrm{GeV}^2$	1000000	874120.83
GRAPE	ee-Prod.	$p_{T,l} > 8$ GeV, $4^\circ < \theta_l < 160^\circ$	151649	30000.00
	$\mu\mu$-Prod.	$p_{T,l} > 8$ GeV, $4^\circ < \theta_l < 160^\circ$	119276	50000.19
	$\tau\tau$-Prod.	$p_{T,l} > 8$ GeV, $4^\circ < \theta_l < 160^\circ$	111596	100000.01
PYTHIA	dir. γP (uds)	$\hat{p}_T > 5\,\mathrm{GeV}$	865955	30.68
		$\hat{p}_T > 10\,\mathrm{GeV}$	249405	100.18
		$\hat{p}_T > 15\,\mathrm{GeV}$	400000	1000.18
		$\hat{p}_T > 25\,\mathrm{GeV}$	643736	9998.84
		$\hat{p}_T > 40\,\mathrm{GeV}$	69889	9975.93
		$\hat{p}_T > 75\,\mathrm{GeV}$	18974	149992.09
PYTHIA	dir. γP (c)	$\hat{p}_T > 5\,\mathrm{GeV}$	317194	30.05
		$\hat{p}_T > 10\,\mathrm{GeV}$	80873	100.21
		$\hat{p}_T > 15\,\mathrm{GeV}$	144519	1001.93
		$\hat{p}_T > 25\,\mathrm{GeV}$	121221	10003.26
		$\hat{p}_T > 40\,\mathrm{GeV}$	7694	10009.24
PYTHIA	dir. γP (b)	$\hat{p}_T > 5\,\mathrm{GeV}$	33178	30.1
		$\hat{p}_T > 10\,\mathrm{GeV}$	15513	99.99
		$\hat{p}_T > 15\,\mathrm{GeV}$	31765	997.45
		$\hat{p}_T > 25\,\mathrm{GeV}$	28700	10018.15
		$\hat{p}_T > 40\,\mathrm{GeV}$	1872	10001.6
		$\hat{p}_T > 5\,\mathrm{GeV}$	2000000	11.58
		$\hat{p}_T > 10\,\mathrm{GeV}$	812524	77.62

PYTHIA	res. γP (uds)	$\hat{p}_T > 15\,\mathrm{GeV}$	500000	428.77
		$\hat{p}_T > 25\,\mathrm{GeV}$	700000	10000.63
		$\hat{p}_T > 40\,\mathrm{GeV}$	44207	10011.1
		$\hat{p}_T > 75\,\mathrm{GeV}$	3506	148369.33
PYTHIA	res. γP (c)	$\hat{p}_T > 5\,\mathrm{GeV}$	12836	29.37
PYTHIA	res. γP (b)	$\hat{p}_T > 5\,\mathrm{GeV}$	4484	30.76
PYTHIA	prompt γP	$\hat{p}_T > 10\,\mathrm{GeV}$	30000	5011.02
		$\hat{p}_T > 20\,\mathrm{GeV}$	10000	32580.64
		$\hat{p}_T > 40\,\mathrm{GeV}$	10000	1300260.07
EPVEC	W-Prod. (lep.)	$Q^2 > 4\,\mathrm{GeV}^2$	87255	200137.44
	W-Prod. (had.)	$Q^2 > 4\,\mathrm{GeV}^2$	101499	100009.78

TABLE 4.2: Summary of the e^+p SM background samples employed in the analysis. Similar numbers are found in the e^-p analysis.

4.5.6 Background systematics

The systematic errors on the SM expectation can be separated into experimental and theoretical uncertainties. The experimental uncertainties are evaluated from systematic upward and downward shifts of measured quantities:

- For selections with an electron in the final state the electromagnetic energy scale is varied universely by 3%. The spatial uncertainty due to misalignment is estimated to be $3\,\mathrm{mrad}$ in θ and $1\,\mathrm{mrad}$ in ϕ.
- The muon energy is assumed to be measured with an uncertainty of 5%. The spatial resolution is taken to be $3\,\mathrm{mrad}$ in θ and $1\,\mathrm{mrad}$ in ϕ.
- An error on the hadronic energy scale of 2% is applied for the LAr measurement and 2% for hadrons with transverse momenta reconstructed from tracks. The values for θ and ϕ are fluctuated by $20\,\mathrm{mrad}$.
- The determination of the integrated luminosity gives an overall uncertainty on the SM expectation of $\pm 1.5\%$.

The individual sources for systematic uncertainties are added in quadrature. Uncertainties on the proton PDF are not taken into account in the systematic error on the stated expected SM background, but they do enter in the limit calculation in correlation with PDF uncertainties in the signal expectation (see Sec. 7.2.1).

Tab. 4.3 summarises the systematic errors accounting for theoretical uncertainties on the calculated cross sections in the individual MC event generators. The relatively large error of 30% on Photoproduction and CC DIS is due to uncertainties on higher-order corrections.

SM Process	Event generator	Syst. error (%)
NC DIS	RAPGAP	10
CC DIS	DJANGO	30
γP	PYTHIA	30
ee,$\mu\mu$,$\tau\tau$-Prod.	GRAPE	10
W-Prod.	EPVEC	15

TABLE 4.3: Systematic theoretical uncertainties for the dominant SM expectations applied in this analysis.

4.6 Signal simulation

The simulation of the LFV signal is performed with a modified version of the LEGO [67] event generator. Initial QED radiation is included in LEGO in the collinear approximation (Weizsäcker-Williams). The perturbative part of the initial and final state parton showers follow the DGLAP [68, 69, 70] evolution equations, whereas the JETSET [59] parton showers with Lund string fragmentation are used for the non-perturbative hadronisation. As neutrino flavour is not observable at HERA experiments, only the neutral current decay channels of the leptoquarks S_0^L, V_1^L, V_0^L and S_1^L are investigated.

The signal expectation can not be easily approximated by a basic function in the m_{LQ}-λ_{ei} parameter space. In particular for high masses near the kinematic boundary the cross section dependence on λ_{ei} is intriguingly strong. A production of many event samples with leptoquarks of a certain mass and coupling strength is technically awkward and faces the challenge of interpolation or fitting procedures that need to be applied to cover the complete phase space. To overcome this potential problem and to allow for a model independent interpretation of the results, a high-statistics generic signal sample is produced with a modified version of the LEGO generator, where the matrix element in the s-channel (see Eq. (2.18)) is replaced by $\hat{s}\times10^{-15}$. This ensures enough statistics of simulated events all over the phase space $0 < x < 1$ before folding with the proton PDF. Knowing the exact cross section from Eqs. (2.18),(2.20) the events are reweighted according to the generated x, Q^2 and x_e and a distinct model assumption with a certain leptoquark type, m_{LQ}, λ_{ei} and β_{LFV} to deduce the signal selection

Generator	generic signal	phase space	events	$\int \mathcal{L}dt\,(\mathrm{pb}^{-}1)$
LEGO	$e^+p \rightarrow \mathrm{LQ} \rightarrow \mu^+q$	$Q^2 > 4\,\mathrm{GeV}^2$	500000	284438.38
	$e^+p \rightarrow \mathrm{LQ} \rightarrow \tau^+q$	$Q^2 > 4\,\mathrm{GeV}^2$	500000	284438.33
	$e^-p \rightarrow \mathrm{LQ} \rightarrow \mu^-q$	$Q^2 > 4\,\mathrm{GeV}^2$	500000	284438.25
	$e^-p \rightarrow \mathrm{LQ} \rightarrow \tau^-q$	$Q^2 > 4\,\mathrm{GeV}^2$	500000	284438.40

TABLE 4.4: Summary of produced LFV signal samples.

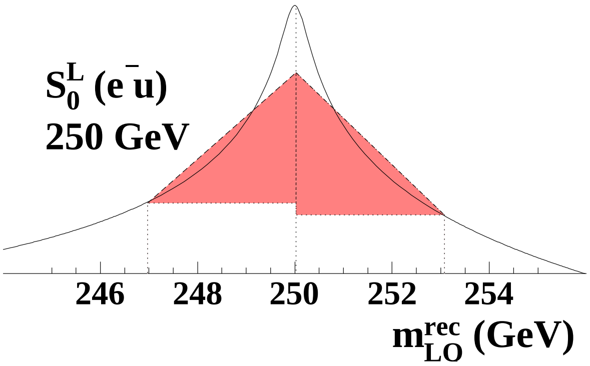

FIGURE 4.9: The smoothing of a simulated leptoquark mass peak. To avoid large weights the Lorentz peak is replaced by a triangular shape with the same integral in an area of ±3 GeV around the nominal leptoquark mass.

efficiency. x_e represents here the energy fraction E'_e/E^0_e of the electron after initial state radiation (ISR) of a collinear photon. It should be noted that, taking ISR into account, the effective centre-of-mass energy for the hard subprocess in Eq. (2.17a) is reduced to $\hat{s} = sxx_e$.

The reweighting factors w which are applied on each simulated event are deduced from the exact double differential cross section (Eqs. (2.18),(2.20)) as follows:

$$w(\mathrm{LQ}, m_{\mathrm{LQ}}, \lambda_{ei}, \beta_{\mathrm{LFV}}, x, Q^2, x_e) = \frac{\frac{d^2\sigma_{\mathrm{exact}}}{dxdQ^2}(\mathrm{LQ}, m_{\mathrm{LQ}}, \lambda_{ei}, \beta_{\mathrm{LFV}}, x, Q^2, x_e)}{\frac{d^2\sigma_{\mathrm{generic}}}{dxdQ^2}(x, Q^2, x_e)} \, . \tag{4.9}$$

In case of resonant leptoquark production the event weight can take very large values for events with a generated value of x near the peak at $m^2_{LQ}/\hat{s}$. In particular for small couplings λ_{ei} and therefore small leptoquark widths the finite statistics in the generic signal sample may lead to a signal cross section dominated by a few events with very large weights.

To overcome this potentially large statistical error the mass peak is smoothed. The smoothing is performed by replacing the Lorentz peak of the reconstructed mass distribution by a triangular shape around the nominal leptoquark mass. The smoothing is schematically illustrated in Fig. 4.9. In order that the reweighting results in the correct number of expected signal events under a certain model hypothesis, the integral of the distribution is unchanged by the smoothing. The smoothing area is chosen to be $\pm 3\,\mathrm{GeV}$, which is smaller than the detector mass resolution of about $5\,\mathrm{GeV}$ (see Fig. 4.5).

The main advantage of the reweighted generic signal MC over a fixed set of signal MC samples parametrising signal selection efficiencies is the possibility to describe leptoquark models with arbitrary parameter sets. This is important for those regions of the parameter space where the analysis has enhanced sensitivity to small parameter changes. Using this approach, the delicate transition region from resonant production to high-mass contact interaction regions, i.e. leptoquarks with masses around $300\,\mathrm{GeV}$ and arbitrary coupling, is treated correctly by the reweighting analysis method.

4.6.1 Signal systematics

The systematic shifts on measured quantities as described for the SM background in Sec. 4.5.6 are also applied on the signal expectation to estimate systematic uncertainties on the signal selection efficiency from detector effects.

The main theoretical uncertainty on the signal cross section originates from uncertainties on the parton densities. In analogy to [71], this uncertainty is estimated to be 5% for leptoquarks coupling to u-quarks and varies between 7% at low leptoquark masses and 30% around $290\,\mathrm{GeV}$ for leptoquarks coupling to d-quarks. The correlation between different statistical channels (see Sec. 7.2.1) is taken into account for the statistical interpretation and limit calculation. For the correlation procedure the method developed in [72] and applied in [71] is used.

4.7 NC DIS control sample

LFV events with a $\tau + q$ final state and a subsequent electronic tau decay yield event topologies very similar to those in high-Q^2 NC DIS. The high-Q^2 NC DIS is used as a check for the general analysis methods that are applied.

Tab. 4.5 summarises the requirements for this NC DIS sample. As the electron from a tau decay in a LFV event tends to be produced in the forward direction, the electron polar angle is chosen to be in the range $5° < \theta_e < 120°$. The kinematic domain is restricted to $Q^2_{da} > 1000\,\mathrm{GeV}^2$ and $y_{da} > 0.1$.

Fig. 4.10 shows some reconstructed measured quantities in the e^+p data sample. The SM NC DIS background process describes the data very well. A reconstructed hypothetical LFV signal with a $200\,\mathrm{GeV}$ $\tilde{S}^L_{1/2}$ and a $\tau + q$ final state with subsequent electronic tau decay is also depicted with arbitrary normalisation.

Quantity	Requirement
n_{jets}	≥ 1
n_e	≥ 1
$p_{T,jet1}$	$> 15\,\mathrm{GeV}$
$p_{T,e}$	$> 10\,\mathrm{GeV}$
θ_e	$5° < \theta_e < 120°$
Q^2_{da}	$> 1000\,\mathrm{GeV}^2$
y_{da}	> 0.1

TABLE 4.5: Selection criteria for the NC DIS control sample. The subscripts e and $jet1$ denote the scattered electron and the highest-p_T jet respectively.

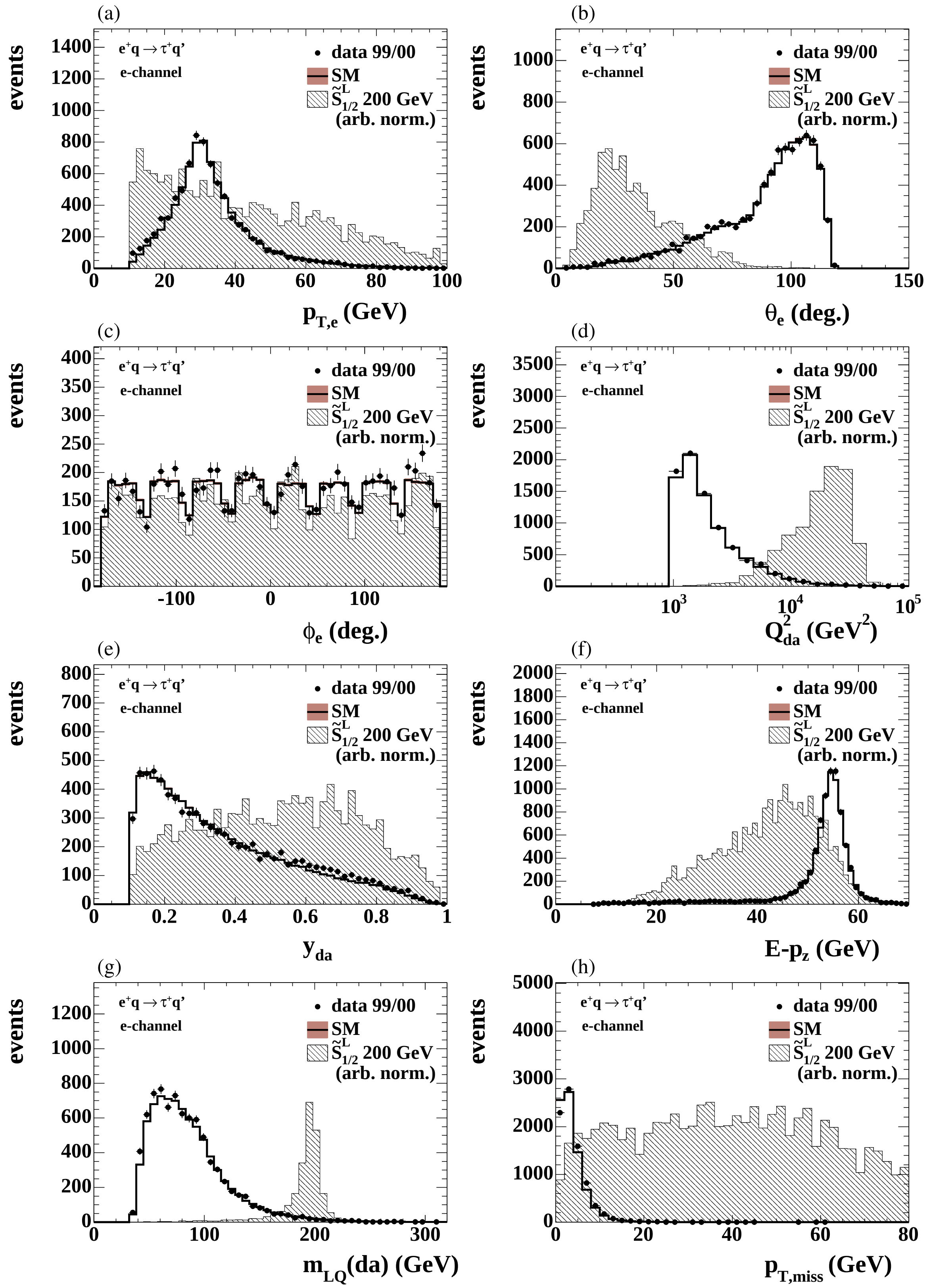

FIGURE 4.10: Reconstructed quantities in a NC DIS control sample. The description of the 98/99 e^-p data by the MC simulation is as good as that of the 99/00 e^+p data shown here. This selection serves as a preselection in the performed search for LFV with electronically decaying taus (see Sec. 6.2).

Chapter 5

Selection of muon-quark pairs

This chapter gives an insight into the selection of muon-quark pairs that can be related to the decay product of a resonantly produced leptoquark. The selection is performed in three steps leading to the final mass spectrum of a hypothetical leptoquark. With regard to exclusion limits on model parameters, the signal selection efficiency is also studied.

5.1 Muon preselection

After applying the general data quality criteria described in Sec. 4.1 and selecting events triggered by the triggers discussed in Sec. 4.2, a preselection sample for muon-quark pairs with a clearly identified high-p_T muon is selected.

The following selection criteria are applied for the muon preselection sample:

- At least one muon (see Sec 4.3.1) with a transverse momentum $p_{T,\mu} > 10\,\mathrm{GeV}$ reconstructed in the polar angle range $10^\circ < \theta_\mu < 140^\circ$.
- A minimal overall transverse momentum reconstructed from the LAr calorimeter alone: $p_{T,\mathrm{calo}} > 12\,\mathrm{GeV}$.
- At least one reconstructed jet in the event.

The large expected leptoquark mass justifies the requirement of $p_{T,\mu} > 10\,\mathrm{GeV}$. For polar angles below 10° the hadronic background is large and the muon measurement is less accurate. As the hadronic LAr calorimeter extends only up to a maximal polar angle of 140°, the upper cut on θ_μ is applied. As already discussed for the trigger selection in Sec. 4.2, high-p_T muons are expected to deposit only a small fraction of their energy in the calorimeter. This leads to a large net value of $p_{T,\mathrm{calo}}$ supposing a leptoquark decay into a muon-quark pair. For the exact determination of the kinematic variables with the double-angle method at least one reconstructed jet in the event is needed.

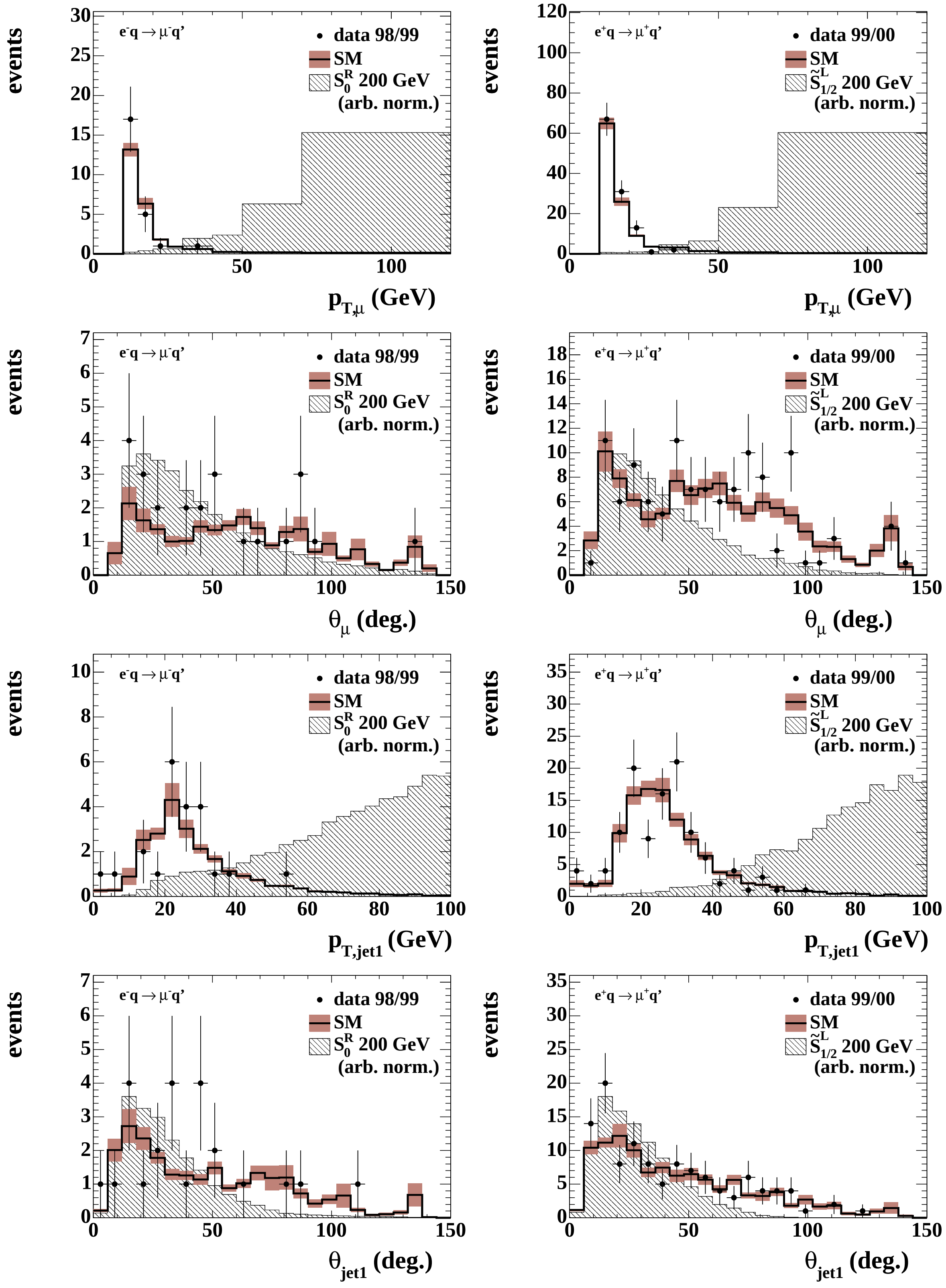

FIGURE 5.1: Muon preselection: Reconstructed transverse momentum and polar angle of the reconstructed muon and the highest-p_T jet in both data samples e^-p (left) and e^+p (right).

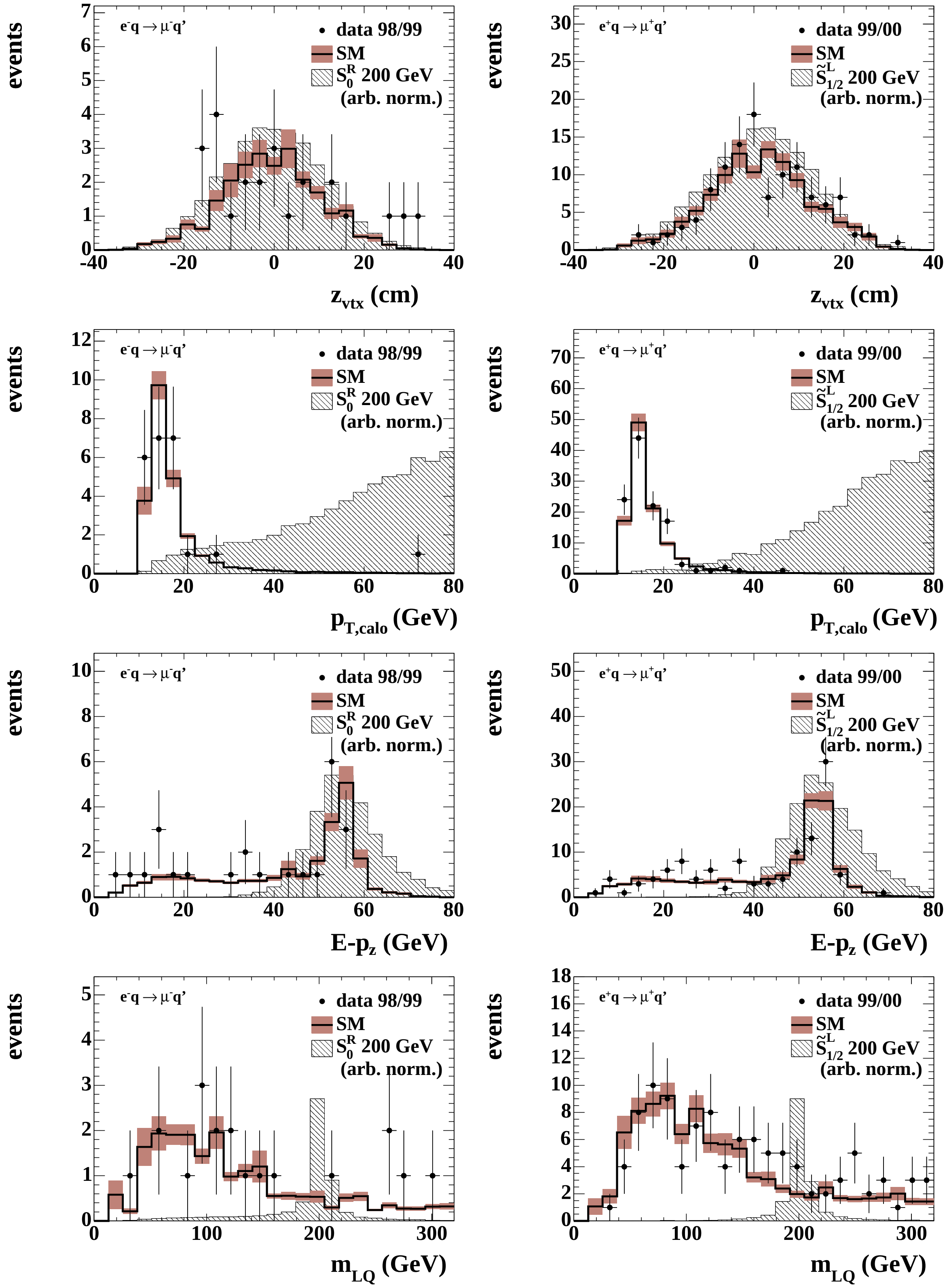

FIGURE 5.2: Muon preselection: Distributions of z_{vtx}, $p_{T,\mathrm{calo}}$, $E - p_z$ and m_{LQ} in both data samples e^-p (left) and e^+p (right).

Muon preselection		
set	98/99 e^-p	99/00 e^+p
NC	10.62 ± 1.06	50.86 ± 3.04
CC	1.49 ± 0.04	3.34 ± 0.11
γP	7.36 ± 0.39	35.90 ± 1.89
ee,$\mu\mu$,$\tau\tau$-Prod.	3.58 ± 0.04	17.27 ± 0.22
W-Prod.	0.46 ± 0.01	3.44 ± 0.11
SM tot.	23.53 ± 1.12	109.62 ± 3.59
data	24	116

TABLE 5.1: Preselection results of muon-quark pairs. Here, the error on the SM background expectation contains the statistical error only.

Already at this stage of the muon selection the statistics in the data samples are quite low as can be seen in Tab. 5.1. Nevertheless, the data is well described by the SM expectation. Fig. 5.1 and Fig. 5.2 illustrate control distributions of the muon preselection sample for both data sets e^-p and e^+p. Dominant background contributions are NC DIS and Photoproduction with a high-p_T muon stemming from the hadronisation processes in a quark-jet. Hence, the following selection step requires isolation criteria for the reconstructed muon.

5.2 Muon isolation

The SM background contamination in the preselected muon sample originates from muons as part of high-p_T jets. This is in contrast to the topology of muon-quark pairs from a leptoquark decay, which is a muon *back-to-back* to a quark-jet in the $r\phi$-plane. The muon is therefore expected to be clearly isolated as it is depicted in form of a MC simulated event display in Fig. 5.3.

The muon finder algorithms in the H1 reconstruction software already flag muons with grade 1, 2 or 3 (see Sec. 4.3.1) as *isolated* if there are not more than $5\,\mathrm{GeV}$ of energy deposits reconstructed inside a cylinder of radius $25\,\mathrm{cm}$ around the muon direction and if there are no vertex-fitted central tracks found in an $\eta\phi$-cone of size 0.5 around the muon track.

These requirements are not effective enough to seperate SM processes from events with a signal signature. Especially the energy isolation criterion is loose as muons often deposit much less than $5\,\mathrm{GeV}$ in the calorimeter. So additionally, no reconstructed jet is allowed in an $\eta\phi$-cone of size 1.0 around the muon.

From Fig. 5.3 one can not only see a clear isolation of the muon, but also a characteristic energy imbalance. A suitable variable to quantify the energy imbalance in an event is the

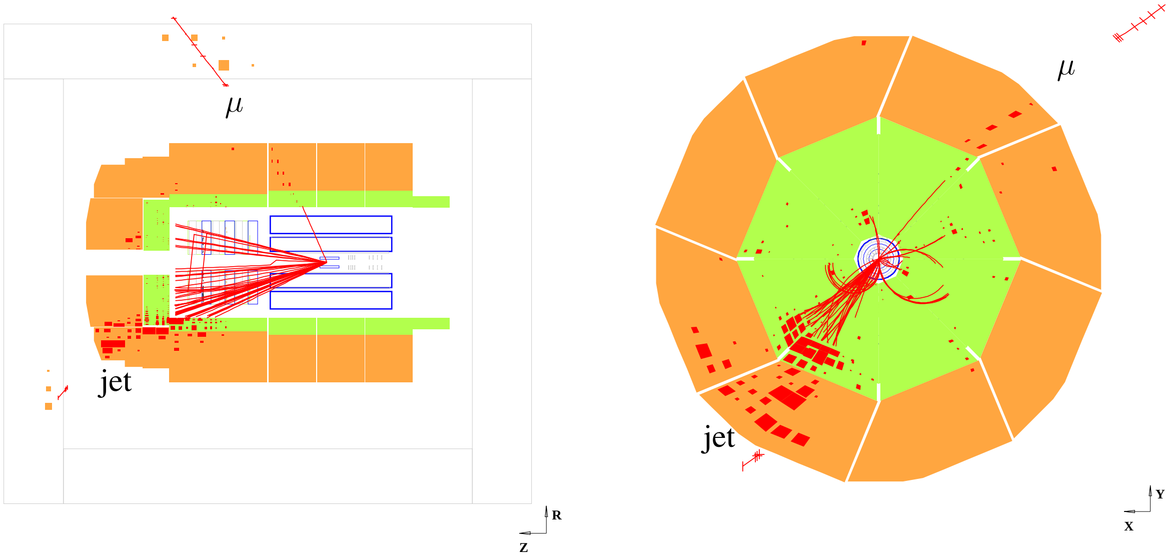

FIGURE 5.3: MC simulated event display of the signal process $ep \rightarrow \mu X$.

variable V_{ap}/V_p with

$$V_p = \sum_i \frac{\vec{p}_{T,X} \cdot \vec{p}_{T,i}}{|\vec{p}_{T,X}|} \quad \text{for} \;\; \vec{p}_{T,X} \cdot \vec{p}_{T,i} > 0 \,, \tag{5.1a}$$

$$V_{ap} = -\sum_i \frac{\vec{p}_{T,X} \cdot \vec{p}_{T,i}}{|\vec{p}_{T,X}|} \quad \text{for} \;\; \vec{p}_{T,X} \cdot \vec{p}_{T,i} < 0 \,. \tag{5.1b}$$

$\vec{p}_{T,X}$ denotes here the transverse momentum vector sum of all energy deposits i in the calorimeter. By this, the $r\phi$-plane is seperated into two hemispheres. In a signal-like event the hemisphere with $\vec{p}_{T,X} \cdot \vec{p}_{T,i} < 0$ contains the muon and adds up to V_{ap}, whereas V_p mainly reflects the sum of the quark-jet deposits. Signal events are expected to show values of V_{ap}/V_p close to zero, whereas for NC DIS and photoproduction background events V_{ap}/V_p is about one.

As an additional selection, an upper cut on the variable V_{ap}/V_p is applied at the value 0.3. Fig. 5.4a,b demonstrate the large background suppression by this cut without significantly affecting the signal selection efficiency.

After the isolation criteria and the cut on V_{ap}/V_p there are 30 data events left in the e^+p sample compared to a SM expectation of $25.56 \pm 1.50\,(\mathrm{stat.})$. The main SM background contribution with $13.97 \pm 0.21\,(\mathrm{stat.})$ events comes from $\mu\mu$-production.

The e^-p sample yields 3 data events whereas $5.22 \pm 0.52\,(\mathrm{stat.})$ are expected from the SM with a fraction of 55% coming from $\mu\mu$-production.

All selected data events passing the isolation criteria are scanned with the H1 event display. The three events in the e^-p sample are displayed in the Appendix A.

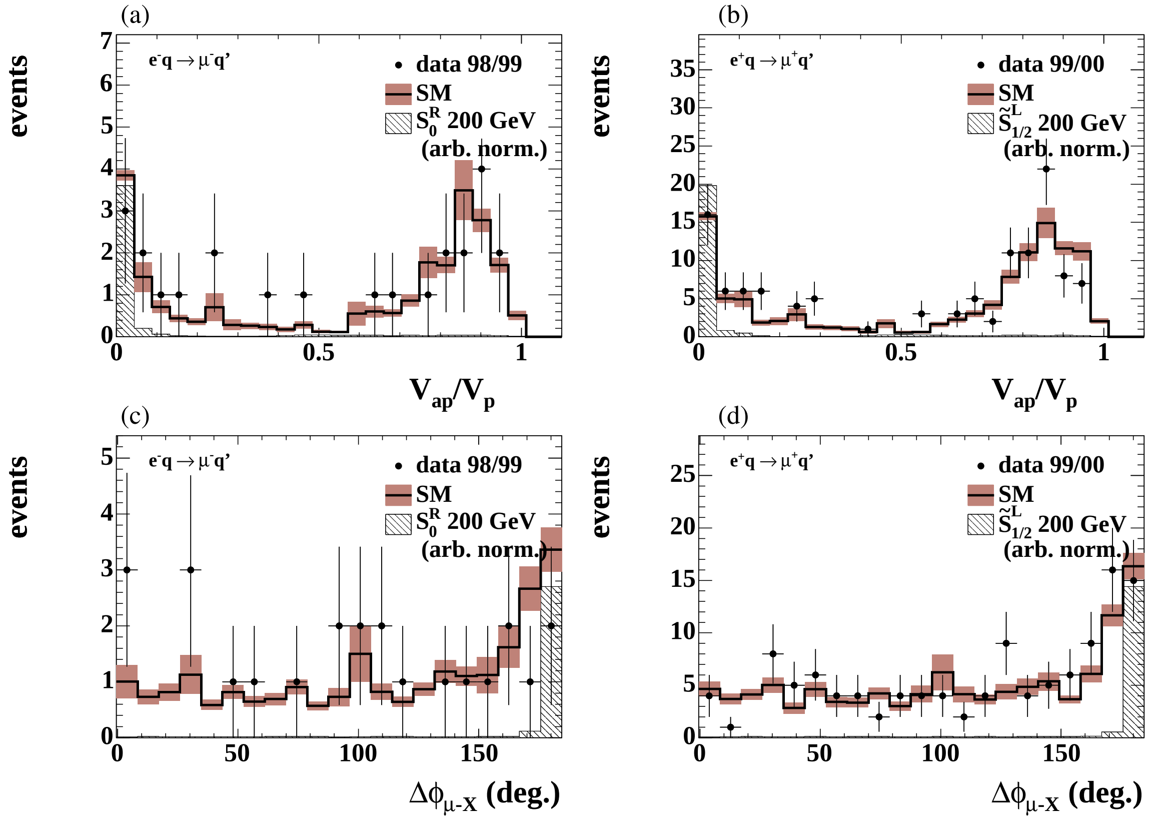

FIGURE 5.4: (a),(b): Energy imbalance in the preselected muon sample illustrated by the variable V_{ap}/V_p. (c),(d): The *back-to-back* topology measured by the distance in ϕ between the muon and the hadronic final state X in the preselected muon sample. In the final selection step $\Delta\phi_{\mu-X} > 170°$ is required.

5.3 Final selection

One can see from the $p_{T,\text{calo}}$ distribution in Fig. 5.2 that the LFV signal tends to much larger values than $12\,\text{GeV}$. Hence, a cut $p_{T,\text{calo}} > 25\,\text{GeV}$ is applied in the final selection step to reduce remaining SM background significantly. NC DIS events are rejected by an additional veto on isolated electrons.

The *back-to-back* topology can be exploited furthermore by the distance in ϕ between the muon and the hadronic final state X. The muon direction in ϕ is determined from the track here. For an accurate application of this selection criterion the polar angle of the hadronic final state must be reconstructed in the range $7° < \theta_X < 140°$. In addition, a minimal distance in ϕ between the muon and the hadronic final state of $170°$ is required.

The final selection results in the search for muon-quark pairs are listed in Tab 5.2. No data event is selected in the final sample. The expected SM background is equal to $1.03 \pm 0.11\,(\text{stat.}) \pm 0.24(\text{sys.})$ in the e^+p set and $0.18 \pm 0.01\,(\text{stat.}) \pm 0.06(\text{sys.})$ in the e^-p sample.

Muon final selection results		
data set	98/99 e^-p	99/00 e^+p
NC	0.008 ± 0.005	0.205 ± 0.128
CC	–	–
γP	0.005 ± 0.003	0.023 ± 0.015
ee,$\mu\mu$,$\tau\tau$-Prod.	0.151 ± 0.061	0.721 ± 0.228
W-Prod.	0.016 ± 0.003	0.079 ± 0.015
SM tot.	0.180 ± 0.061	1.028 ± 0.262
data	0	0

TABLE 5.2: Final selection results of the search for muon-quark pairs. The error on the expectation from SM processes incorporates the statistical error and the systematic error added in quadrature.

5.4 Signal selection efficiency

The final selection yields no candidate event for a LFV process with a muon-quark pair, not to mention any excess over the SM expectation. With regard to exclusion limits that can be derived from this result the signal selection efficiency is studied in detail.

The efficiency is determined by reweighting the selected generic MC signal events passing the final selection step with the procedure discussed in Sec 4.6. Rather than using an interpolated set of various signal assumptions incorporating the parameters *LQ-type*, $\lambda_{\mu q}$, m_{LQ} and β_{LFV} the efficiency is calculated exactly for the signal assumption at issue.

Fig. 5.5 shows the signal selection efficiencies for four leptoquark types. The selected values of Tab. 5.3 can also be read off the final selection efficiencies in Fig. 5.5. The efficiency loss after the final selection step for masses below $150\,\text{GeV}$ is due to the harsh cut $p_{T,\text{calo}} > 25\,\text{GeV}$

Muon final signal selection efficiencies					
signal		98/99 e^-p		99/00 e^+p	
F	type	$150\,\text{GeV}$	$500\,\text{GeV}$	$150\,\text{GeV}$	$500\,\text{GeV}$
2	S_0^R	58%	49%	56%	40%
2	$V_{1/2}^L$	61%	40%	58%	40%
0	V_0^R	60%	42%	59%	39%
0	$\tilde{S}_{1/2}^L$	58%	38%	56%	43%

TABLE 5.3: Some final selection efficiencies in the search for muon-quark pairs.

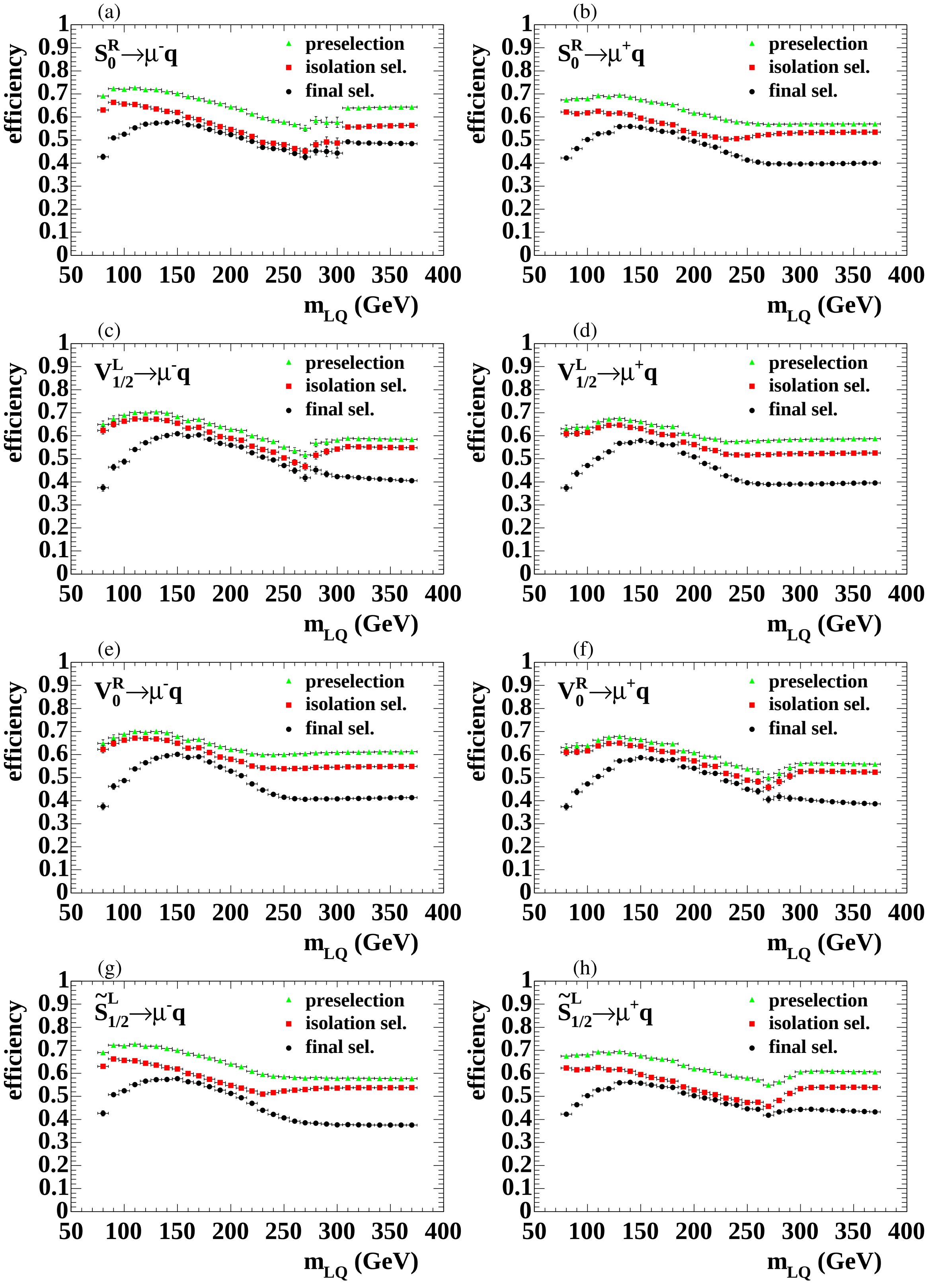

FIGURE 5.5: Muon selection efficiencies in the e^-p data set (left) and in the e^+p data set (right) for different types of leptoquarks. The efficiency is studied for various values of the coupling. Here, the efficiency for a coupling $\lambda_{\mu q} = 0.3$ is shown.

and is noticeable independently of the leptoquark type. This is a compromise for the large background at low values of m_{LQ}. In view of the existing limits on LFV leptoquarks [73, 74] the search is optimised for leptoquark masses above $150\,\mathrm{GeV}$.

It is also an interesting feature that the isolation criteria reduce the efficiency for resonant scalar leptoquarks more than for resonant vector leptoquarks. Vice versa, vector leptoquarks are more affected for u-channel exchange and s-channel production with valence quarks. This can be understood from the difference in the event topology between scalar and vector leptoquarks. For a cross section with $d\sigma/dy \propto (1-y)^2$ (see Sec. 2.4) the decay products have low polar angles whereas a flat y-distribution leads to an isotropic decay in the leptoquark rest frame. The strongest isolation criterion is the distance to central inner vertex-fitted tracks. As forward tracks are not taken into account here, the efficiency in the forward region is less affected.

It should be noted that the effect of the cut $p_{T,\mathrm{calo}} > 25\,\mathrm{GeV}$ on the efficiency for leptoquark masses above $\sqrt{s}$ depends on the leptoquark type and the sensitivity to a u-quark or d-quark. The parton density function (PDF), $xq(x,Q^2)$, for u-quarks tends to larger values of x than for the PDF for d-quarks. If now a leptoquark couples to a u-quark like S_0^R does, the $p_{T,\mathrm{calo}}$ criterion does not reduce the high-mass efficiency as much as in case of leptoquarks coupling to a d-quark only, e.g. $V_{1/2}^L$.

The transition region of m_{LQ} near $\sqrt{s}$ shows large steps in the efficiency of selecting the electron fusion with a valence quark. This reflects the steep fall of the proton PDF in convolution with a narrow resonance peak at very high values of x. As the proton PDF drops significantly less steeply for sea-quarks at high values of x, Fig. 5.5b,d,e and g show a smooth transition from resonant production to virtual exchange.

Chapter 6

Selection of tau-quark pairs

The selection of tau-quark pairs originating from the decay of leptoquarks is presented in this chapter. The efficient identification of tau leptons is very challenging because tau leptons decay before detection in various ways. The selection is divided into three exclusive subselections of electronically, muonically and hadronically decaying taus. The SM background is studied in each decay channel and the selection efficiencies are discussed with the goal of maximal SM background suppression.

6.1 Tau identification

The identification of tau leptons is substantially different from that of electrons or muons. The tau lepton is the heaviest lepton with a mass of $m_\tau = 1776.99^{+0.29}_{-0.26}\,\mathrm{MeV}$ [2]. Its very short lifetime of $\tau_\tau \approx 290\,\mathrm{fs}$ [2] leads to a short average decay length $\langle L \rangle$. The tau lifetime and the average decay length are related through the following expression:

$$\langle L \rangle = \tau_\tau \beta\gamma c, \text{ with } \beta = \frac{|\vec{p}_\tau|}{E_\tau}\ , \quad \gamma = \frac{E_\tau}{m_\tau}\ . \tag{6.1}$$

Therefore, a tau lepton as a leptoquark decay product with a momentum of $10\,\mathrm{GeV}$ decays at a distance of approximately $0.5\,\mathrm{mm}$ from the primary event vertex. This means that only decay products of the tau reach active detector components.

Nevertheless, the feasibility of using this lifetime information by searching for secondary vertices to identify tau leptons has been studied in [75] for the CDF experiment. A separation power of $S = \epsilon_\tau/(1-\epsilon_{vtx}) = 2-4$ between particles from tau decays and those produced at the primary vertex could be achieved. Given the significantly lower track parameter resolution at the H1 experiment and the relatively low transverse momenta of the expected SM tau leptons at HERA, methods based on lifetime information are not further investigated here.

The opening angle α of decay particles from a tau lepton with a momentum of $\mathcal{O}(10\,\mathrm{GeV})$ is relatively small, compared to those from heavier B-mesons for example, and due to the

tau decay mode	branching fraction
electronic decays	
$\tau^- \longrightarrow e^- \bar{\nu}_e \nu_\tau$	17.8%
muonic decays	
$\tau^- \longrightarrow \mu^- \bar{\nu}_\mu \nu_\tau$	17.4%
hadronic decays	
”one-prong”	
$\tau^- \longrightarrow \pi^- \nu_\tau$	11.1%
$\tau^- \longrightarrow \pi^- \pi^0 \nu_\tau$	25.4%
$\tau^- \longrightarrow \pi^- \pi^0 \pi^0 \nu_\tau$	9.2%
“three-prong”	
$\tau^- \longrightarrow \pi^- \pi^- \pi^+ \nu_\tau$	9.5%
$\tau^- \longrightarrow \pi^- \pi^- \pi^+ \pi^0 \nu_\tau$	4.4%
sum hadr.	59.6%
other	5.2%

TABLE 6.1: Principal decay modes of the tau lepton with branching fractions [2].

Lorentz boost it becomes:

$$\cos\alpha = \frac{p_\tau^2 \sin^2\theta^* - m_\tau^2}{p_\tau^2 \sin^2\theta^* + m_\tau^2} , \tag{6.2}$$

where θ^* denotes the decay angle in the tau rest frame.

Fig. 6.1 displays graphically the dependence of the opening angle α on θ^* for different values of p_τ. Assuming that θ^* can be arbitrarily chosen, one can see that for $p_\tau > 10\,\mathrm{GeV}$ the majority of tau decays have an opening angle α of less than 30°. The small opening angle of the decay products hampers the usage of identification techniques like the *impact parameter method* or the $p_{T,\mathrm{rel}}$-*method* which are for example used at the H1 experiment to tag D- or B-mesons [76, 77].

However, the collimated decay products with a characteristic tau signature can be searched for in a narrow $\eta\phi$-cone. In Tab. 6.1 one can see the principle decay modes of the tau lepton with branching fractions. For the identification of electronically decaying tau leptons the neutrinos are expected to be boosted along the electron direction. This characteristic $p_{T,\mathrm{miss}}$ signature is exploited for the electronic tau decay channel as explained in Sec. 6.2. The same argument applies for muonic tau decays, but the limited statistics after the final muon selection allows to interpret the muon search results directly for muonic tau decays. For hadronic tau decays an algorithm exploiting typical track multiplicities in a tau cone was developed in [78, 79] and is applied in this analysis. The main tau decays in Tab. 6.1 can be grouped into *one-prong* and *three-prong* modes. Hence, a charged track multiplicity of 1 or 3 is searched

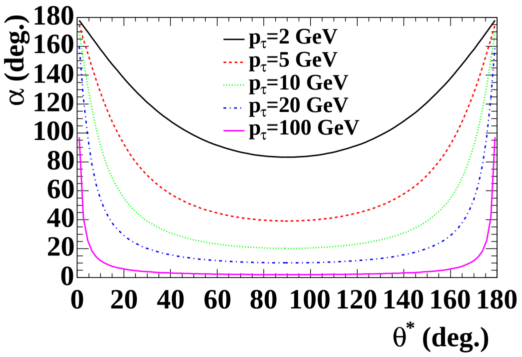

FIGURE 6.1: Opening angle α of tau decay products as a function of the decay angle in the tau rest frame, θ^*, for different values of tau momenta p_τ.

for in a cone of variable size:

$$\alpha_{\text{cone}} = \min\left(\arccos\left(\frac{p_\tau^2 - m_\tau^2}{p_\tau^2 + m_\tau^2}\right), 30^\circ\right) , \tag{6.3}$$

where $2\alpha_{\text{cone}}$ corresponds to a maximum opening angle α. It should be noted that there is, depending on the tau momentum, an inevitable loss of tau decay particles outside a well defined cone (see Fig. 6.1) and that the exact reconstruction of p_τ and θ^* is not feasible due to the escaping neutrinos involved.

It was shown in [78] that the unknown tau momentum p_τ can be approximated universely with $1.5 p_{\tau-\text{jet}}$. Here, a tau-jet is a reconstructed jet serving as a tau candidate. The factor 1.5 accounts for the average undetected neutrino momentum. For the tau cone then follows

$$\alpha_{\text{cone}} = \min\left(\arccos\left(\frac{1.5 p_{\tau-\text{jet}}^2 - m_\tau^2}{1.5 p_{\tau-\text{jet}}^2 + m_\tau^2}\right), 30^\circ\right) + 7.5^\circ , \tag{6.4}$$

where the additional 7.5° account for effects of electromagnetic showers.

For the determination of the track multiplicity, only jets with a sum of track momenta above $2\,\text{GeV}$ are considered. In a tau cone of size α_{cone} around a tau-jet all vertex-fitted central and forward tracks fulfilling so-called *Lee West* quality criteria (listed in Tab. B.1) and with a minimal transverse momentum, i.e. $p_T > 150\,\text{MeV}$, are counted. Tracks which point to secondary vertices or start behind inactive detector material are interpreted as being due to photon conversions and subtracted. Moreover, the fiducial cuts around the calorimeter z-cracks for the electron identification (see Sec. 4.3.1) are also applied to the charged tracks from hadronic particles.

Tau candidates (tau-jets) are thus those jets with exactly one or three tracks in the tau cone and no other track in an isolation cone of fixed size 1.0 in $\eta\phi$. With each tau candidate detailed calorimeter and tracking information is stored to make use of characteristic shower shapes separating tau-jets from quark- or gluon-induced jets (see Sec. 6.4.2).

Electronic tau decay channel preselection							
coll.	data	NC DIS	m_{LQ}	S_0^R	$V_{1/2}^L$	V_0^R	$\tilde{S}_{1/2}^L$
e^-p	1869	1810.24 ± 4.14	$150\,\mathrm{GeV}$	87%	73%	73%	85%
			$500\,\mathrm{GeV}$	73%	53%	62%	50%
e^+p	8201	8026.10 ± 16.50	$150\,\mathrm{GeV}$	84%	70%	70%	82%
			$500\,\mathrm{GeV}$	56%	62%	53%	67%

TABLE 6.2: Preselection results and efficiencies for the electronic tau decay channel. Here, the error on the NC DIS background expectation contains the statistical error only. At the preselection level the contribution of other SM background sources is negligible compared to the NC DIS background.

6.2 Electronic tau decay channel

Apart from the neutrinos leading to missing energy, the event topology of LFV processes with a tau-quark pair and a subsequent electronic tau decay is the same as that of NC DIS events. The NC DIS control sample discussed in Sec. 4.7 is used here as a preselection sample. The control distributions in Fig. 4.10 show a $200\,\mathrm{GeV}$ $\tilde{S}_{1/2}^L$ leading to a $\tau + q$ final state with a subsequent electronic tau decay as a LFV signal.

As can be read from Tab. 6.2, the preselection yields 1869 e^-p data events with a NC DIS background expectation from NC DIS of $1810.24 \pm 4.14\,(\mathrm{stat.})$. The e^+p data set preselection results in 8201 data events where $8026.10 \pm 16.50\,(\mathrm{stat.})$ are expected from the NC DIS. At the preselection level the contribution of other SM background sources is negligible compared to the NC DIS background. Tab. 6.2 also shows the selection efficiencies for the leptoquarks S_0^R, $V_{1/2}^L$, V_0^R and $S_{1/2}^L$ of mass $150\,\mathrm{GeV}$ and $500\,\mathrm{GeV}$ decaying to a tau-quark pair and a following electronic tau decay.

As the final selection step, a set of cuts mostly exploiting the characteristic $p_{T,\mathrm{miss}}$ signature (see Fig. 4.10h) in the signal events is applied:

- $p_{T,jet1} > 25\,\mathrm{GeV}$
- $p_{T,\mathrm{miss}} > 20\,\mathrm{GeV}$
- $\Delta\phi_{e-\mathrm{miss}} < 20^\circ$
- $p_{T,e}/p_{T,X} < 0.8$
- if a *Lee West* track is associated to the electron: $p_{T,e-\mathrm{clu}}/p_{T,e-\mathrm{trk}} > 0.7$

The requirement $p_{T,jet1} > 25\,\mathrm{GeV}$ is motivated by the distribution in Fig. 6.2a. Low-p_T background is reduced while the expected signal is kept. It is necessary to demand a clear missing momentum with $p_{T,\mathrm{miss}} > 20\,\mathrm{GeV}$ to make use of the characteristic neutrinos in the

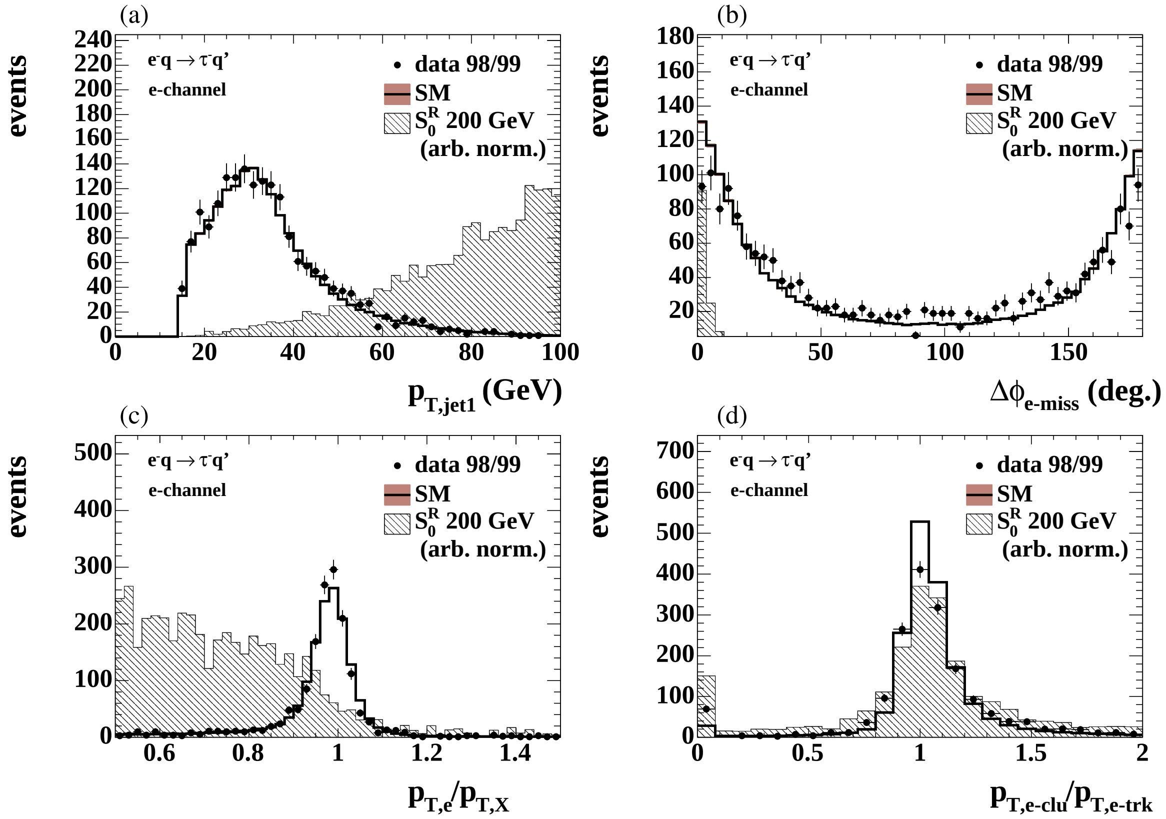

FIGURE 6.2: Distributions before the final selection step in the electronic tau decay channel.

signal event. From the high electron transverse momentum (see Fig. 4.10a) in the signal process one can deduce with Eq. (6.2) that the neutrinos in the event are most likely boosted along the electron direction. This leads to the distribution in Fig. 6.2b which displays the distance in ϕ between the electron and the missing transverse momentum, $\Delta\phi_{e-\text{miss}}$, if $p_{T,\text{miss}} > 5\,\text{GeV}$. The signal is accumulated at very low values of $\Delta\phi_{e-\text{miss}}$ and the very effective requirement $\Delta\phi_{e-\text{miss}} < 20°$ is justified. The imbalance in p_T is furthermore utilised by the criterion $p_{T,e}/p_{T,X} < 0.8$, where the transverse momentum of the hadronic final state $p_{T,X}$ is calculated with the double-angle method (see Fig. 6.2c). The last requirement of $p_{T,e-\text{clu}}/p_{T,e-\text{trk}} > 0.7$ for events with a *Lee West* track associated to the electron is not so obvious from Fig. 6.2d. Nevertheless, remaining background from mismeasurements of the electron energy can be drastically reduced if the tracking information is available. As the previous selection steps enrich the background sample with electron mismeasurements the last selection criterion is needed. The first bin in Fig. 6.2d gives an estimate on the fraction of events with no electron track.

The final selection results in the electronic tau decay channel are summarised in Tab. 6.3. One data event (run 240456, event 62835) in the e^-p data sample passes all criteria with

Electronic tau decay channel final selection								
coll.	data	SM		m_{LQ}	S_0^R	$V_{1/2}^L$	V_0^R	$\tilde{S}_{1/2}^L$
e^-p	1	0.36 ± 0.20	NC: 0.25 ± 0.19 CC: 0.07 ± 0.02 γP: 0.03 ± 0.02	150 GeV 500 GeV	51% 44%	45% 26%	45% 28%	51% 23%
e^+p	0	1.40 ± 0.56	NC: 1.12 ± 0.54 CC: 0.09 ± 0.03 γP: 0.12 ± 0.11	150 GeV 500 GeV	47% 28%	42% 28%	42% 26%	48% 34%

TABLE 6.3: Final selection results and efficiencies for the electronic tau decay channel. The statistical error and the systematic error are added in quadrature.

$0.36 \pm 0.04\,(\mathrm{stat.}) \pm 0.19(\mathrm{sys.})$ expected from SM. The e^+p data sample contains no candidate event with a SM background of $1.40 \pm 0.20\,(\mathrm{stat.}) \pm 0.52(\mathrm{sys.})$. The final mass spectrum of the e^-p data sample with the candidate event is displayed in Fig. 6.3. An event display of the candidate event is shown in Fig. 6.4. The kinematics of the event agree with a LFV signal event. The missing transverse momentum in the event is determined to be 71 GeV. The distance in ϕ between the electron and the $P_{T,\mathrm{miss}}$ is below 2°. A leptoquark mass of 312 GeV can be reconstructed using the double-angle method.

Due to the fact that there is no reconstructed track associated to the electromagnetic cluster, an uncertainty on the electron measurement remains. As can be seen in the event display in Fig. 6.4 there are almost no hits in the central or forward tracking chambers that can be associated to the electron. Only a short reconstructed forward track segment in the second FTD supermodule might be due to the electron. Consistent with about 20% of the selected background attributed to CC DIS events in e^-p collisions, the event may also be identified as a radiative CC DIS event, where the electromagnetic cluster is interpreted as a photon radiated from the electron- or quark-line. The signal-typical *back-to-back* topology would be coincidence under this assumption. Nonetheless, the event remains a candidate event for LFV, because of the low efficiency of reconstructing forward tracks (see. Fig. 4.4).

In analogy to the search for muon-quark pairs the lack of a significant deviation from the SM suggests a detailed study of the signal selection efficiencies. Tab. 6.3 and Fig. 6.5 illustrate the efficiencies for some leptoquark types. Whereas in Tab. 6.3 the selection efficiency refers to electronic tau decays only, Fig. 6.5 shows the efficiency normalised to all tau decays limited by the branching fraction $BR(\tau^- \to e^-\bar{\nu}_e\nu_\tau) = 17.8\%$.

The features of the selection efficiencies are similar to those in the search for muon-quark pairs. The PDF uncertainties are highest in the transition region for a leptoquark coupling to a valence quark. Of the chosen example leptoquarks, S_0^R is only one that couples to a u-quark leading to a significantly higher selection efficiency in the high-mass region with $m_{\mathrm{LQ}} > \sqrt{s}$.

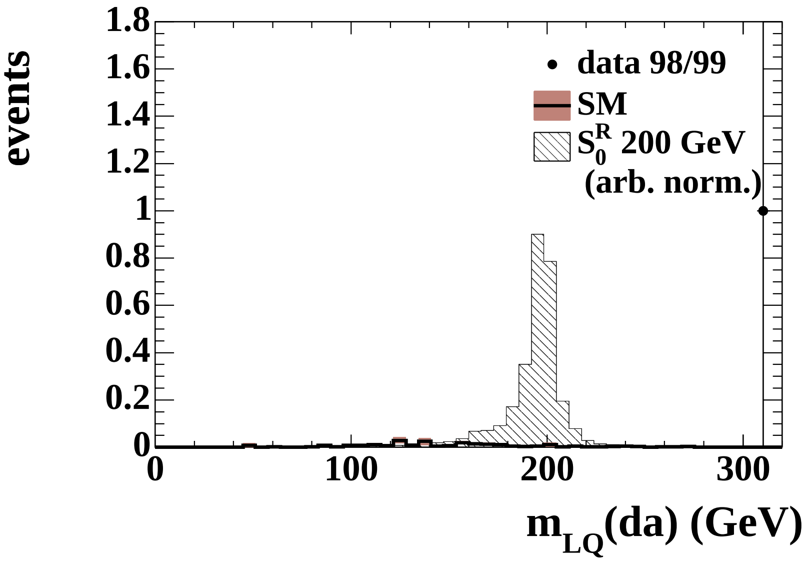

FIGURE 6.3: Leptoquark mass spectrum after final selection in the electronic tau decay channel.

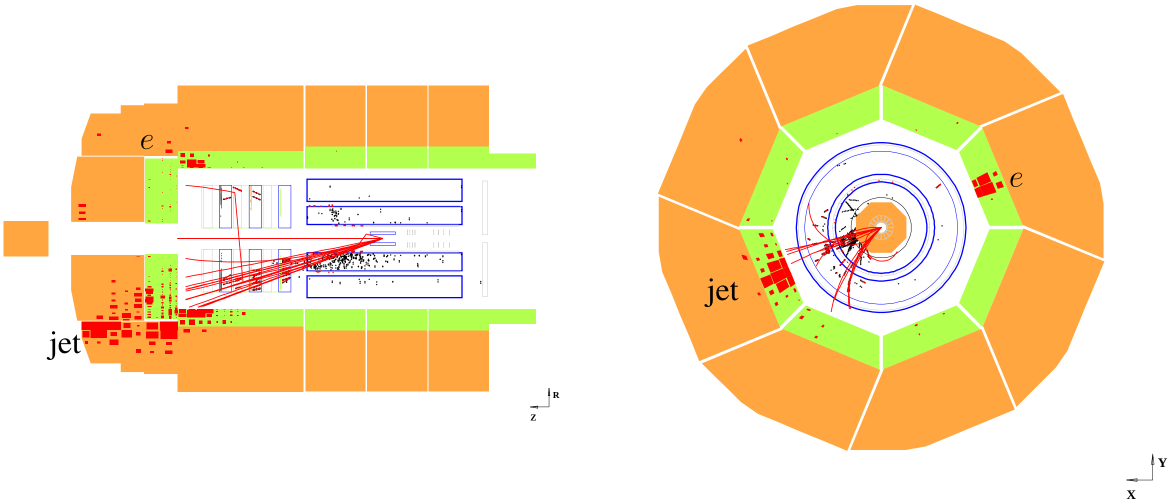

FIGURE 6.4: Event display of the e^-p data event passing all selection criteria in the electronic tau decay channel (run 240456, event 62835). The $r\phi$ perspective shows only the central calorimeter barrels to get a detailed view on the tracking system. Hits in the tracking system are displayed to find traces of the unidentified electron track.

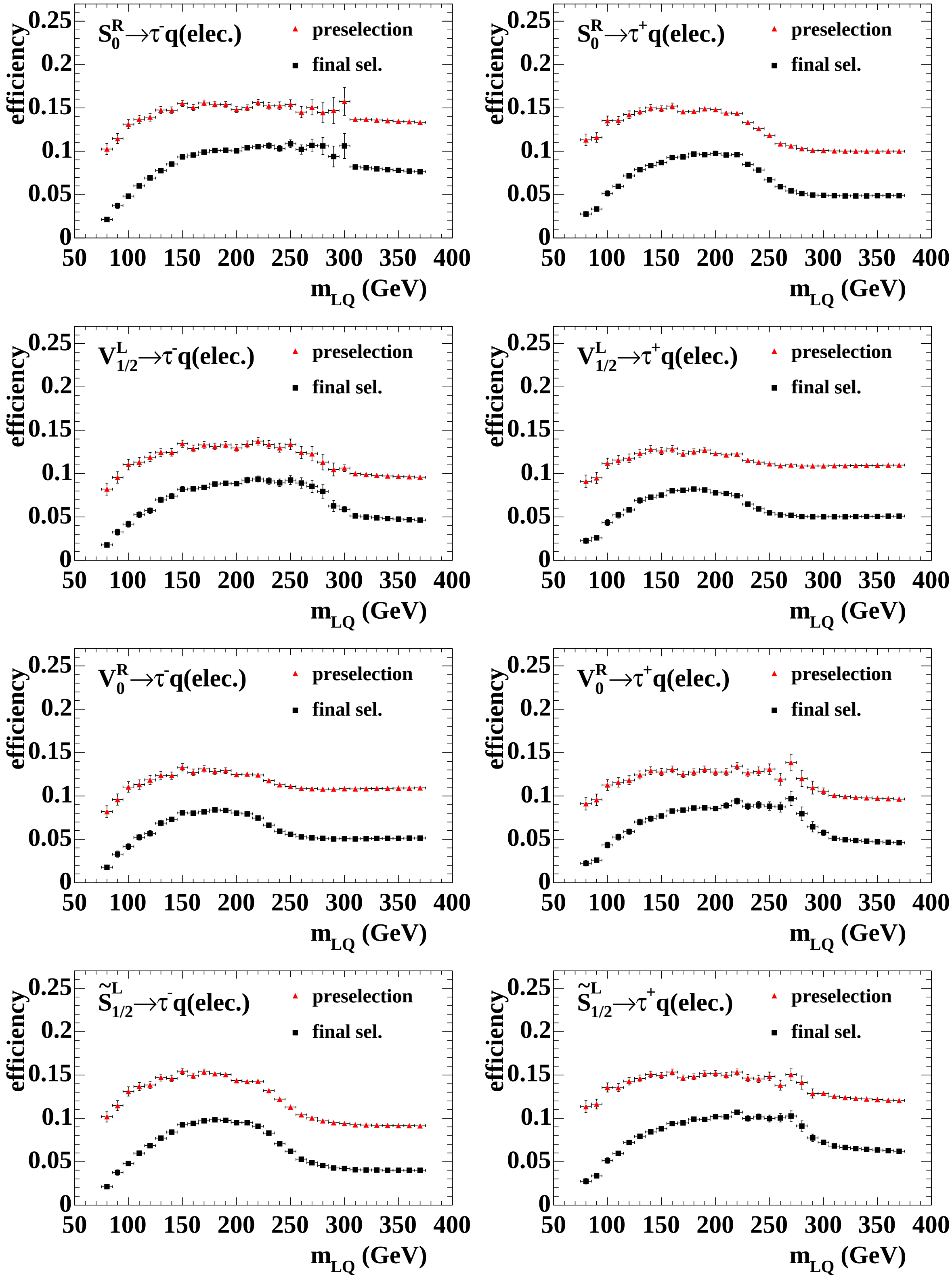

FIGURE 6.5: Selection efficiencies in the electronic tau decay channel in the e^-p data set (left) and in the e^+p data set (right) for different types of leptoquarks. It should be noted that this is the efficiency normalised to all tau decays limited by the branching fraction $BR(\tau^- \to e^-\bar{\nu}_e\nu_\tau) = 17.8\%$. The efficiency is studied for various values of the coupling. Here, the efficiency for a coupling $\lambda_{\tau q} = 0.3$ is shown.

6.3 Muonic tau decay channel

The muonic tau decay channel is with regard to the event topology very similar to the LFV decay to a muon-quark pair, albeit with somewhat smaller muon transverse momenta. Therefore, the results of the search for muon-quark pairs are applied to this channel as well. The same argumentation as in the previous Sec. 6.2 making use of the typical neutrino signature could in principle be applied here. But for two reasons no further selection criteria are demanded:

1. The background statistics after the final selection in the search for muon-quark pairs are already low.

2. The determination of the missing transverse momentum in the event would depend on the energy determination in the muon system. The accuracy of the energy measurement in the muon system showed not to be sufficient enough for this purpose.

Hence, the results in Tab. 5.2 apply for the interpretation of the search results for LFV events with a tau-quark pair and a muonic tau decay. To account for possible effects on the efficiency due to different muon kinematics, the selection efficiency was studied in detail with a LFV signal sample with a $\tau + q$ final state and a subsequent muonic tau decay. Fig. 6.6 shows some efficiencies for the individual selection steps. The e^+p data is used to display the efficiency of the search for $F = 0$ leptoquarks and e^-p data was chosen for $F = 2$ leptoquarks. Again, the branching fraction $BR(\tau^- \rightarrow \mu^- \bar{\nu}_\mu \nu_\tau) = 17.4\%$ is limiting the efficiency which is normalised to all tau decays. Comparison of the efficiencies with those in the muon channel (see Fig. 5.5) shows that the branching fraction of muonic tau decays is the cause of the principle differences. Effects of the potentially lower muon transverse momenta on the efficiency are minimal.

6.4 Hadronic tau decay channel

Hadronic decays are the dominant tau decay channel with a branching fraction of about 65%. The hadronic decay products from a high-p_T tau are expected to build a collimated jet. Following the tau identification procedure described in Sec. 6.1, isolated low multiplicity jets are flagged as tau-jets in a dijet preselection sample. Then, a multivariate analysis of the calorimetric jet shapes and tracking information is used to separate collimated tau-jets from broad quark- or gluon-induced jets. Finally, some missing momentum distributions are confined to the regions where the leptoquark signal is dominant.

6.4.1 Dijet preselection with a tau candidate

The search for LFV events with a tau-quark pair and a hadronic tau decay starts with a dijet preselection containing at least one tau-jet (see Sec. 6.1). The following preselection criteria apply:

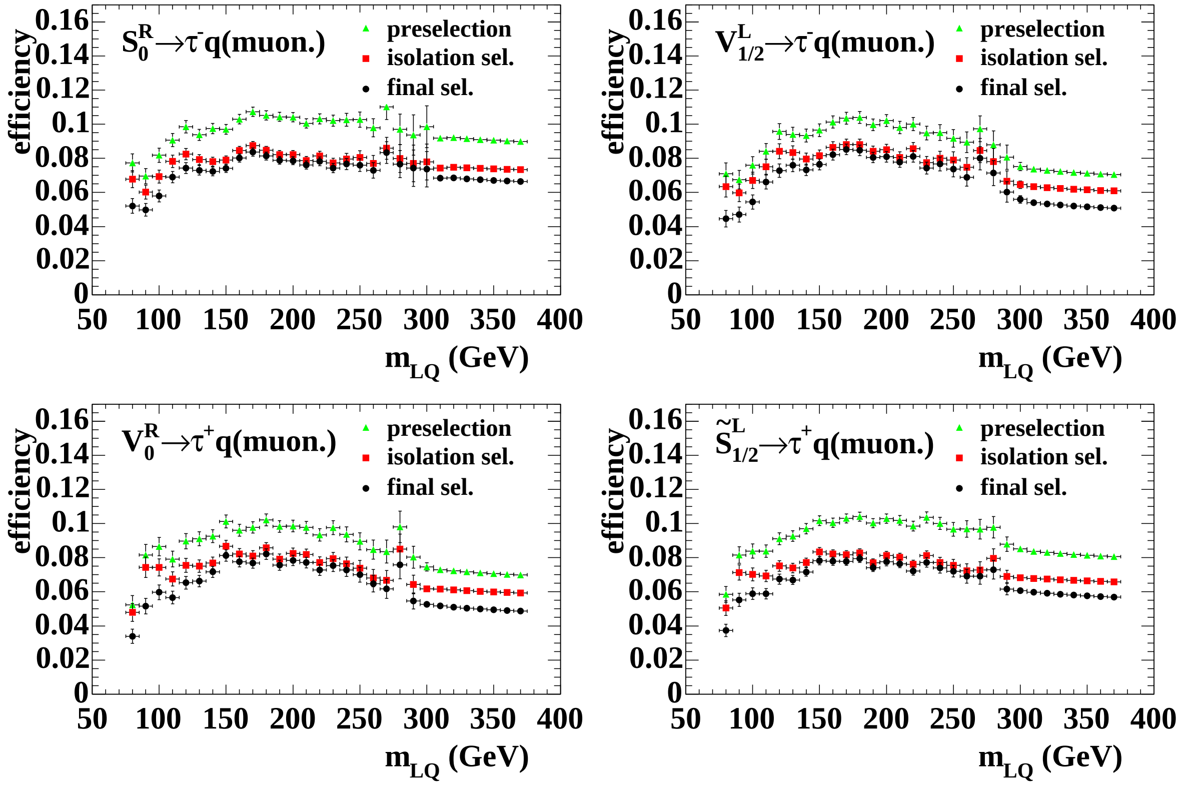

FIGURE 6.6: Selection efficiencies in the muonic tau decay channel for different types of leptoquarks. The data sample for $F = 2$ leptoquarks is chosen to be $e^- p$ and $e^+ p$ data is used to display the efficiency of the search for $F = 0$ leptoquarks. The branching fraction $BR(\tau^- \to \mu^- \bar{\nu}_\mu \nu_\tau) = 17.4\%$ is limiting the efficiency which is normalised to all tau decays.

- At least two jets with a transverse momentum $p_{T,\text{jet1}} > 20\,\text{GeV}$ and $p_{T,\text{jet2}} > 15\,\text{GeV}$ reconstructed in the polar angle range $7^\circ < \theta_{\text{jets}} < 145^\circ$.
- Veto events with a reconstructed isolated electron[1] or muon[2].
- At least one tau-jet with $\theta_{\tau-\text{jet}} > 20^\circ$.

The general data quality criteria described in Sec. 4.1 are demanded and the subtriggers s66, s67, s71, s75 and s77 are employed to trigger the events.

---

[1] Isolated electron means here that the sum of all energy deposits in an $\eta\phi$-cone of size 0.5 around the electron, E_{cone}, is restricted to $E_{\text{cone}}/E_e < 1.03$

[2] A muon is flagged as isolated if there are not more than $5\,\text{GeV}$ of energy deposits reconstructed inside a cylinder of radius $25\,\text{cm}$ around the muon direction and if there are no vertex-fitted central tracks found in an $\eta\phi$-cone of size 0.5 around the muon track.

Hadronic tau decay channel preselection		
set	98/99 e^-p	99/00 e^+p
NC	115.33 ± 4.01	623.48 ± 13.26
CC	0.67 ± 0.04	2.31 ± 0.13
γP	368.28 ± 5.67	1837.39 ± 31.95
ee,$\mu\mu$,$\tau\tau$-Prod.	0.45 ± 0.04	1.46 ± 0.12
W-Prod.	1.16 ± 0.01	3.82 ± 0.08
SM tot.	485.89 ± 6.94	2471.44 ± 29.53
data	493	2548

TABLE 6.4: Preselection results of the hadronic tau decay channel. Here, the error on the SM background expectation contains the statistical error only.

As the tau-neutrino is expected to be boosted along the hadronic tau decay products, the highest-p_T jet (jet1) is most likely to be the quark-jet and the second highest-p_T jet (jet2) is probably the tau-jet. However, the tau-jet flag may be set in very rare events for more than one jet, in which cases the highest-p_T tau-jet is chosen to be the analysed tau-jet. The minimal values of jet transverse momenta are motivated by the large expected leptoquark mass of $\mathcal{O}(100\,\mathrm{GeV})$ inducing large momenta of the decay products. Furthermore, the trigger efficiency (see Fig. 4.3) is near to 100% and well described by the SM MC simulation for events with $p_{T,\mathrm{jet1}} > 20\,\mathrm{GeV}$. The polar angle range demanded for both jets reflects the LAr calorimeter acceptance. For the later combination of the hadronic search channel with the leptonic channels, the exclusivity between the channels must be guaranteed by the veto on isolated electrons or muons. The identification of tau-jets was found to be well described if a minimal polar angle $\theta_{\tau-\mathrm{jet}} > 20^\circ$ is demanded.

Fig.6.7 demonstrates the reconstructed transverse momenta and polar angles of the two highest-p_T jets in both data samples. The data is very well described in both samples by the SM MC simulation, which is made up of mainly photoproduction ($\sim 74\%$) and NC DIS ($\sim 24\%$). Tab. 6.4 contains the results of the preselection in numbers.

The features of the kinematic variables Q^2_{jj} and y_{jj} are displayed in Fig.6.8a,b. The subscript jj points to the fact that the variables are calculated with the double-angle method using the directions of the two jets. The direction of jet2 is taken to be the direction of the scattered lepton and the jet1 vector replaces the vector of the hadronic final state in Eqs. (4.7),(4.8). By this the leptoquark mass resolution (see Fig.6.8e) is significantly improved. Events with three jets or more and a third jet significantly contributing with respect to p_T are very rare in the sample. The compromised mass resolution for these few events can be tolerated.

The variable $E - p_z$ (Fig.6.8d) is the only variable showing some discrepancies between data and MC simulation. For low values of $E - p_z$ the SM background is dominated by

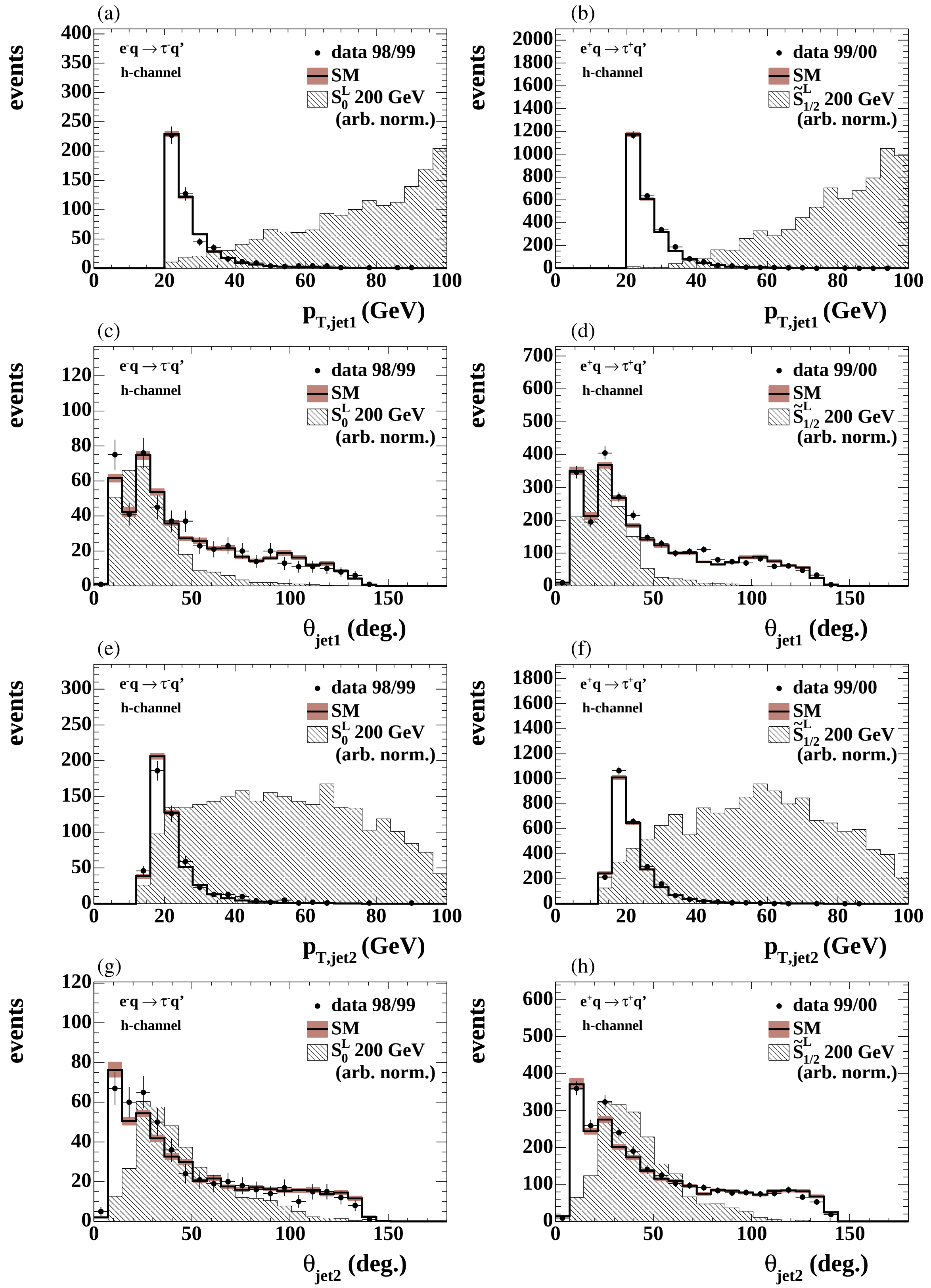

FIGURE 6.7: Dijet preselection in the hadronic tau decay channel: Reconstructed transverse momenta and polar angles of the two highest-p_T jets in both data samples e^-p (left) and e^+p (right).

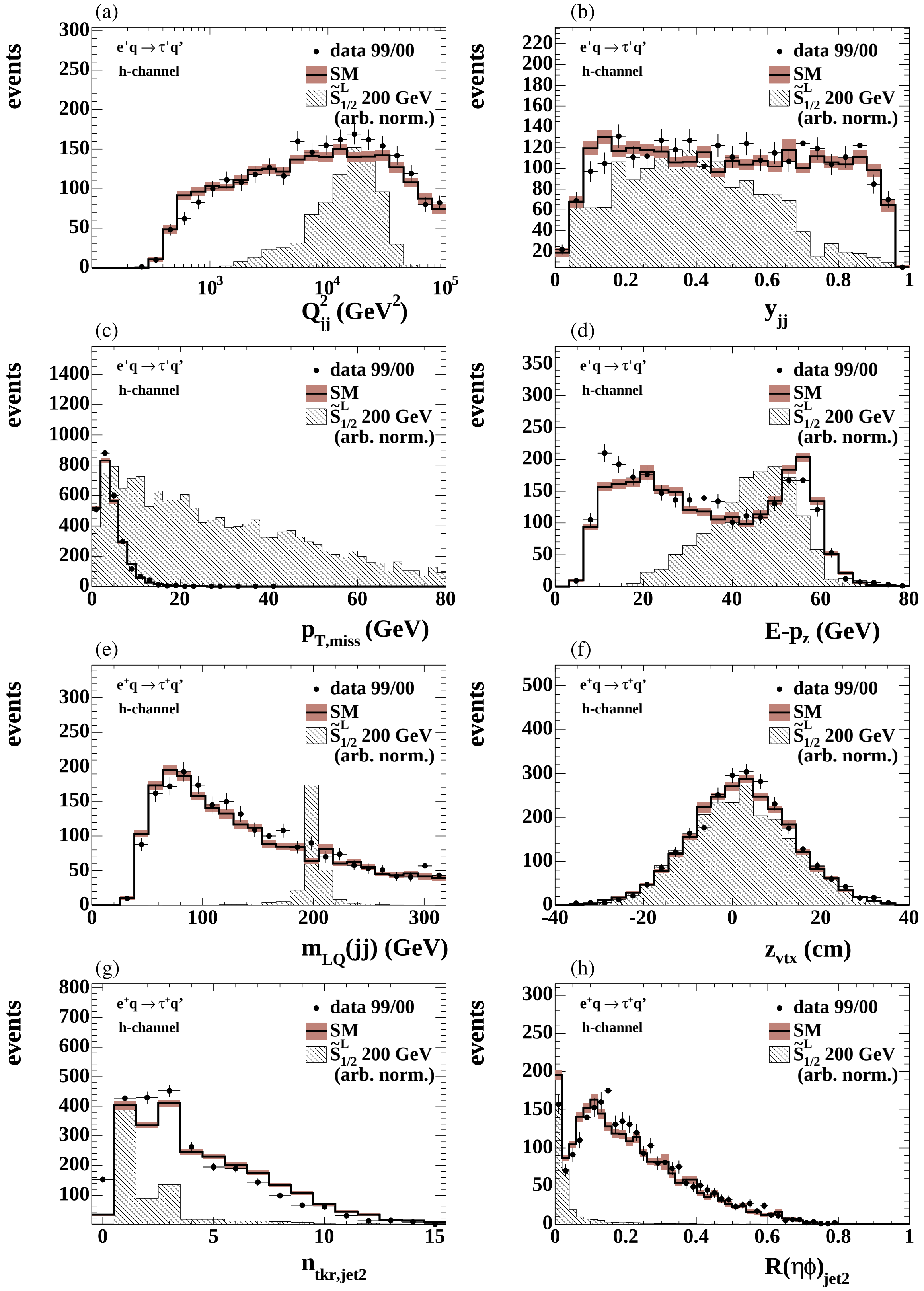

FIGURE 6.8: Dijet preselection in the hadronic tau decay channel: Selected reconstructed kinematic variables and observables in the e^+p data sample. The description of the data by the SM MC simulation is similar for the e^-p data set. The notation jj means that the value is derived with the double-angle method using the directions of the two jets.

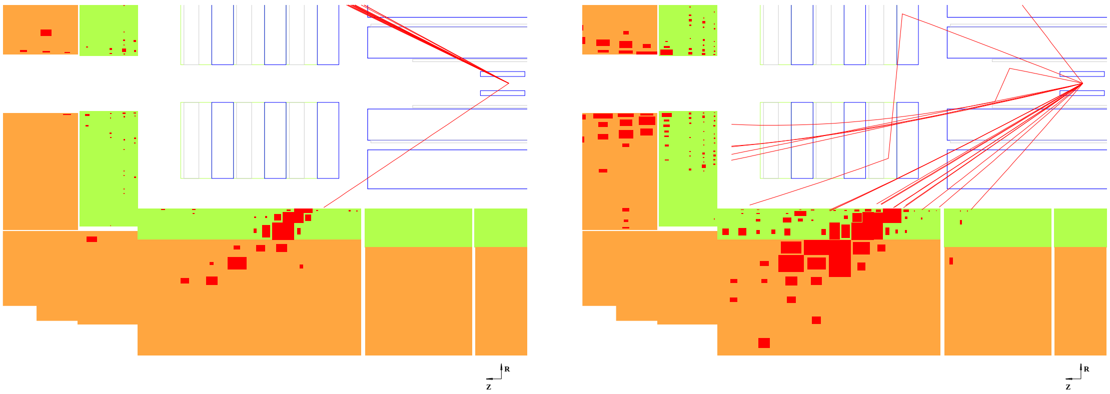

FIGURE 6.9: Simulated detector response of a typical tau-jet (left) and a quark- or gluon-induced jet (right).

photoproduction events. However, the applied theoretical error of 30% on the photoproduction sample, not shown in Fig.6.8, covers these discrepancies. Fig.6.8g,h support the supposition that the tau-jet is in most cases identical to jet2. The track multiplicity $n_{trk,\mathrm{jet2}}$ for the signal reflect the one- and three prong tau decay topology. An estimate on the radial size of jet2 is given by $R(\eta\phi)_{\mathrm{jet2}}$ which is defined as the energy-weighted mean distance in $\eta\phi$ of all particles in jet2 with respect to the jet2 axis. The narrow jet shape of the signal in contrast to the SM background is apparent in Fig.6.8h.

Nevertheless, the tau-jet flag is only set for jets with $\theta_{\mathrm{jet}} > 20°$. In events with $\theta_{\mathrm{jet2}} < 20°$ the uncertainty on the p_T-ordering is large and the highest-p_T jet may be flagged as tau-jet. The $p_{T,\mathrm{miss}}$-distribution in Fig.6.8c shows that the signal tends to much larger values than the SM background. However, a harsh cut like $p_{T,\mathrm{miss}} > 20\,\mathrm{GeV}$ would significantly deteriorate the signal selection efficiency.

6.4.2 Multivariate discrimination

The large SM background contribution after the preselection shows that the tau-jet flag based on track isolation and low multiplicity is not sufficient enough to separate tau-jets from quark- or gluon-induced jets (QCD-jets). In the second selection step, the typical calorimetric shower shape and tracking signature is exploited to further identify tau-jets. Fig. 6.9 illustrates the difference between a tau-jet and a QCD-jet on the basis of a partial event display of a simulated detector response. In contrast to the broad QCD-jet, the narrow *pencil-like* shape of the calorimeter deposits from the hadronic tau decay products are apparent. Also three-prong tau decays leave a characteristic narrow signature in the detector that is markedly different from most QCD-jets.

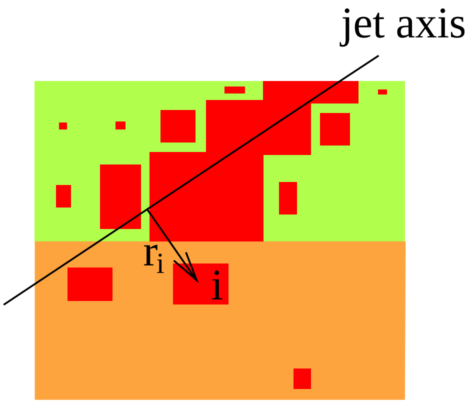

FIGURE 6.10: Schematic sketch of the radial momentum determination.

Estimator variables

The energy-weighted radial moments of the jet are used to quantify the radial extension of the jet with respect to the jet axis. The j^{th} energy-weighted radial algebraic moment is defined as

$$\langle r^j \rangle = \frac{\sum_i E_i r_i^j}{\sum_i E_i} , \tag{6.5}$$

where the sum runs over all calorimeter cells i in the tau cone and r_i represents the radial distance of cell i to the jet axis (see Fig. 6.10). The first two moments are considered for discrimination, where the first moment can be interpreted as the mean distance $\langle r \rangle$ and the square root of the second moment $\langle r^2 \rangle$ is known as the root-mean-square (RMS) of the radial jet expansion. Rather than the RMS the standard deviation $\sigma(r)$ is employed in the following with

$$\sigma(r) = \sqrt{\langle r^2 \rangle - \langle r \rangle^2} . \tag{6.6}$$

Although the first and second radial momenta contain the strongest separation power between tau-jets and QCD-jets, additional observables are used to identify hadronic tau decays:

- Distance in $\eta\phi$ between the direction of the highest-p_T track and the centre of gravity of the calorimetric cluster, i.e.

$$D_{\mathrm{trk-clu}} = \sqrt{(\eta_{\mathrm{trk}} - \eta_{\mathrm{clu}})^2 + (\phi_{\mathrm{trk}} - \phi_{\mathrm{clu}})^2} . \tag{6.7}$$

- Number of tracks including those which point to secondary vertices or start behind inactive detector material, $n_{\mathrm{trk,tau-cone}}$.
- Number of cells above the noise level inside the tau cone, n_{cells}.

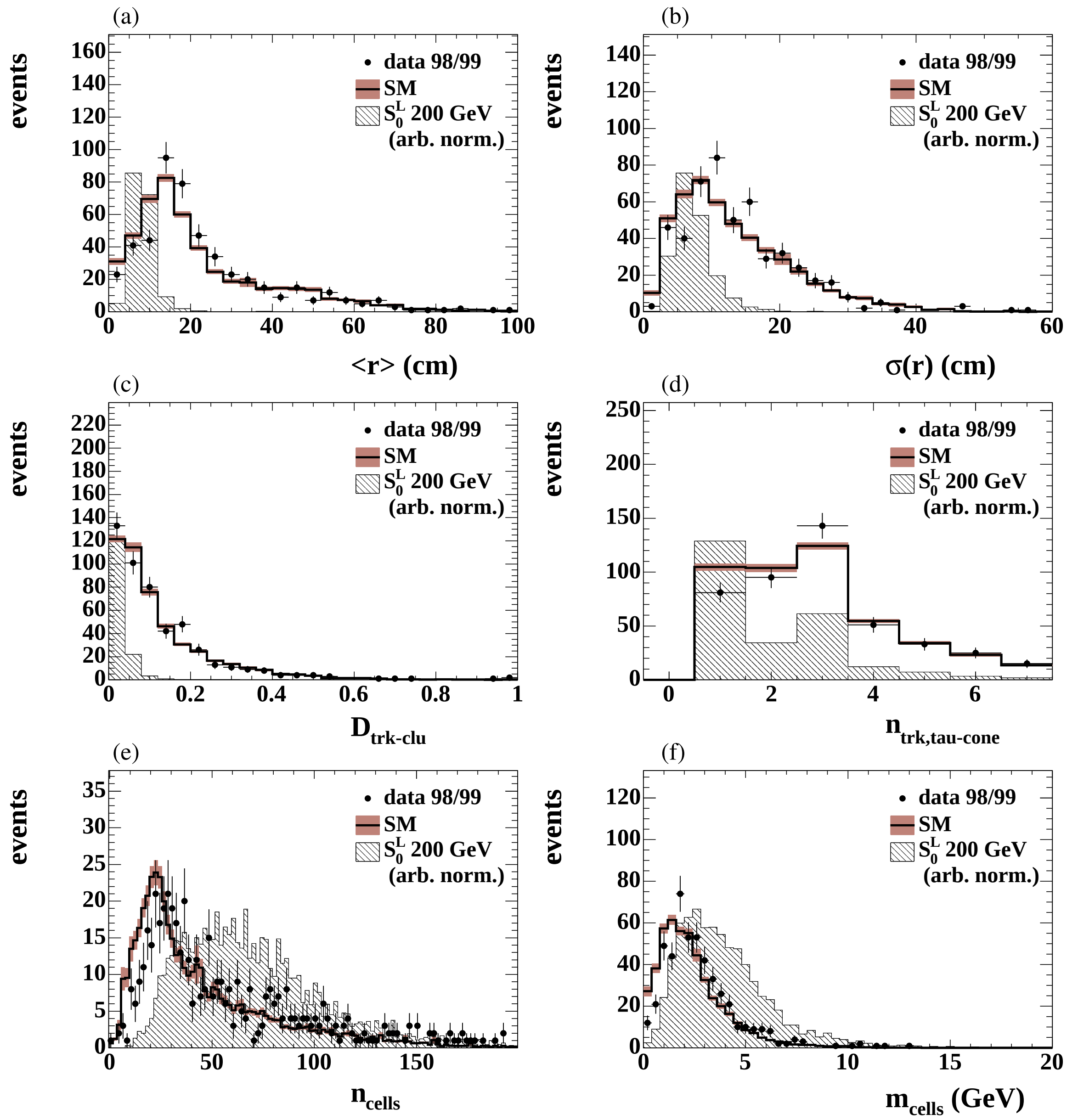

FIGURE 6.11: Estimator variables for the neural network classification of tau-jets in the e^-p sample. The distributions are similar in the e^+p sample.

- The invariant tau-jet mass calculated from the calorimeter cells, i.e.

$$m_{\text{cells}} = \sqrt{\left(\sum_i E_i\right)^2 - \left(\sum_i \vec{p}_i\right)^2} \ , \tag{6.8}$$

  where the momentum vector $\vec{p}_i$ of cell i with energy E_i and position (θ_i,ϕ_i) is defined as $\vec{p}_i \equiv (E_i \sin\theta_i \cos\phi_i \ , \ E_i \sin\theta_i \sin\phi_i \ , \ E_i \cos\theta_i)$.

Neural network separation

Most of the estimator variables are highly correlated which suggests a multivariate analysis approach rather than a cut-based strategy. Previous analyses tackling the problem of tau identification [73, 79] have shown that multivariate analysis techniques are advantageous with respect to discrimination power. However, for comparison of the performance and as a cross-check a cut-based selection and a range search (RS) algorithm [80, 81] are performed in addition to the final applied neural network (NN) classification [82].

A neural network is trained with a total of nine input variables: the six estimators mentioned above and additional three parametrisation variables. Both the energy of the tau-jet determined from tracks, $E_{\tau-\text{jet}}(\text{trk})$, and energy reconstructed from the calorimeter deposits, $E_{\tau-\text{jet}}(\text{clu})$, are used to parametrise the energy dependence of the shower shape. For the neural network to learn the shape dependence on the polar angle due to differences in the calorimeter granularity, the polar angle $\theta_{\tau-\text{jet}}$ is also added as an input variable.

In order to obtain tau-jet identification that is independent of the event kinematics, the feature vector consistent of the nine input variables is weighted according to relative statistics of signal and background in a bin on a two-dimensional grid $(E_{\tau-\text{jet}}(\text{clu}),\theta_{\tau-\text{jet}})$. Details of this procedure can be found in [78]. After this reweighting a high-p_T jet is for example less likely to be identified as a tau-jet because the collimation of particles gets stronger with rising jet energy (see Fig. 6.1).

It is an interesting feature of the jets which are flagged as a tau-jet in the preselected sample that $E_{\tau-\text{jet}}(\text{trk})$ and $E_{\tau-\text{jet}}(\text{clu})$ differ significantly in both SM background (consistent of $\sim 75\%$ γP and $\sim 25\%$ NC DIS, see Tab. 6.4) and LFV signal. For the signal the cluster energy is larger than the energy determined from tracks, because of neutral particles which are produced in many tau decays. The QCD-jets in the SM background incorporate a significant fraction of neutral particles with transverse momenta above $15\,\text{GeV}$.

For the neural network training the background and signal sets are split randomly into a training set with 40% of the events and an analysis sample with 60% of the events. The training set itself is built up of a 60% training sample, a 20% validation sample and a 20% evaluation sample. The complete training set is not used for further analysis. For the topology two hidden layers are chosen with 10 (17) neurons in the first (second) hidden layer (for argumentation see [78]). The output layer consists of one node releasing a discriminator variable $\mathcal{D}_{\text{NN}}$ in the range $0 \leq \mathcal{D}_{\text{NN}} \leq 1$ with value 0 for QCD-jets and value 1 for tau decay products

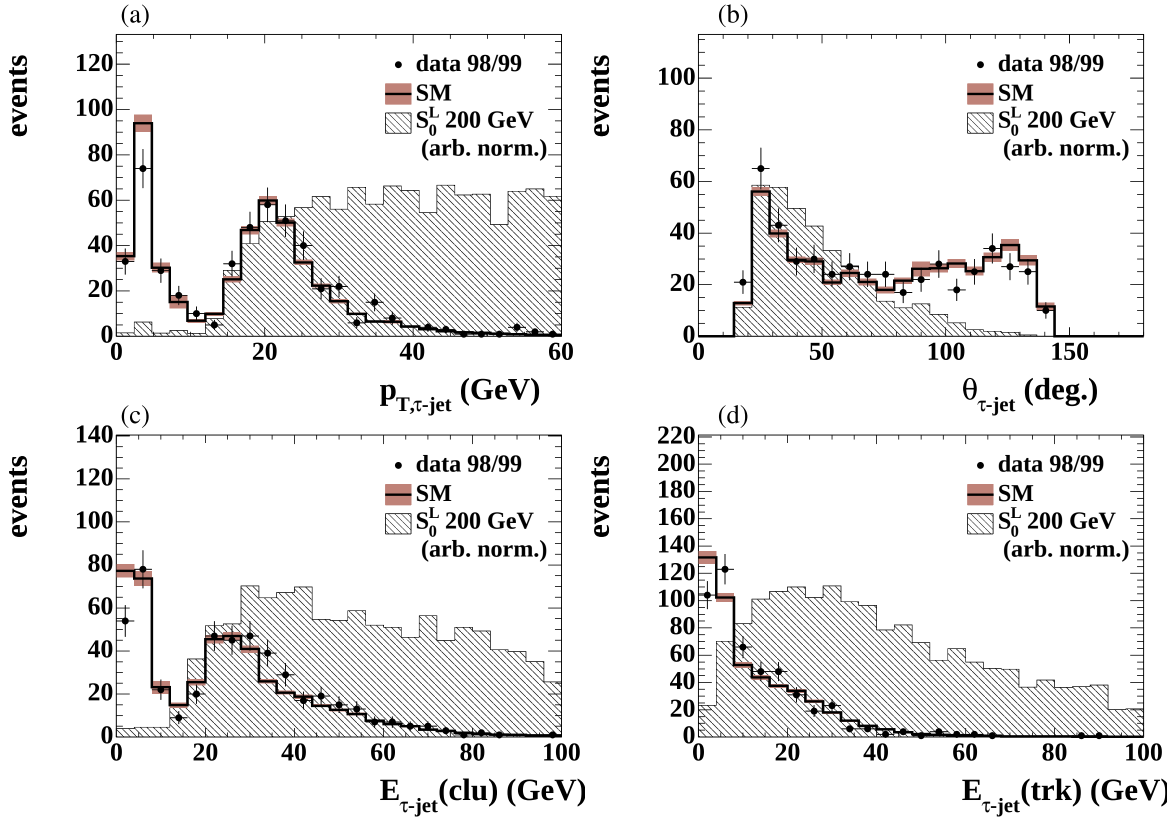

FIGURE 6.12: Parametrisation variables to determine the dependence of the shower shape on the jet energy and jet polar angle. The $p_{T,\tau-\mathrm{jet}}$-distribution in (a) is not used as a parameter.

Fig. 6.13a shows the distribution of the output variable $\mathcal{D}_{\mathrm{NN}}$. The strong separation power between tau-jets and QCD-jets is apparent. The multivariate discrimination is performed with the cut $\mathcal{D}_{\mathrm{NN}} > 0.8$.

As a cross-check the estimator variables are also fed into a range search algorithm [80, 81], the output of which is displayed in Fig. 6.13b. The range search is also capable of separating tau-jets from QCD-jets although the performance here is somewhat weaker compared to the neural network. The performances are quantitatively compared in Fig. 6.14. A variation of a possible cut-value on the discriminator variable yields the displayed lines for the NN and the RS. Since a large background rejection is needed, the NN with a higher signal selection efficiency for a target background rejection of more than 80% performs better than the RS.

In addition, a point for a rudimentary cut-based selection is visible in Fig. 6.14. This cut-based selection is performed in parallel to the selection steps so far and incorporates $p_{T,\mathrm{miss}}$ cuts similar to those which are applied in the final selection step. After the same preselection cuts, jet2 is required to fulfil some tau-jet criteria: $1 \leq n_{\mathrm{trk,jet2}} \leq 3$, $R(\eta\phi)_{\mathrm{jet2}} < 0.12$, $m_{\mathrm{jet2}} < 7\,\mathrm{GeV}$ and no tracks in an outer $\eta\phi$-cone around jet2 with $0.12 < D_{\mathrm{trk-jet2}} < 1.0$. Furthermore, the cuts $p_{T,\mathrm{miss}} > 20\,\mathrm{GeV}$ and $\Delta\phi_{\mathrm{jet2-miss}} < 30^\circ$ are applied. One can see that

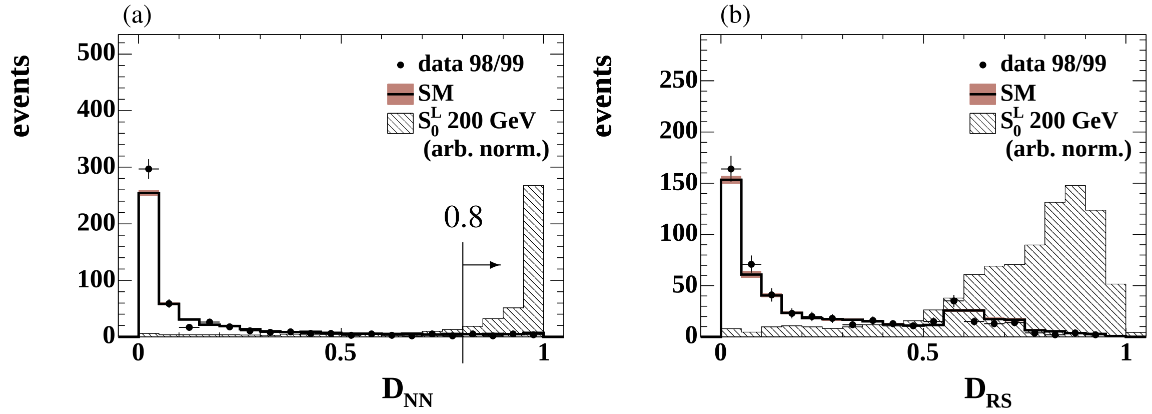

FIGURE 6.13: Discriminator variables $\mathcal{D}_{\mathrm{NN}}$ as neural network output and $\mathcal{D}_{\mathrm{RS}}$ as range search output. A value of zero indicates QCD-jets (here $\sim 75\%$ γP and $\sim$ 25% NC DIS) and a value of one classifies a jet as tau decay products. The multivariate discrimination is performed with the cut $\mathcal{D}_{\mathrm{NN}} > 0.8$. The range search output in (b) serves as a cross-check.

the performance is similar, but still worse than the NN performance. Moreover, the criterion $p_{T,\mathrm{miss}} > 20\,\mathrm{GeV}$ is a harsh cut affecting the selection efficiency of high-mass leptoquarks with large low-mass tales significantly (see Fig. 6.18).

After the cut $\mathcal{D}_{\mathrm{NN}} > 0.8$ is applied, 16 e^-p data events are selected with $22.0 \pm 1.02\,(\mathrm{stat.})$ expected from SM background and 112 e^+p data events pass the selection with a SM expectation of $121.12 \pm 5.25\,(\mathrm{stat.})$ events. Tab. 6.5 summarises the results and gives an estimate for the signal selection efficiencies of some leptoquark types with mass $150\,\mathrm{GeV}$ and $500\,\mathrm{GeV}$ respectively.

Hadronic tau decay channel multivariate selection							
coll.	data	SM MC	m_{LQ}	S_0^R	$V_{1/2}^L$	V_0^R	$\tilde{S}_{1/2}^L$
e^-p	16	22.0 ± 1.02	$150\,\mathrm{GeV}$	38%	42%	42%	38%
			$500\,\mathrm{GeV}$	32%	29%	29%	28%
e^+p	112	121.12 ± 5.25	$150\,\mathrm{GeV}$	35%	37%	37%	35%
			$500\,\mathrm{GeV}$	29%	28%	29%	31%

TABLE 6.5: Multivariate selection results and efficiencies for the hadronic tau decay channel. Here, the error on the SM background expectation contains the statistical error only.

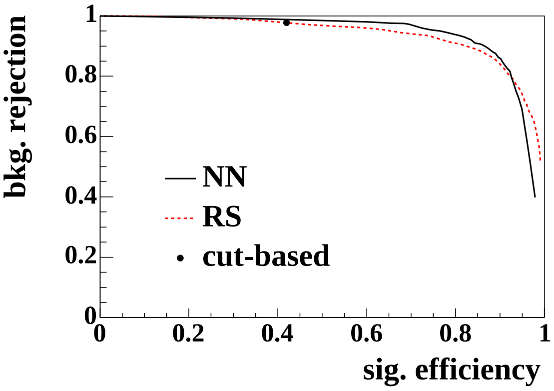

FIGURE 6.14: Performance of the applied analysis methods. The lines result from a variation of the cut value on the discriminator variable. The point for a parallel cut-based analysis including $p_{T,\mathrm{miss}}$ criteria is also shown for comparison.

6.4.3 Final selection

The final selection step in the hadronic tau decay channel makes use of the characteristic large missing transverse momentum carried by the tau neutrino which is expected to be emitted into the direction of the tau-jet.

Fig. 6.15c demonstrates the large potential for further background rejection in the distribution with a selection cut of $\Delta\phi_{\mathrm{miss}-\tau-\mathrm{jet}} < 20°$, where $\Delta\phi_{\mathrm{miss}-\tau-\mathrm{jet}}$ is the distance in ϕ between the missing transverse momentum vector and the tau-jet. A minimal value of $p_{T,\mathrm{miss}} > 12\,\mathrm{GeV}$ was chosen for an accurate determination of the direction. In addition to $p_{T,\mathrm{miss}} > 12\,\mathrm{GeV}$ a minimal value of $12\,\mathrm{GeV}$ is also demanded for the overall transverse momentum reconstructed from calorimetric deposits only, i.e. $p_{T,\mathrm{calo}} > 12\,\mathrm{GeV}$. The distributions of $p_{T,\mathrm{miss}}$ and $p_{T,\mathrm{calo}}$ do not differ significantly, but may do in some events with muonic energy involved. Such non-isolated muons are produced in the hadronisation process of jets and may

Hadronic tau decay channel final selection							
coll.	data	SM MC	m_{LQ}	S_0^R	$V_{1/2}^L$	V_0^R	$\tilde{S}_{1/2}^L$
e^-p	0	0.29 ± 0.06	150 GeV	19%	20%	20%	19%
			500 GeV	14%	10%	10%	8%
e^+p	1	2.63 ± 0.57	150 GeV	17%	17%	19%	17%
			500 GeV	11%	9%	10%	11%

TABLE 6.6: Final selection results and efficiencies for the hadronic tau decay channel. The error on the SM background expectation includes the systematic error added to the statistical error in quadrature.

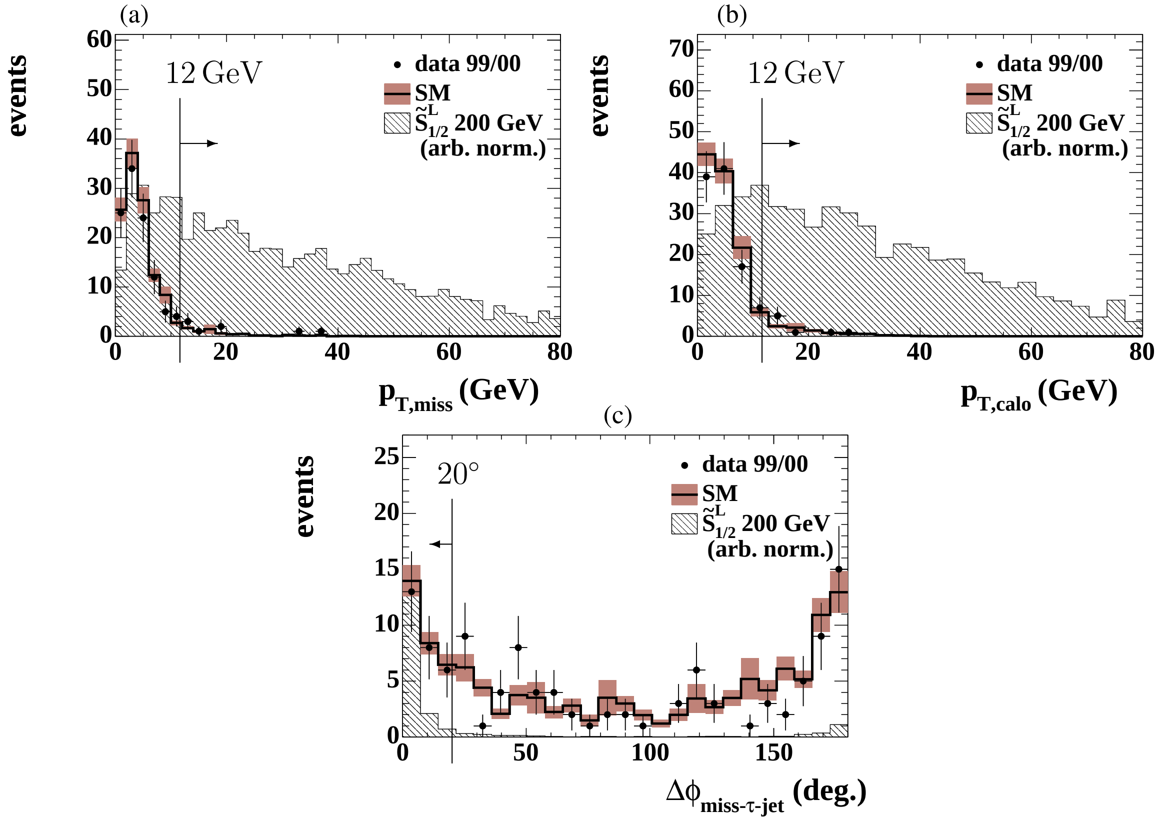

FIGURE 6.15: Missing momentum variables that are cut on in the final hadronic tau decay channel selection step.

leave a $p_{T,\mathrm{miss}}$ signature through a mismeasurement of the muon energy in the muon system. The requirement of $p_{T,\mathrm{calo}} > 12\,\mathrm{GeV}$ rejects these background events.

None of the 16 e^-p data events pass the final selection criteria and the remaining SM background amounts to $0.29 \pm 0.05\,(\mathrm{stat.}) \pm 0.03(\mathrm{sys.})$ The final yield of e^+p data events in the hadronic tau decay channel is one event (run 278414, event 63616) with an expected SM background of $2.63 \pm 0.49\,(\mathrm{stat.}) \pm 0.28(\mathrm{sys.})$. The final mass spectrum with the selected data event is depicted in Fig. 6.16. The mass is reconstructed with the double-angle method between the tau-jet and the quark-induced jet.

Fig. 6.17 is an event display of the selected event with two jets in the final sample. The tau-jet with its narrow pencil-like shape and one track associated to it is clearly visible. The jets are back-to-back in ϕ and the reconstructed missing transverse momentum of $33\,\mathrm{GeV}$ points into the $\theta\phi$-direction of the tau-jet within $2°$. From the double-angle method using the direction of the tau-jet as the outgoing electron direction and the QCD-jet as the hadronic final state vector a leptoquark mass of $171\,\mathrm{GeV}$ is determined.

Due to the fact that the tau-jet is quite close to the excluded region around a z-crack in the calorimeter as well as to that of a ϕ-crack (see Sec. 4.3.1), it can not be completely ruled out

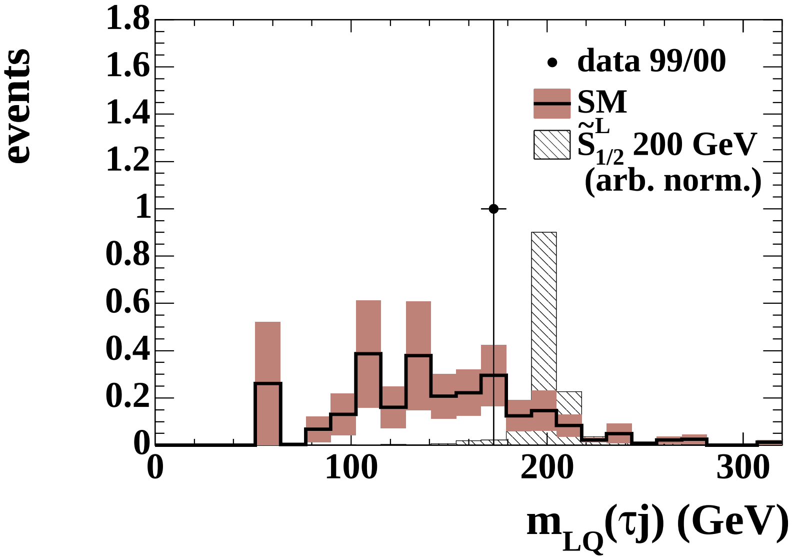

FIGURE 6.16: Leptoquark mass spectrum after final selection in the hadronic tau decay channel. The notation τj means that the value is derived with the double-angle method using the direction of the tau-jet as the outgoing electron direction and the QCD-jet as the hadronic final state vector.

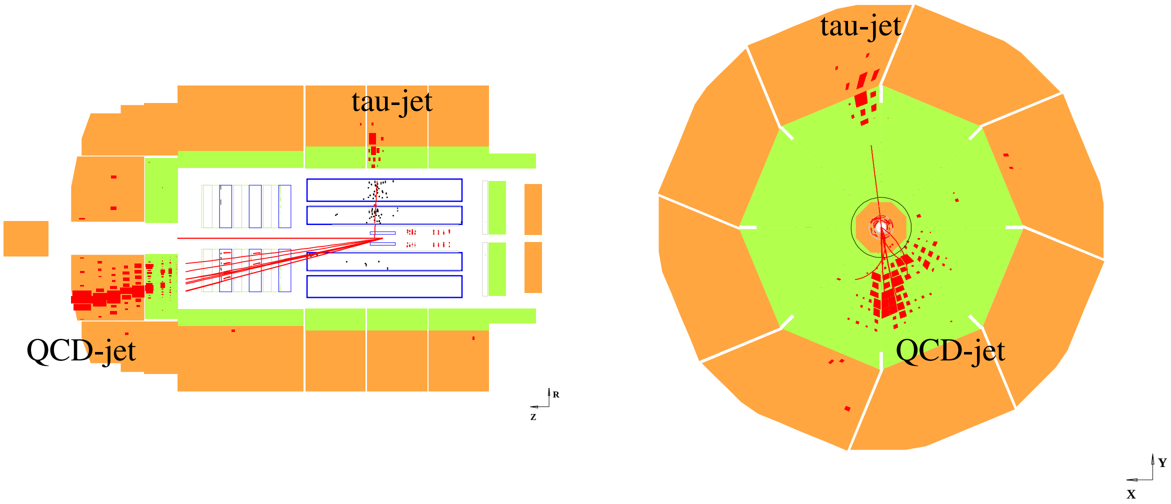

FIGURE 6.17: Event display of the e^+p data event (run 278414, event 63616) passing all selection criteria in the hadronic tau decay channel.

that this event is a NC DIS event. In fact, a background contribution of 1.89 ± 0.44 signal-like NC DIS events is expected. Assuming this event to be a NC DIS background event, an electron with some energy loss into cracks and a significant energy leakage into the hadronic part of the calorimeter is misidentified as a tau-jet. As this unlikely scenario is nearly indistinguishable from a 1-prong tau-jet and harsher fiducial cuts would significantly affect the signal selection efficiency, the event remains a candidate event for LFV. It is a striking fact that also the range search and the cut-based parallel analysis both select this event in the final analysis as a tau-quark pair candidate.

6.4.4 Signal selection efficiency

As in the other search channels the signal selection efficiency is studied in detail with regard to the deriviation of exclusion limits. Fig. 6.18 illustrates the efficiencies after the individual selection steps for some leptoquark types. The features are similar to the leptonic tau decay channels. As in all previous selection channels, the dependence of the selection efficiency on the coupling is also studied. Fig. 6.18e displays two-dimensionally the efficiency over the m_{LQ}-λ_{ei}-plane. There is almost no observed dependence on the coupling. Only for masses near the kinematic limit the efficiency is affected by the coupling. However, for the limit calculation (see. Sec 7.2.2) the exact efficiency is determined in parallel for the parameter set $\{\mathrm{LQ}, m_{\mathrm{LQ}}, \lambda_{ei}, \beta_{\mathrm{LFV}}\}$. Uncertainties from limited statistics in low-populated parameter space regions are taken into account for the error on the number of signal events.

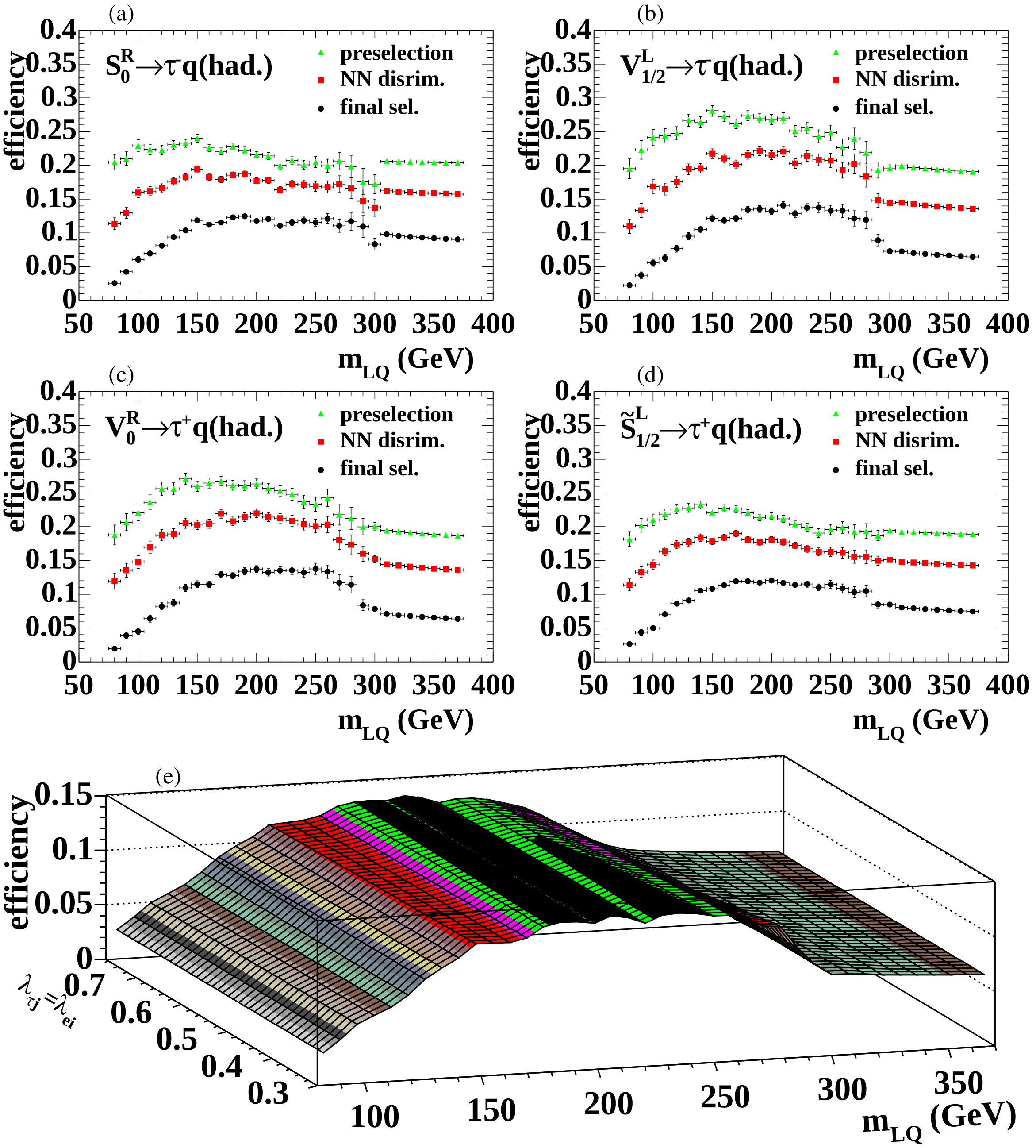

FIGURE 6.18: Selection efficiencies in the hadronic tau decay channel in the e^-p data set for $F = 2$ leptoquarks ((a),(b)) and in the e^+p data set for $F = 0$ leptoquarks ((c),(d)). It should be noted that this is the effective efficiency referring to all tau decays and the branching fraction $BR(\tau^- \rightarrow \nu_\tau + \text{hadrons}) \sim 65\%$ is implicit. (e): The dependence of the selection efficiency on the coupling $\lambda_{lj} = \lambda_{ei}$ is seen to be negligible.

Chapter 7

Statistical interpretation

The search performed for LFV shows no significant deviation from the SM in any observed channel. To exploit this experimental result exclusion limits on the parameters of the extended BRW effective leptoquark model are derived. After a summary of the selection results, the applied statistical analysis is introduced. Exclusion limits for the coupling of leptoquarks mediating LFV deduced from the search for muon-quarks pairs and tau-quarks pairs respectively are presented. For comparison with results from other experiments the limits in the high-mass region are separately interpreted and shown for possible combinations of quark-flavours. Additionally, the LFV branching ratio is opened to arbitrary values and combined limits with the latest published search of the H1 experiment for first generation leptoquarks are presented in the λ_{eq}-λ_{lq}-plane. The limits are finally compared to latest published limits on LFV by the H1 collaboration.

7.1 Selection summary

The results of the investigated search channels for leptoquark processes inducing LFV are in very good agreement with the SM. No hint for a LFV signal can be found at typical efficiencies of 38%-61% (16%-32%) in the muon (tau) channel. For a detailed summary see Tab. 7.1. The individual exclusive tau decay channels are summed up to the overall result of the search for tau-quark pairs. It is important to note that the individual channels are fully exclusive such that no event can contribute to more than one channel in any data, background or signal set.

7.2 Statistical analysis

Different approaches may be followed when it comes to the statistical analysis of experimental data and its compatibility with a given theory. Intuitively, one may enquire the experimentalist for her/his belief in a certain theoretical signal assumption after having performed the experi-

Final selection results								
channel	coll.	data	SM MC	m_{LQ}	S_0^R	$V_{1/2}^L$	V_0^R	$\tilde{S}_{1/2}^L$
$eq \to \mu q$	e^-p	0	0.18 ± 0.06	150 GeV	58%	61%	60%	58%
				500 GeV	49%	40%	42%	38%
	e^+p	0	1.03 ± 0.26	150 GeV	56%	58%	59%	56%
				500 GeV	40%	40%	39%	43%
$eq \to \tau q$	e^-p	1	0.83 ± 0.22	150 GeV	32%	32%	32%	32%
				500 GeV	26%	18%	19%	16%
	e^+p	1	5.06 ± 0.84	150 GeV	30%	29%	27%	29%
				500 GeV	21%	18%	19%	20%
$eq \to \tau q$ $\hookrightarrow$ elec.	e^-p	1	0.36 ± 0.20	150 GeV	8.9%	7.8%	7.8%	8.9%
				500 GeV	7.7%	4.5%	4.9%	4.0%
	e^+p	0	1.40 ± 0.56	150 GeV	8.2%	7.3%	4.3%	8.4%
				500 GeV	4.9%	4.9%	4.5%	5.9%
$eq \to \tau q$ $\hookrightarrow$ muon.	e^-p	0	0.18 ± 0.06	150 GeV	10.3%	10.8%	10.7%	10.3%
				500 GeV	8.7%	7.1%	7.5%	6.7%
	e^+p	0	1.03 ± 0.26	150 GeV	10.0%	10.3%	10.5%	10.0%
				500 GeV	8.7%	7.1%	7.5%	6.8%
$eq \to \tau q$ $\hookrightarrow$ had.	e^-p	0	0.29 ± 0.06	150 GeV	12.3%	13.0%	13.0%	12.3%
				500 GeV	9.1%	6.5%	6.5%	5.2%
	e^+p	1	2.63 ± 0.57	150 GeV	11.0%	11.0%	12.3%	11.0%
				500 GeV	7.1%	5.8%	6.5%	7.1%

TABLE 7.1: Summary of the selection results. Here, the tau decay branching fractions are multiplied to the signal selection efficiencies. The errors on the SM MC include statistical and systematic errors.

ment. This approach leads to the statement of a *Bayesian*[1] probability. Bayes' theorem gives the conditional probability of a theory with the constraint of the experimental results:

$$P(\text{theory}|\text{exp.}) = \frac{P(\text{exp.}|\text{theory})P(\text{theory})}{P(\text{exp.})}\,, \tag{7.1}$$

where $P(\text{theory})$ is known as the *prior* probability of the theory. The prior probability of the theory must be assumed and gives a certain subjectivity to the statistical analysis. Nevertheless, with a chosen prior probability different theories may be compared with regard to their probability of being compatible with the experimental results.

The main alternative to the Bayesian probability is the *frequentist* method. In contrast to a Bayesian approach, a frequentist statistician does not state a degree of belief in a certain theoretical prediction. Here, the probability of repeating the well-defined experiment randomly and obtaining a result that is compatible with a distinct theory is stated. In other words, the frequentist does not bet on a certain theory among others, but precisely tests the compatibility of her/his experiment with a given theory which is itself not under debate.

The differences between the methods are of a rather philosophical nature, whereas stated exclusion limits should not differ by means. The decades old debate about the advantages and disadvantages of the individual methods, which is today more relaxed, may be reviewed in more detail in [83].

7.2.1 Modified frequentist method

This thesis follows the tradition of frequentist limits at the H1 experiment.

The experimental outcome of this search manifests itself in more than a single statistical channel. Each data set contributes more or less to a certain signal sensitivity. Moreover, in the case of the search for tau-quark pairs the individual search channels represent each a channel for the statistical interpretation. If there were more data observed (and described by background), e.g. mass spectra populated in each bin with binomial statistics, each mass bin would have to be considered appropriately as a separate channel. It is now a non-trivial free choice for the frequentist to find a combination method for the multiple channels in order to make a statement whether the overall experimental outcome is signal-like or background-like.

A test statistic X needs to be defined here. The test statistic merges the statistical channels into one discriminating variable and is constructed such that it increases monotonically for increasingly signal-like and decreasingly background-like. It was shown in [84] that the *Likelihood Ratio*, for example applied in [85, 86], is a good choice for X. Rather than simply adding the channels, a Likelihood Ratio X_i is attributed to each channel.

The frequentist performs a large number of toy experiments to get a well-defined probability distribution over the test statistic. The probability distribution of observing in a toy experiment

---

[1] named after Thomas Bayes (1701-1761)

$s_i + b_i$ events with s_i signal and b_i background events ((s+b)-hypothesis) in a search channel i after the observation of d_i data events in her/his performed experiment is a Poisson distribution:

$$P(s_i + b_i) = \frac{e^{-(s_i+b_i)}(s_i + b_i)^{d_i}}{d_i!} \ . \tag{7.2}$$

The background-only hypothesis can be written as

$$P(b_i) = \frac{e^{-b_i} b_i^{d_i}}{d_i!} \ . \tag{7.3}$$

In order to give a "weight" to each channel corresponding to its signal sensitivity, the Likelihood Ratio X_i per channel is now chosen to be

$$X_i = \frac{P(s_i + b_i)}{P(b_i)} \ . \tag{7.4}$$

n statistical channels are combined through the product of the X_i to give the overall Likelihood Ratio X with

$$X = \prod_{i=1}^{n} X_i \ . \tag{7.5}$$

After performing toy experiments, confidence levels can be read off the probability distributions. The fraction of toy experiments with a value X compatible with the test statistics of the performed experiment X_{obs}, i.e. $X \leq X_{obs}$, defines the confidence level CL_{s+b} in the (s+b)-hypothesis:

$$CL_{s+b} = P_{s+b}(X \leq X_{obs}) = \int_0^{X_{obs}} \frac{dP_{s+b}}{dX} dX \ , \tag{7.6}$$

where dP_{s+b}/dX is the probability density function (p.d.f.) of the test statistic for signal and background events.

One could now state an exclusion limit, e.g. $1 - CL_{s+b} = 95\%$, for observing more than $s + b$ events. In other words, one could state the exclusion of those theoretical predictions plus background expectation which are to maximally 5% compatible with the observed data. However, this procedure has the disturbing feature that in cases where the observed data fluctuates below the predicted background the exclusion limit is unnaturally strong. The reason for this is that the observation of a large downward fluctuation is considered to be very unlikely in the first place. This is especially not true for experiments with low statistics results and in particular wrong for the observation of no events. A credible experimentalist interprets a larger background expectation in these cases as a worse experimental performance rather than as a chance to make use of the "rare" experimental outcome to set strong exclusion limits.

To overcome this well-known effect, the frequentist method is modified. It is suggested in [87] that the *sensitivity* of an experiment should be stated along with the limit. Sensitivity means here the average upper limit that would be obtained by an ensemble of experiments with the expected background and no true signal. This leads to the definition of the CL for the background-only hypothesis:

$$CL_b = P_b(X \leq X_{obs}) = \int_0^{X_{obs}} \frac{dP_b}{dX} dX \ . \tag{7.7}$$

The so-called *modified frequentist method* which is used in [4] is followed here to state a conservative exclusion limit CL_s on the number of signal events with

$$CL_s = \frac{CL_{s+b}}{CL_b} \ . \tag{7.8}$$

With the division by CL_b the dependence on the expected background is strongly reduced. As the upper limit on the number of signal events N_{lim} is set such that $CL_s \leq 5\%$ for $N \geq N_{\mathrm{lim}}$, the modified frequentist method with $0 \leq CL_b \leq 1$ is conservative compared to the classical approach.

Systematic uncertainties enter the limit calculation as an offset to the predicted number of events b_i and s_i assuming a Gaussian distribution around the average with a lower physical bound at zero.

7.2.2 Limit calculation

The application of weighting factors $w(\mathrm{LQ}, m_{\mathrm{LQ}}, \lambda_{eq}, \beta_{\mathrm{LFV}}, x, Q^2, x_e)$ (see Eq. (4.9)) to the events in the finally selected generic signal sample yields the number of signal events N which would be selected for a given set of the leptoquark model parameters:

- leptoquark type (LQ)
- m_{LQ}
- λ_{lq}, λ_{eq}
- β_{LFV}

The limit calculation searches the parameter set for which $N(\mathrm{LQ}, m_{\mathrm{LQ}}, \lambda_{eq}, \beta_{\mathrm{LFV}})$ is equal to N_{lim} with $CL_s \leq 5\%$ for $N \geq N_{\mathrm{lim}}$. It is convenient to find for each leptoquark type with a certain mass the highest coupling $\lambda_{lq} = \lambda_{eq}$ (assuming $\beta_{\mathrm{LFV}} = 0.5$) which is still compatible to 5% CL with the experiment. Higher couplings are excluded at a 95% CL. Analogously, for a fixed coupling, e.g. $\lambda_{lq} = \lambda_{eq} = 0.3$, the lowest compatible mass may be found. Hence, lower masses are excluded at a 95% CL.

For all stated limits only one non-zero LFV coupling to either the muon or tau generation, not to both, is assumed for simplicity.

In contrast to the search for first generation leptoquarks with large SM NC/CC DIS background [71], no sophisticated binning in $m_{\mathrm{LQ}}^{\mathrm{rec}}$ and y is needed in this analysis where the background is very low. Only one large single leptoquark mass bin of $0\,\mathrm{GeV} < m_{\mathrm{LQ}}^{\mathrm{rec}} < 300\,\mathrm{GeV}$

is used here for the limit calculation. The upper bin border of $m_{\mathrm{LQ}}^{\mathrm{rec}} < 300\,\mathrm{GeV}$ is set, because those rare events with reconstructed leptoquark mass values larger than $300\,\mathrm{GeV}$ are very likely to be wrongly reconstructed[2]. In combination with the low background and signal statistics in this region these bad events would have an unnaturally strong influence on the limit calculation. This is also true for the e^-p data event selected in the electronic tau channel with $m_{\mathrm{LQ}}(\mathrm{da}) = 312\,\mathrm{GeV}$. In this channel the hadron method resulting in $m_{\mathrm{LQ}}(\mathrm{H}) = 201\,\mathrm{GeV}$ should yield a similar leptoquark mass as in the double-angle method that is used here. This discrepancy is a strong hint that the event is in fact a radiative CC DIS event and the photon is falsely interpreted as a forward electron with no associated track.

7.3 Limits on eq → LQ → μq

Fig. 7.1 displays the derived upper limits on the coupling $\lambda_{\mu q}$ of a leptoquark to a muon-quark pair as a function of the leptoquark mass leading to LFV in ep collisions. For each of the 14 leptoquark types in the BRW effective model, couplings larger than the depicted limit are excluded at 95% CL. The limits are most stringent at low leptoquark masses with values $\mathcal{O}(10^{-3})$ around $m_{\mathrm{LQ}} = 100\,\mathrm{GeV}$. Corresponding to the steeply falling parton density function for high values of x, the leptoquark production cross section decreases rapidly and exclusion limits are less stringent towards higher leptoquark masses. Near the kinematical limit at $m_{\mathrm{LQ}} = \sqrt{\hat{s}}$, the minimal excluded value on $\lambda_{\mu q}$ referring to the resonantly produced leptoquark turns smoothly into a limit on the virtual effects of both an off-shell s-channel leptoquark process and a u-channel leptoquark exchange. At these high masses the process contracts more and more to an effective four-fermion interaction. As explained in Sec. 2.4 the cross section of the four-fermion interaction is proportional to the value $(\lambda_{\mu q}\lambda_{eq}/m_{\mathrm{LQ}}^2)^2$. This feature is visible in the constant increase of the exclusion limit for masses above the ep centre-of-mass energy, i.e. $\sqrt{s} = 319\,\mathrm{GeV}$. Due to initial state radiation (ISR) and very low parton densities for masses near $\sqrt{s}$ the "kink" of the transition region is shifted to somewhat smaller masses of around $290 - 300\,\mathrm{GeV}$.

Fig. 7.1 shows the limits separately for scalar and vector leptoquarks, corresponding to their fermion number. Although the legend gives in brackets the dominant production process for the individual leptoquarks, the complete analysed data set is considered for all types. Despite the fact that e^-p (e^+p) data are almost insensitive to $F = 0$ ($F = 2$) leptoquarks of mass $m_{\mathrm{LQ}} < \sqrt{\hat{s}}$, this is part of the integral statistical analysis strategy which allows for a smooth and exact limit calculation over the complete parameter space. This is especially important to set competitive limits near the kinematic border and above without erroneous approximations like the narrow width approximation (NWA). Former analyses like [73, 88] have set most stringent limits which are confined by the area of validity for such approximations.

---

[2] alternatively, with an additional requirement of the value $|(m_{\mathrm{LQ}}(\mathrm{H}) - m_{\mathrm{LQ}}(\mathrm{da}))/m_{\mathrm{LQ}}(\mathrm{da})|$ to be below a certain maximal value, the upper mass boundary may have also been extended to the kinematic limit of $319\,\mathrm{GeV}$.

$eq \rightarrow$ LQ $\rightarrow \mu q$							
$F = 0$	$S^L_{1/2}$	$S^R_{1/2}$	$\tilde{S}^L_{1/2}$	V^L_0	V^R_0	$\tilde{V}^R_0$	V^L_1
$m_{\mathrm{LQ}}(\mathrm{GeV})$	302	314	283	293	294	329	453
$F = 2$	S^L_0	S^R_0	$\tilde{S}^R_0$	S^L_1	$V^L_{1/2}$	$V^R_{1/2}$	$\tilde{V}^L_{1/2}$
$m_{\mathrm{LQ}}(\mathrm{GeV})$	282	286	267	304	291	373	335

TABLE 7.2: Lower limits on m_{LQ} with $\lambda_{\mu q} = \lambda_{eq} = 0.3$.

As no candidate event passes the final selection and the background dependence is strongly reduced in the modified frequentist method, the limits mainly depend on the signal cross section. It is noticeable that the limits on vector leptoquarks are more stringent compared to those on the scalars. The reason for this is a considerably larger cross section and a slightly higher signal selection efficiency. In each group those leptoquark types with couplings to both valence quarks exhibit the best limit. The lower PDF for d-quarks compared to u-quarks can be read off the weaker limit on leptoquarks with couplings to d-quarks only. The leptoquarks V^L_0 and V^R_0 (or S^L_0 and S^R_0 respectively) differ only by an additional decay channel of the lefthanded leptoquark type to a neutrino-quark pair. As this decay channel is not covered by the performed search, the left-handed leptoquark can not be as strictly excluded as the right-handed one. This argument applies only in case of resonant production where the analysis is sensitive only to a partial width of the leptoquark. In the high-mass region the limits for left-handed and right-handed leptoquarks are equal as the four-fermion interaction is independent of the decay width.

Assuming a coupling of electromagnetic strength, i.e. $\lambda_{\mu q} = \lambda_{eq} = 0.3$, leptoquarks mediating LFV to the muon generation are confined by this experiment at 95% CL to masses of more than $267 - 453\,\mathrm{GeV}$ depending on the leptoquark type. The lower limits on the mass for the individual types can be found in Tab. 7.2.

These limits on the leptoquark mass with an assumed coupling of $\lambda_{\mu q} = \lambda_{eq} = 0.3$ are the most stringent limits on LFV processes at HERA so far. The lack of analysed luminosity compared to [73] is compensated by the advantage of the integral statistical analysis allowing for a limit calculation at the kinematic border. However, the limits on $\lambda_{\mu q} = \lambda_{eq}$ published in [73] are somewhat stronger for leptoquark masses below $250\,\mathrm{GeV}$ due to more analysed data. Until the year 1997 the ep data were taken at a centre-of-mass energy of only $\sqrt{s} = 300\,\mathrm{GeV}$. The sensitivity of that data that was additionally analysed in [73] is marginal for leptoquark masses above $250\,\mathrm{GeV}$.

Compared to the latest published results of a search for LFV processes at HERA with the H1 experiment [74], the limits have improved overall by almost a factor 2.

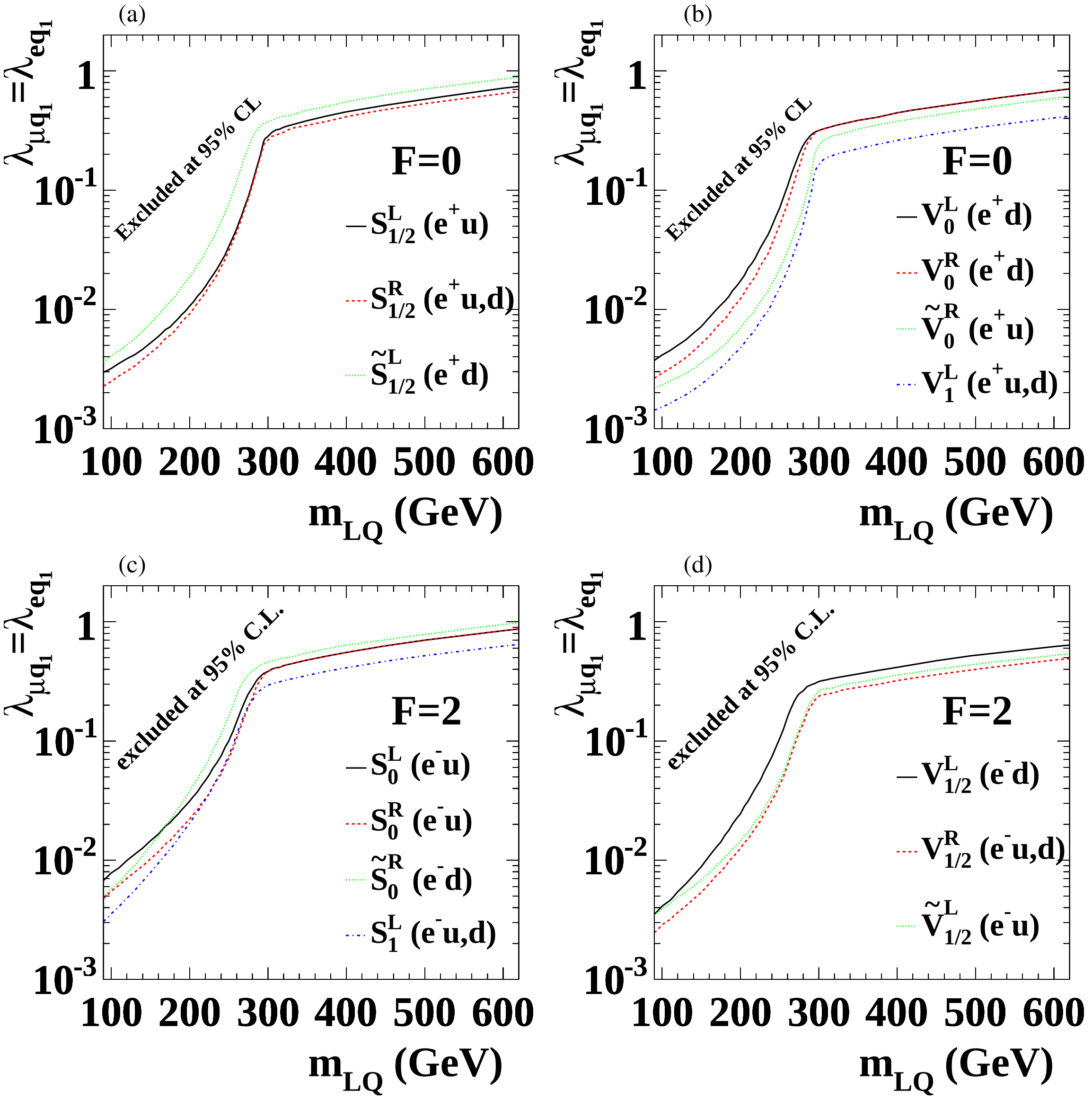

FIGURE 7.1: Limits on the coupling constant $\lambda_{\mu q} = \lambda_{eq}$ at 95% CL as a function of the leptoquark mass for $F = 0$ (a,b) and $F = 2$ (c,d) leptoquarks.

7.3.1 Contact interaction region

With respect to quark flavours this analysis is inclusive. No special tagging on individual flavours of the involved QCD-jet is applied. The dependence of the signal selection efficiency on the quark flavour is determined for each process $eq_i \to \mu q_j$ individually. Therefore, the search results may be interpreted in exclusive scenarios $eq_i \to \mathrm{LQ} \to \mu q_j$ just by the difference in the PDF and thus the expected signal cross section.

For comparison with the published results from the ZEUS collaboration [73] the limits on $\lambda_{\mu q} = \lambda_{eq}$ derived from the virtual effects of a $500\,\mathrm{GeV}$ leptoquark are transformed into a limit on the value $\lambda_{\mu q_j}\lambda_{eq_i}/m^2_{\mathrm{LQ}}$ and summarised in units of TeV^{-2} in Tab. 7.3 for $F = 0$ leptoquarks and in Tab. 7.4 for $F = 2$ leptoquarks. For each leptoquark type the limit is calculated for the exclusive hypothesis of a process with quarks of flavour i and j involved. In the picture of two distinct interaction vertices as it can be seen in Fig. 2.4, i denotes the quark generation of the incoming quark and j is the outgoing quark generation in the s-channel production. Vice versa, for the u-channel exchange j is the initial anti-quark flavour and i is the flavour of the outgoing anti-quark. The cases marked in the tables with '$*$' refer to scenarios involving a top quark. The tables also contain stringent limits on $\lambda_{\mu q_j}\lambda_{eq_i}/m^2_{\mathrm{LQ}}$ (TeV^{-2}) from low-energy experiments (taken from [73]). The interpretation of limits from low-energy experiments in terms of leptoquark processes is introduced in Sec. 2.4.1 and can be reviewed in more detail in [34, 35].

The limits derived in this analysis can not compete with the limits from dedicated low-energy experiments in most of the scenarios. However, one can see in some cases that the limits from this analysis supercede or come close to existing indirect bounds. For leptoquarks coupling to muons, this concerns in particular the leptoquarks which can contribute to the rare decay $D \to \mu\bar{e}$, i.e. $S^L_{1/2}$, $\tilde{V}^R_0$, S^R_0 or $\tilde{V}^L_{1/2}$ coupling to quark generations 1 and 2.

The limits derived by the ZEUS collaboration in [73] are shown in Tab. 7.3 and Tab. 7.4 with a preceding 'Z:'. Due to the fact that the ZEUS analysis covers more data[3] that is sensitive to the low-mass tails of the virtual effects from high-mass leptoquarks, the limits from this analysis are overall slightly weaker. It was checked that the difference is only due to a difference in the analysed data luminosity. With regard to the large differences between the detectors, the analysis methods and the statistical interpretations this result is quite remarkable.

7.4 Limits on eq $\to$ LQ $\to$ τq

In analogy to the derived limits from the search for muon-quark pairs, the results of the search for tau-quark pairs are interpreted in terms of exclusion limits at 95% CL on the coupling $\lambda_{\tau q}$ of a leptoquark to a tau-quark pair. For simplicity, the coupling $\lambda_{\mu q}$ is assumed to be zero for all limits referring to LFV processes involving a tau lepton. The limits are illustrated in Fig. 7.2

---

[3] an integrated luminosity of $\int\mathcal{L} = 130\,\mathrm{pb}^{-1}$ of which $\sim 50\,\mathrm{pb}^{-1}$ are additional e^+p data recorded in the years 1994-1997 at a centre-of-mass energy of $\sqrt{s} = 300\,\mathrm{GeV}$

$e \to \mu$ 98-00 $e^{\pm}p$ $F = 0$

upper exclusion limits on $\lambda_{eq_i}\lambda_{\mu q_j}/m_{\mathrm{LQ}}^2$ (in TeV^{-2})
for lepton flavour violating leptoquarks

$i\ j$	$S_{1/2}^L$ $e^-\bar{u}$ e^+u	$S_{1/2}^R$ $e^-(\bar{u}+\bar{d})$ $e^+(u+d)$	$\tilde{S}_{1/2}^L$ $e^-\bar{d}$ e^+d	V_0^L $e^-\bar{d}$ e^+d	V_0^R $e^-\bar{d}$ e^+d	$\tilde{V}_0^R$ $e^-\bar{u}$ e^+u	V_1^L $e^-(\sqrt{2}\bar{u}+\bar{d})$ $e^+(\sqrt{2}u+d)$
1 1	$\mu N \to eN$ 5.2×10^{-5} Z: 1.2 **1.4**	$\mu N \to eN$ 2.6×10^{-5} Z: 1.0 **1.1**	$\mu N \to eN$ 5.2×10^{-5} Z: 1.7 **2.0**	$\mu N \to eN$ 2.6×10^{-5} Z: 1.0 **1.3**	$\mu N \to eN$ 2.6×10^{-5} Z: 1.0 **1.3**	$\mu N \to eN$ 2.6×10^{-5} Z: 0.8 **0.9**	$\mu N \to eN$ 0.8×10^{-5} Z: 0.4 **0.4**
1 2	$D \to \mu\bar{e}$ 2.4 Z: 1.3 **1.4**	$K \to \mu\bar{e}$ 2×10^{-5} Z: 1.0 **1.2**	$K \to \mu\bar{e}$ 2×10^{-5} Z: 1.8 **2.0**	$K \to \mu\bar{e}$ 1×10^{-5} Z: 1.2 **1.5**	$K \to \mu\bar{e}$ 1×10^{-5} Z: 1.2 **1.5**	$D \to \mu\bar{e}$ 1.2 Z: 1.0 **1.1**	$K \to \mu\bar{e}$ 1×10^{-5} Z: 0.5 **0.5**
1 3	$*$	$B \to \mu\bar{e}$ 0.4 Z: 1.8 **2.1**	$B \to \mu\bar{e}$ 0.4 Z: 1.9 **2.1**	$B \to \mu\bar{e}$ 0.2 Z: 1.5 **1.6**	$B \to \mu\bar{e}$ 0.2 Z: 1.5 **1.6**	$*$	$B \to \mu\bar{e}$ 0.2 Z: 1.5 **1.6**
2 1	$D \to \mu\bar{e}$ 2.4 Z: 3.6 **4.2**	$K \to \mu\bar{e}$ 2×10^{-5} Z: 2.4 **2.9**	$K \to \mu\bar{e}$ 2×10^{-5} Z: 3.1 **4.1**	$K \to \mu\bar{e}$ 1×10^{-5} Z: 1.3 **1.7**	$K \to \mu\bar{e}$ 1×10^{-5} Z: 1.3 **1.7**	$D \to \mu\bar{e}$ 1.2 Z: 1.3 **1.5**	$K \to \mu\bar{e}$ 1×10^{-5} Z: 0.6 **0.7**
2 2	$\mu N \to eN$ 9.2×10^{-4} Z: 5.7 **6.0**	$\mu N \to eN$ 1.3×10^{-3} Z: 3.1 **3.7**	$\mu N \to eN$ 3×10^{-3} Z: 3.8 **4.8**	$\mu N \to eN$ 1.5×10^{-3} Z: 1.9 **2.5**	$\mu N \to eN$ 1.5×10^{-3} Z: 1.9 **2.5**	$\mu N \to eN$ 4.6×10^{-4} Z: 2.8 **3.1**	$\mu N \to eN$ 2.7×10^{-4} Z: 1.1 **1.3**
2 3	$*$	$B \to \bar{\mu}eK$ 0.3 Z: 4.3 **5.2**	$B \to \bar{\mu}eK$ 0.3 Z: 4.2 **5.2**	$B \to \bar{\mu}eK$ 0.15 Z: 2.9 **3.5**	$B \to \bar{\mu}eK$ 0.15 Z: 2.9 **3.5**	$*$	$B \to \bar{\mu}eK$ 0.15 Z: 2.9 **3.5**
3 1	$*$	$B \to \mu\bar{e}$ 0.4 Z: 4.4 **5.3**	$B \to \mu\bar{e}$ 0.4 Z: 4.4 **5.3**	V_{ub} 0.12 Z: 1.5 **1.8**	$B \to \mu\bar{e}$ 0.2 Z: 1.5 **1.8**	$*$	V_{ub} 0.12 Z: 1.5 **1.8**
3 2	$*$	$B \to \bar{\mu}eK$ 0.3 Z: 5.8 **7.0**	$B \to \bar{\mu}eK$ 0.3 Z: 5.8 **7.0**	$B \to \bar{\mu}eK$ 0.15 Z: 2.2 **2.8**	$B \to \bar{\mu}eK$ 0.15 Z: 2.2 **2.8**	$*$	$B \to \bar{\mu}eK$ 0.15 Z: 2.2 **2.8**
3 3	$*$	$\mu N \to eN$ 1.3×10^{-3} Z: 7.6 **8.3**	$\mu N \to eN$ 3×10^{-3} Z: 7.6 **8.3**	$\mu N \to eN$ 1.5×10^{-3} Z: 3.9 **4.3**	$\mu N \to eN$ 1.5×10^{-3} Z: 3.9 **4.3**	$*$	$\mu N \to eN$ 2.7×10^{-4} Z: 3.9 **4.3**

Table 7.3: Limits at 95% C.L. on $\lambda_{eq_i}\lambda_{\mu q_j}/m_{\mathrm{LQ}}^2$ for $F = 0$ leptoquarks, in units of TeV^{-2} (bold). Combinations of i and j shown in the first column denote the quark generation coupling to the electron and muon respectively. In each cell the first two rows show most stringent limits from low energy experiments. ZEUS limits for 1994-2000 $e^{\pm}p$ data from [73] are preceded by a 'Z:'. The cases marked with '$*$' refer to scenarios involving a top quark.

$e \to \mu$ 98-00 $e^{\pm}p$ $F = 2$

upper exclusion limits on $\lambda_{eq_i}\lambda_{\mu q_j}/m^2_{\text{LQ}}$ (in TeV^{-2})
for lepton flavour violating leptoquarks

$i\ j$	S_0^L e^-u $e^+\bar{u}$	S_0^R e^-u $e^+\bar{u}$	$\tilde{S}_0^R$ $e^-(u+d)$ $e^+(\bar{u}+\bar{d})$	S_1^L $e^-(u+\sqrt{2}d)$ $e^+(\bar{u}+\sqrt{2}\bar{d})$	$V_{1/2}^L$ e^-d $e^+\bar{d}$	$V_{1/2}^R$ $e^-(u+d)$ $e^+(\bar{u}+\bar{d})$	$\tilde{V}_{1/2}^L$ e^-u $e^+\bar{u}$
1 1	$\mu N \to eN$ 5.2×10^{-5} Z: 1.6 **2.0**	$\mu N \to eN$ 5.2×10^{-5} Z: 1.6 **2.0**	$\mu N \to eN$ 5.2×10^{-5} Z: 2.1 **2.6**	$\mu N \to eN$ 1.7×10^{-5} Z: 0.9 **1.0**	$\mu N \to eN$ 2.6×10^{-5} Z: 0.9 **1.1**	$\mu N \to eN$ 1.3×10^{-5} Z: 0.5 **0.6**	$\mu N \to eN$ 2.6×10^{-5} Z: 0.6 **0.8**
1 2	$K \to \pi\nu\bar{\nu}$ 1×10^{-3} Z: 2.5 **2.6**	$D \to \mu\bar{e}$ 2.4 Z: 2.5 **2.6**	$K \to \mu\bar{e}$ 2×10^{-5} Z: 2.6 **3.2**	$K \to \mu\bar{e}$ 1×10^{-5} Z: 1.2 **1.4**	$K \to \mu\bar{e}$ 1×10^{-5} Z: 1.6 **2.0**	$K \to \mu\bar{e}$ 1×10^{-5} Z: 1.2 **1.4**	$D \to \mu\bar{e}$ 1.2 Z: 1.8 **1.9**
1 3	$*$	$*$	$B \to \mu\bar{e}$ 0.4 Z: 2.9 **3.3**	V_{ub} 0.24 Z: 1.4 **1.6**	$B \to \mu\bar{e}$ 0.2 Z: 2.2 **2.5**	$B \to \mu\bar{e}$ 0.2 Z: 2.2 **2.5**	$*$
2 1	$K \to \pi\nu\bar{\nu}$ 1×10^{-3} Z: 2.1 **2.6**	$D \to \mu\bar{e}$ 2.4 Z: 2.1 **2.6**	$K \to \mu\bar{e}$ 2×10^{-5} Z: 2.5 **3.3**	$K \to \mu\bar{e}$ 1×10^{-5} Z: 1.1 **1.4**	$K \to \mu\bar{e}$ 1×10^{-5} Z: 0.9 **1.1**	$K \to \mu\bar{e}$ 1×10^{-5} Z: 0.5 **0.7**	$D \to \mu\bar{e}$ 1.2 Z: 0.6 **0.8**
2 2	$\mu N \to eN$ 9.2×10^{-4} Z: 5.7 **6.0**	$\mu N \to eN$ 9.2×10^{-3} Z: 5.7 **6.0**	$\mu N \to eN$ 3×10^{-3} Z: 3.8 **4.8**	$\mu N \to eN$ 2.5×10^{-3} Z: 1.8 **2.2**	$\mu N \to eN$ 1.5×10^{-3} Z: 1.9 **2.5**	$\mu N \to eN$ 6.7×10^{-4} Z: 1.6 **1.9**	$\mu N \to eN$ 4.6×10^{-4} Z: 2.8 **3.1**
2 3	$*$	$*$	$B \to \bar{\mu}eK$ 0.3 Z: 4.4 **5.2**	$B \to \bar{\mu}eK$ 0.15 Z: 2.2 **2.6**	$B \to \bar{\mu}eK$ 0.15 Z: 2.9 **3.5**	$B \to \bar{\mu}eK$ 0.15 Z: 2.9 **3.5**	$*$
3 1	$*$	$*$	$B \to \mu\bar{e}$ 0.4 Z: 3.1 **3.7**	$B \to \mu\bar{e}$ 0.4 Z: 1.5 **1.9**	$B \to \mu\bar{e}$ 0.2 Z: 0.9 **1.2**	$B \to \mu\bar{e}$ 0.2 Z: 0.9 **1.2**	$*$
3 2	$*$	$*$	$B \to \bar{\mu}eK$ 0.3 Z: 5.9 **7.0**	$B \to \bar{\mu}eK$ 0.15 Z: 3.0 **3.5**	$B \to \bar{\mu}eK$ 0.15 Z: 2.2 **2.8**	$B \to \bar{\mu}eK$ 0.15 Z: 2.2 **2.8**	$*$
3 3	$*$	$*$	$\mu N \to eN$ 3×10^{-3} Z: 7.7 **8.3**	$\mu N \to eN$ 2.5×10^{-3} Z: 3.9 **4.3**	$\mu N \to eN$ 1.5×10^{-3} Z: 4.0 **4.3**	$\mu N \to eN$ 6.7×10^{-4} Z: 4.0 **4.3**	$*$

TABLE 7.4: Limits at 95% C.L. on $\lambda_{eq_i}\lambda_{\mu q_j}/m^2_{\text{LQ}}$ for $F = 2$ LQs, in units of TeV^{-2} (bold). Combinations of i and j shown in the first column denote the quark generation coupling to the electron and muon respectively. In each cell the first two rows show most stringent limits from low energy experiments. ZEUS limits for 1994-2000 $e^{\pm}p$ data from [73] are preceded by a 'Z:'. The cases marked with '$*$' refer to scenarios involving a top quark.

$eq \rightarrow \mathrm{LQ} \rightarrow \tau q$							
$F = 0$	$S^L_{1/2}$	$S^R_{1/2}$	$\tilde{S}^L_{1/2}$	V^L_0	V^R_0	$\tilde{V}^R_0$	V^L_1
m_{LQ}(GeV)	294	296	276	280	285	301	371
$F = 2$	S^L_0	S^R_0	$\tilde{S}^R_0$	S^L_1	$V^L_{1/2}$	$V^R_{1/2}$	$\tilde{V}^L_{1/2}$
m_{LQ}(GeV)	276	283	260	284	274	301	294

TABLE 7.5: Lower limits on m_{LQ} with $\lambda_{\tau q} = \lambda_{eq} = 0.3$.

as a function of the leptoquark mass. The features discussed in Sec. 7.3 are similarly present here. Corresponding to a significantly lower signal selection efficiency for tau-quark pairs of 27-32% (26-26%) compared to that for muon-quark pairs of 38-43% (56-61%) assuming a 150 GeV (500 GeV) leptoquark, the limit on $\lambda_{\tau q}$ is overall weaker than that on $\lambda_{\mu q}$.

The e^+p data event selected in the hadronic tau channel is not prominent in the limit plots as only in one large leptoquark mass bin of $0\,\mathrm{GeV} < m^{\mathrm{rec}}_{\mathrm{LQ}} < 300\,\mathrm{GeV}$ is searched for.

7.4.1 Contact interaction region

The parameter space in the contact interaction region of high-mass leptoquarks that couple to tau leptons is less confined by indirect bounds than that of leptoquarks that couple to muons. Although the majority of scenarios are excluded by the presented stringent indirect bounds, the limits on $\lambda_{\tau q_j}\lambda_{eq_i}/m^2_{\mathrm{LQ}}$ derived in this work come very close in a considerable fraction of processes (see Tab. 7.6 and Tab. 7.7). Some scenarios like those involving a u- and a c-quark and the production of a leptoquark of type $S^L_{1/2}$, $\tilde{V}^R_0$, S^R_0 or $\tilde{V}^L_{1/2}$ are uniquely covered by HERA experiments. The limits for processes involving a b-quark and a c-quark or b-quarks only are even more stringent. Also the bounds calculated from the results of searches for the LFV tau decay $\tau \rightarrow Ke$ are superceded by this analysis.

Concerning the comparison with the bounds from the ZEUS collaboration [73], the same difference due to a smaller analysed data luminosity is observed as seen in the case of LFV transitions $e \rightarrow \mu$ (see Sec. 7.3.1). The limits deduced in this analysis are overall slightly weaker than those in [73]. Nevertheless, the bounds have improved by a factor ~ 1.5 with respect to the latest published H1 results in [74].

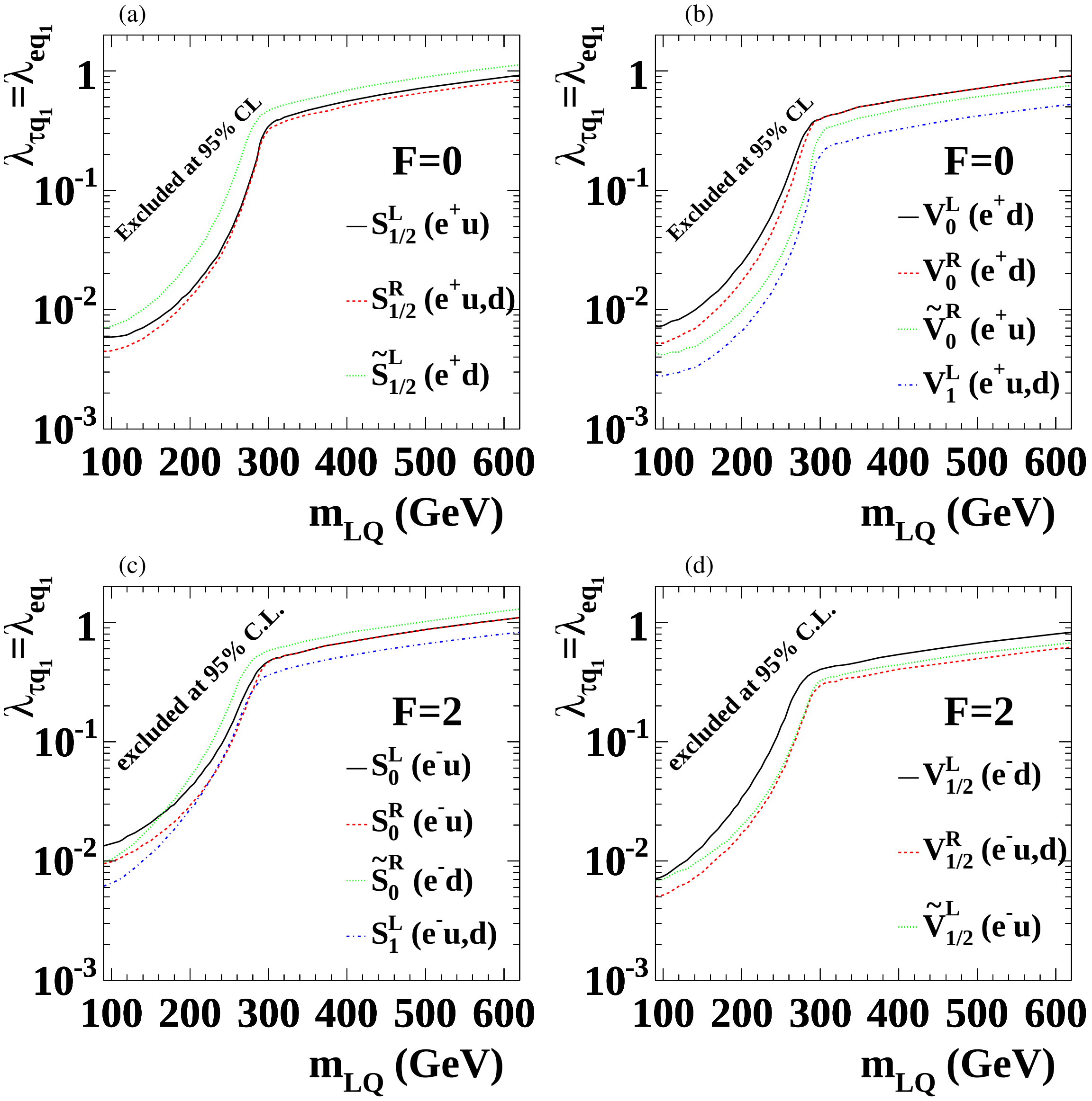

FIGURE 7.2: Limits on the coupling constant $\lambda_{\tau q} = \lambda_{eq}$ at 95% CL as a function of the leptoquark mass for $F = 0$ (a,b) and $F = 2$ (c,d) leptoquarks.

$e \to \tau$ 98-00 $e^{\pm}p$ $F = 0$

upper exclusion limits on $\lambda_{eq_i}\lambda_{\tau q_j}/m^2_{\mathrm{LQ}}$ (in TeV^{-2})
for lepton flavour violating leptoquarks

$i\ j$	$S^L_{1/2}$ $e^-\bar{u}$ e^+u	$S^R_{1/2}$ $e^-(\bar{u}+\bar{d})$ $e^+(u+d)$	$\tilde{S}^L_{1/2}$ $e^-\bar{d}$ e^+d	V^L_0 $e^-\bar{d}$ e^+d	V^R_0 $e^-\bar{d}$ e^+d	$\tilde{V}^R_0$ $e^-\bar{u}$ e^+u	V^L_1 $e^-(\sqrt{2}\bar{u}+\bar{d})$ $e^+(\sqrt{2}u+d)$
1 1	$\tau \to \pi e$ 0.4 Z: 1.8 **2.1**	$\tau \to \pi e$ 0.2 Z: 1.5 **1.8**	$\tau \to \pi e$ 0.4 Z: 2.7 **3.1**	$\tau \to \pi e$ 0.2 Z: 1.7 **2.1**	$\tau \to \pi e$ 0.2 Z: 1.7 **2.1**	$\tau \to \pi e$ 0.2 Z: 1.3 **1.5**	$\tau \to \pi e$ 0.06 Z: 0.6 **0.7**
1 2	Z: 1.9 **2.2**	$\tau \to Ke$ 6.3 Z: 1.6 **1.8**	$K \to \pi\nu\bar{\nu}$ 5.8×10^{-4} Z: 2.9 **3.2**	$\tau \to Ke$ 3.2 Z: 2.1 **2.5**	$\tau \to Ke$ 3.2 Z: 2.1 **2.5**	Z: 1.6 **1.7**	$K \to \pi\nu\bar{\nu}$ 1.5×10^{-4} Z: 0.8 **0.8**
1 3	$*$	$B \to \tau\bar{e}$ 0.3 Z: 3.2 **3.2**	$B \to \tau\bar{e}$ 0.3 Z: 3.3 **3.2**	$B \to \tau\bar{e}$ 0.13 Z: 2.6 **2.7**	$B \to \tau\bar{e}$ 0.13 Z: 2.6 **2.7**	$*$	$B \to \tau\bar{e}$ 0.13 Z: 2.6 **2.7**
2 1	Z: 6.0 **6.7**	$\tau \to Ke$ 6.3 Z: 4.1 **4.8**	$K \to \pi\nu\bar{\nu}$ 5.8×10^{-4} Z: 5.2 **6.9**	$\tau \to Ke$ 3.2 Z: 2.3 **2.8**	$\tau \to Ke$ 3.2 Z: 2.3 **2.9**	Z: 2.1 **2.3**	$K \to \pi\nu\bar{\nu}$ 1.5×10^{-4} Z: 0.9 **1.1**
2 2	$\tau \to 3e$ 5.0 Z: 10.0 **10.9**	$\tau \to 3e$ 8.0 Z: 5.6 **6.7**	$\tau \to 3e$ 17.0 Z: 6.5 **8.6**	$\tau \to 3e$ 9.0 Z: 3.4 **4.5**	$\tau \to 3e$ 9.0 Z: 3.4 **4.5**	$\tau \to 3e$ 3.0 Z: 5.5 **5.5**	$\tau \to 3e$ 1.6 Z: 2.1 **2.4**
2 3	$*$	$B \to \tau\bar{e}X$ 14.0 Z: 8.1 **9.3**	$B \to \tau\bar{e}X$ 14.0 Z: 7.8 **9.3**	$B \to \tau\bar{e}X$ 7.2 Z: 5.5 **6.3**	$B \to \tau\bar{e}X$ 7.2 Z: 5.5 **6.3**	$*$	$B \to \tau\bar{e}X$ 7.2 Z: 5.5 **6.3**
3 1	$*$	$B \to \tau\bar{e}$ 0.3 Z: 7.8 **9.1**	$B \to \tau\bar{e}$ 0.3 Z: 7.2 **9.1**	V_{ub} 0.12 Z: 2.5 **3.0**	$B \to \tau\bar{e}$ 0.13 Z: 2.5 **3.0**	$*$	V_{ub} 0.12 Z: 2.5 **3.0**
3 2	$*$	$B \to \tau\bar{e}X$ 14.0 Z: 11.0 **12.6**	$B \to \tau\bar{e}X$ 14.0 Z: 10.0 **12.6**	$B \to \tau\bar{e}X$ 7.2 Z: 4.2 **4.9**	$B \to \tau\bar{e}X$ 7.2 Z: 4.2 **4.9**	$*$	$B \to \tau\bar{e}X$ 7.2 Z: 4.2 **4.9**
3 3	$*$	$\tau \to 3e$ 8.0 Z: 15.0 **15.2**	$\tau \to 3e$ 17.0 Z: 14.0 **15.2**	$\tau \to 3e$ 9.0 Z: 8.1 **8.1**	$\tau \to 3e$ 9.0 Z: 8.1 **8.1**	$*$	$\tau \to 3e$ 1.6 Z: 8.1 **8.1**

TABLE 7.6: Limits at 95% C.L. on $\lambda_{eq_i}\lambda_{\tau q_j}/m^2_{\mathrm{LQ}}$ for $F = 0$ LQs, in units of TeV^{-2} (bold). Combinations of i and j shown in the first column denote the quark generation coupling to the electron and tau respectively. In each cell the first two rows show most stringent limits from low energy experiments. ZEUS limits for 1994-2000 $e^{\pm}p$ data from [73] are preceded by a 'Z:'. The cases marked with '$*$' refer to scenarios involving a top quark.

$e \to \tau$ 98-00 $e^{\pm}p$ $F = 2$

upper exclusion limits on $\lambda_{eq_i}\lambda_{\tau q_j}/m^2_{\mathrm{LQ}}$ (in TeV^{-2})
for lepton flavour violating leptoquarks

$i\ j$	S_0^L $e^- u$ $e^+ \bar{u}$	S_0^R $e^- u$ $e^+ \bar{u}$	$\tilde{S}_0^R$ $e^-(u+d)$ $e^+(\bar{u}+\bar{d})$	S_1^L $e^-(u+\sqrt{2}d)$ $e^+(\bar{u}+\sqrt{2}\bar{d})$	$V_{1/2}^L$ $e^- d$ $e^+ \bar{d}$	$V_{1/2}^R$ $e^-(u+d)$ $e^+(\bar{u}+\bar{d})$	$\tilde{V}_{1/2}^L$ $e^- u$ $e^+ \bar{u}$
1 1	G_F 0.3 Z: 2.5 **3.0**	$\tau \to \pi e$ 0.4 Z: 2.5 **3.0**	$\tau \to \pi e$ 0.4 Z: 3.5 **4.2**	$\tau \to \pi e$ 0.1 Z: 1.4 **1.7**	$\tau \to \pi e$ 0.2 Z: 1.4 **1.8**	$\tau \to \pi e$ 0.1 Z: 0.8 **1.0**	$\tau \to \pi e$ 0.2 Z: 1.0 **1.2**
1 2	$K \to \pi\nu\bar{\nu}$ 5.8×10^{-4} Z: 4.0 **4.0**	Z: 4.0 **4.0**	$\tau \to Ke$ 6.3 Z: 4.4 **5.0**	$K \to \pi\nu\bar{\nu}$ 2.9×10^{-4} Z: 1.9 **2.1**	$K \to \pi\nu\bar{\nu}$ 2.9×10^{-4} Z: 2.8 **3.5**	$\tau \to Ke$ 3.2 Z: 2.0 **2.3**	Z: 3.1 **3.1**
1 3	$*$	$*$	$B \to \tau\bar{e}$ 0.3 Z: 5.1 **5.3**	V_{ub} 0.12 Z: 2.6 **2.7**	$B \to \tau\bar{e}$ 0.13 Z: 4.0 **4.2**	$B \to \tau\bar{e}$ 0.13 Z: 4.0 **4.2**	$*$
2 1	$K \to \pi\nu\bar{\nu}$ 5.8×10^{-4} Z: 3.2 **4.2**	Z: 3.2 **4.2**	$\tau \to Ke$ 6.3 Z: 4.3 **5.5**	$K \to \pi\nu\bar{\nu}$ 2.9×10^{-4} Z: 1.8 **2.3**	$K \to \pi\nu\bar{\nu}$ 2.9×10^{-4} Z: 1.4 **1.8**	$\tau \to Ke$ 3.2 Z: 0.8 **1.1**	Z: 1.0 **1.2**
2 2	$\tau \to 3e$ 5.0 Z: 10.0 **10.8**	$\tau \to 3e$ 5.0 Z: 10.0 **10.9**	$\tau \to 3e$ 17.0 Z: 6.5 **8.6**	$\tau \to 3e$ 14.0 Z: 3.2 **3.9**	$\tau \to 3e$ 9.0 Z: 3.5 **4.5**	$\tau \to 3e$ 4.0 Z: 2.8 **3.5**	$\tau \to 3e$ 3.0 Z: 5.1 **5.5**
2 3	$*$	$*$	$B \to \bar{\tau}eX$ 14.0 Z: 8.3 **9.3**	$B \to \bar{\tau}eX$ 7.2 Z: 4.1 **4.7**	$B \to \bar{\tau}eX$ 7.2 Z: 5.4 **6.3**	$B \to \bar{\tau}eX$ 7.2 Z: 5.4 **6.3**	$*$
3 1	$*$	$*$	$B \to \tau\bar{e}$ 0.3 Z: 5.3 **6.3**	$B \to \tau\bar{e}$ 0.13 Z: 2.7 **3.1**	$B \to \tau\bar{e}$ 0.13 Z: 1.6 **1.9**	$B \to \tau\bar{e}$ 0.13 Z: 1.6 **1.9**	$*$
3 2	$*$	$*$	$B \to \bar{\tau}eX$ 14.0 Z: 11.0 **12.6**	$B \to \bar{\tau}eX$ 7.2 Z: 5.5 **6.4**	$B \to \bar{\tau}eX$ 7.2 Z: 4.1 **4.9**	$B \to \bar{\tau}eX$ 7.2 Z: 4.1 **4.9**	$*$
3 3	$*$	$*$	$\tau \to 3e$ 17.0 Z: 15.0 **15.2**	$\tau \to 3e$ 14.0 Z: 7.6 **7.8**	$\tau \to 3e$ 9.0 Z: 7.6 **8.1**	$\tau \to 3e$ 4.0 Z: 7.6 **8.1**	$*$

TABLE 7.7: Limits at 95% C.L. on $\lambda_{eq_i}\lambda_{\tau q_j}/m^2_{\mathrm{LQ}}$ for $F = 2$ LQs, in units of TeV^{-2} (bold). Combinations of i and j shown in the first column denote the quark generation coupling to the electron and tau respectively. In each cell the first two rows show most stringent limits from low energy experiments. ZEUS limits for 1994-2000 $e^{\pm}p$ data from [73] are preceded by a 'Z:'. The cases marked with '$*$' refer to scenarios involving a top quark.

7.5 Free β_{LFV} and combination with first generation leptoquarks

The assumption of $\beta_{\mathrm{LFV}} = 0.5$ made so far is arbitrarily chosen and not confined to a certain value by theory. Thus, the LFV branching ratio β_{LFV} is relaxed in this section. For very low values of β_{LFV} the bound is dominated by the coupling strength λ_{eq} at the leptoquark production vertex. It is clear, that a dedicated search for first generation leptoquarks decaying via the same coupling λ_{eq} without LFV to an electron(neutrino)-quark in a NC(CC) DIS data set is much more appropriate to constrain λ_{eq} than this analysis searching for LFV decays only.

The H1 experiment has recently published a search for first generation leptoquarks [71]. In order to set most stringent limits in the parameter space with a relaxed LFV branching ratio, the results of that search are combined with this analysis[4]. An exact rerun of the statistical analysis of the search results of the complete NC(CC) DIS data sets covered in [71] is performed. The main differences between this LFV analysis are outlined in the following and may be studied in more detail in [71]:

- The search covers leptoquark decays to neutrino-quark pairs by analysing selected SM CC DIS data.

- The processes including first generation leptoquarks interfere with the SM NC/CC DIS processes due to equal final states. Such interferences are taken into account.

- Rather than signal events produced with a dedicated signal generator, the events simulated by the SM NC/CC DIS MC are reweighted to yield the signal-plus-background expectation (including interference).

- The analysed data sets are recorded in the years 1994-2000 corresponding to an integrated luminosity of $102\,\mathrm{pb}^{-1}$ for e^+p collisions and $15\,\mathrm{pb}^{-1}$ for e^-p collisions. $37\,\mathrm{pb}^{-1}$ of the analysed e^+p data are taken in the years 1994-1997 at a centre-of-mass energy of $\sqrt{s} = 300\,\mathrm{GeV}$.

- In order to optimise the statistical analysis in the final data sample with a large NC/CC DIS background contribution, the data are studied in bins in the $m_{\mathrm{LQ}} - y$ plane. The number of bins in the statistical analysis amounts to about 200.

All these statistical analysis bins are added to the analysis bins of this LFV analysis. According to [71] the combination of statistical bins is performed with the method of *fractional event counting* [89] instead of the previously used test statistic of a likelihood ratio. It was

---

[4] although this argument also applies for the limits presented in the previous sections, the combination was not performed therein, in order not to obscure the distinct results of this analysis.

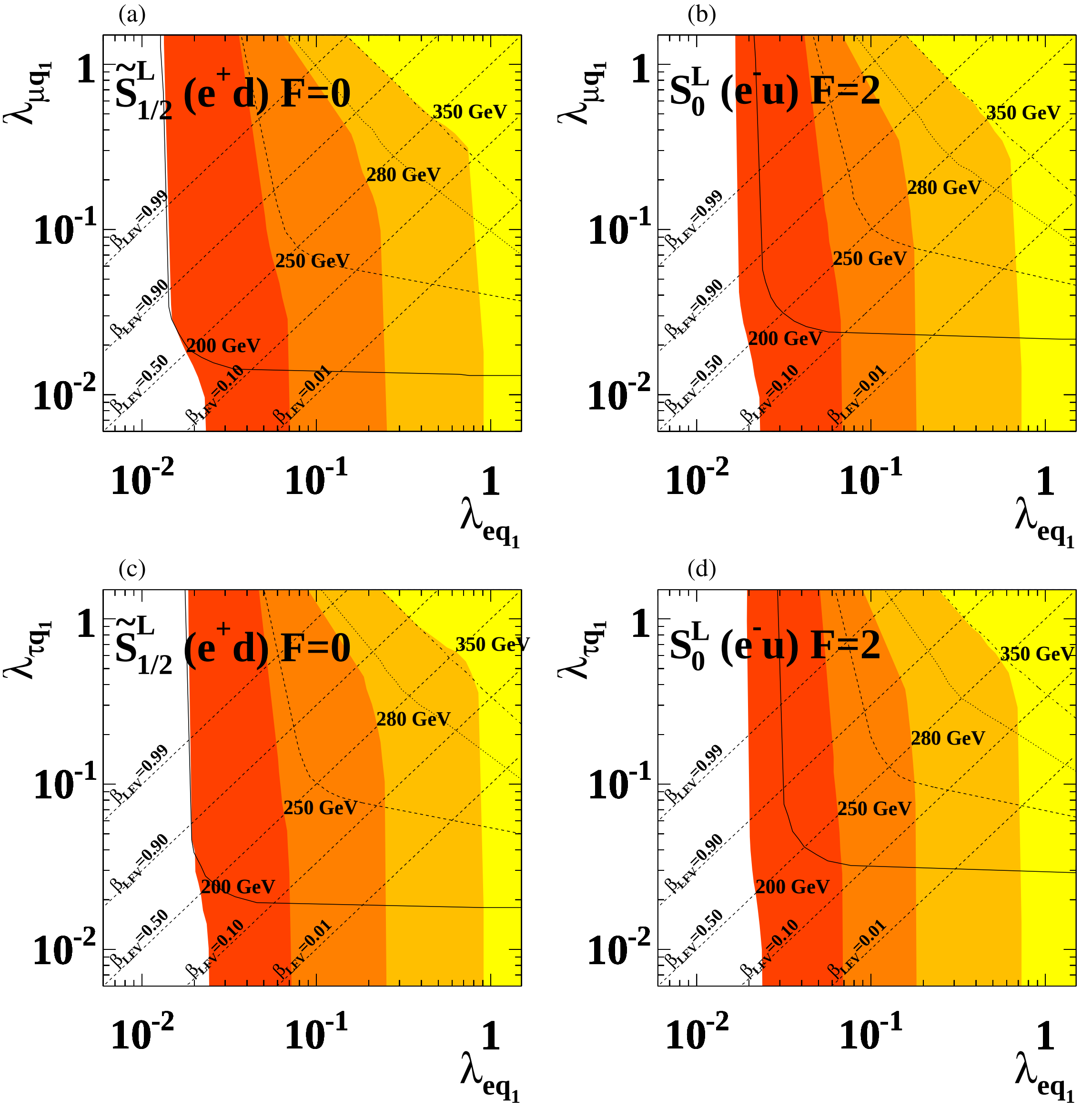

FIGURE 7.3: Excluded regions (filled, 95% CL) on λ_{lq} as a function of λ_{eq} where the branching ratio $\beta_{\mathrm{LFV}} = \lambda_{lq}^2/(\lambda_{lq}^2 + \lambda_{eq}^2)$ is not fixed for four different leptoquark masses. The leptoquarks S_0^L and $\tilde{S}_{1/2}^L$ may be interpreted as a down-type squark and an up-type squark respectively in an R_p-violating SUSY scenario with $\lambda'_{1jk} \neq 0$ and a coupling inducing LFV with $\lambda'_{2jk} \neq 0$ or $\lambda'_{3jk} \neq 0$. Diagonal dashed lines represent iso-curves for fixed values of β_{LFV}. The bounds deduced without the combination with first generation leptoquarks are shown as black curves in different dash styles.

checked that differences between the methods are negligible. In the method of fractional event counting a weight

$$w_i = \frac{(b_i + s_i) - b_i}{(b_i + s_i) + b_i} = \frac{s_i}{2b_i + s_i} \tag{7.9}$$

corresponding to the asymmetry between the presence and absence of a signal hypothesis is attributed to each bin. Following a frequentist approach, the Poisson distribution of the individual test statistics

$$X(d) = \sum_i w_i N_i(d), \;\; X(b) = \sum_i w_i N_i(b), \;\; X(b+s) = \sum_i w_i N_i(b+s) \tag{7.10}$$

as a weighted sum over all bins for the selected data events $N_i(d)$ and the SM background (plus signal) $N_i(b)$ ($N_i(b+s)$) is then obtained from a large number of generated experiments. The systematic uncertainties enter again as an offset to the predicted number of events b_i and $b_i + s_i$.

The resulting limits on the signal parameter space are displayed for two leptoquark types in Fig. 7.3 as excluded regions in the $\lambda_{\mu q_1} - \lambda_{eq_1}$ plane (b,d) and $\lambda_{\tau q_1} - \lambda_{eq_1}$ plane (a,c) for four different leptoquark masses. The leptoquark types S_0^L and $\tilde{S}_{1/2}^L$ are chosen such that the limits may be interpreted as a down-type squark and an up-type squark respectively in an R_p-violating SUSY scenario with $\lambda'_{1jk} \neq 0$ and a coupling inducing LFV with $\lambda'_{2jk} \neq 0$ or $\lambda'_{3jk} \neq 0$. For very low values of $\beta_{\rm LFV}$ the limits turn into the bounds published in [71].

Following the iso-curves for fixed values of $\beta_{\rm LFV}$ and comparing the intersections with the excluded regions for a certain leptoquark mass assumption with the limit deduced without the combination with first generation leptoquarks the advantage of combining results becomes apparent. As expected, for low values of $\beta_{\rm LFV}$ the limit on a LFV scenario is dominated by the limit on the coupling λ_{eq} at the production vertex. For $\beta_{\rm LFV} \gg 0.5$ this analysis extends significantly the published limits on λ_{eq} to lower values.

Considering only this analysis the limit in the contact-interaction region on LFV processes (which is proportional to $\lambda_{eq_i}\lambda_{lq_j}/m_{\rm LQ}^2$) leads to a cross-diagonal straight line following different values of $\beta_{\rm LFV}$. The four-fermion interaction with first generation leptoquarks is independent giving rise to the sharp “kink” in the excluded region of a 350 GeV leptoquark after combination with the search for first generation leptoquarks. For even higher masses where the high-mass approximation (HMA) is valid the kink is more pronounced. The fact that the kink tends to much lower values of $\beta_{\rm LFV}$ than 0.5 shows that the sensitivity for leptoquark scenarios with LFV is largest in dedicated decay channels rather than when restricted to the production of first generation leptoquarks only.

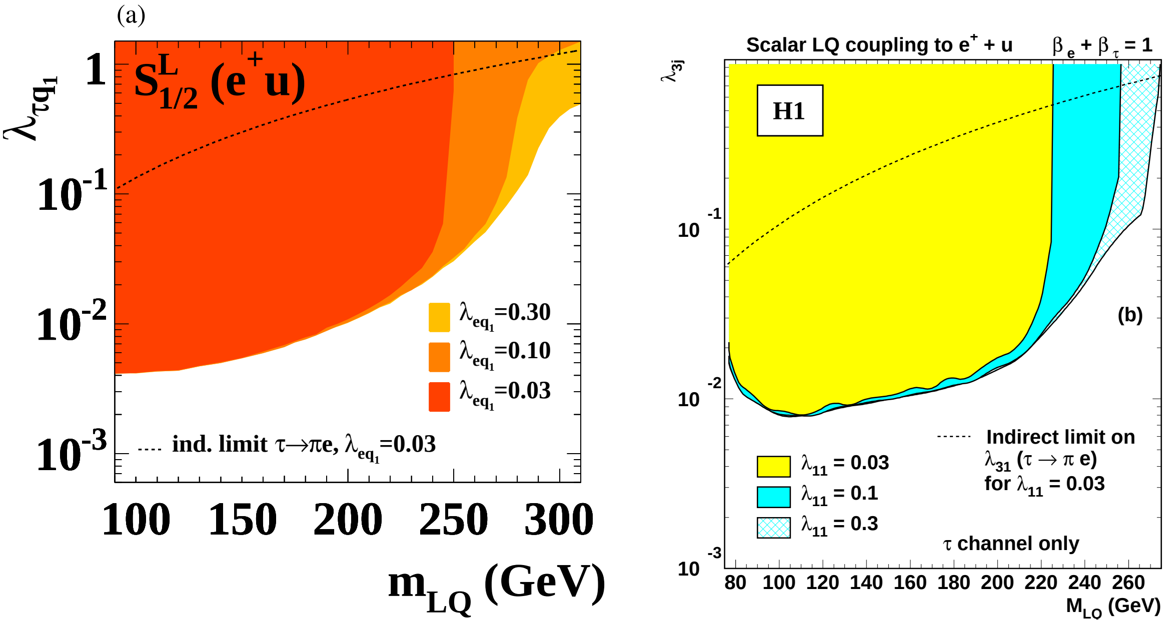

FIGURE 7.4: Limits on $\lambda_{\tau q_1}$ for fixed values of λ_{eq_1} (a) in comparison with latest H1 limits (b) published in [74]. The dashed curve shows the indirect limit from the process $\tau \to \pi e$ at $\lambda_{eq_1}\lambda_{\tau q_1}/m^2_{\mathrm{LQ}} = 0.4\,\mathrm{TeV}^{-2}$.

7.6 Limits in comparison

7.6.1 Comparison with latest H1 limits

The limits derived in this analysis are compared directly to the latest H1 limits published in [74]. In Fig. 7.4 the limits on $\lambda_{\tau q_1}$ (a) are compared to those in [74] (b). In both plots the limit on $S^L_{1/2}$ coupling to a u-quark as a function of the leptoquark mass is chosen to show for three fixed values of λ_{eq_1}. The indirect limit from the process $\tau \to \pi e$ at $\lambda_{eq_1}\lambda_{\tau q_1}/m^2_{\mathrm{LQ}} = 0.4\,\mathrm{TeV}^{-2}$ is depicted as a dashed curve. Assuming a scenario with $\lambda_{eq_1} = 0.3$ this analysis supercedes the indirect limit by far for all leptoquark masses. Even for couplings down to values of $\lambda_{eq_1} = 0.03$ the limits derived in this analysis are stronger than the indirect bounds for leptoquark masses up to $250\,\mathrm{GeV}$.

For the comparison with the limits in [74] it should be noted that in the published analysis only e^+p data at a centre-of-mass energy of $300\,\mathrm{GeV}$ were studied. The integrated luminosity of the analysed data is at $\mathcal{L} = 37\,\mathrm{pb}^{-1}$ also considerably lower. The published limits are completely superceded by this analysis. The limits derived in this work are about a factor 2 more stringent for low leptoquarks masses of about $100\,\mathrm{GeV}$. The data with $\sqrt{s} = 319\,\mathrm{GeV}$ show more sensitivity to resonances with high leptoquark masses. The reweighting method to estimate the signal efficiency allows for an extension of the analysis to leptoquark masses near and above the kinematic limit where former H1 analyses are not sensitive.

7.6.2 Limits from other collider experiments

The experiments CDF and DØ at the TEVATRON $p\bar{p}$ collider also perform searches for processes with leptoquarks. In contrast to the resonant production at HERA, leptoquarks are mainly produced in pairs in $p\bar{p}$ collisions. Therefore, CDF and DØ experiments are nearly insensitive to the coupling of leptoquarks, but they may set strong limits on the mass of second and third generation leptoquarks, respectively. Complementary to HERA, the branching ratio of a leptoquark coupling to a muon-quark pair or tau-quark pair may assumed to be 1. The latest publication of the DØ experiment states a lower limit of $247\,\mathrm{GeV}$ $(182\,\mathrm{GeV})$ on the mass of scalar leptoquarks coupling with a branching ratio of 1 (0.5) to a muon-quark pair [90]. The CDF collaboration recently released a preliminary lower limit of $282\,\mathrm{GeV}$ on the mass of vector leptoquarks coupling exclusively to tau-quark pairs with the nominal choice of parton distribution functions and Q^2 scale [91]. Obviously, those limits do not refer to LFV processes and all leptoquark scenarios covered in this work. Nevertheless, the limits are interleaved with the limits on LFV deduced here and may be compared with caution.

At the LEP e^+e^- collider the pair-production of leptoquarks via a photon or Z-boson was searched for as well as the “radiation” of a single leptoquark from the electron or positron line. The latest limits from the OPAL experiment exclude pair-produced leptoquarks of any exclusive generation with masses of up to about $100\,\mathrm{GeV}$ [92]. More competitive are limits from the single leptoquark production. Here, the sensitivity is complementary to the TEVATRON experiments as the cross section strongly depends on the coupling and has little dependence on the leptoquark mass. In [93] only limits on the coupling of first generation leptoquarks are set. These limits are only for high masses competitive to those obtained by the H1 experiment in [71].

In comparison to the limits from other collider experiments, the limits derived in this work are competitive and complementary.

Chapter 8

Summary and Outlook

This work represents a search for lepton flavour violating processes (LFV) in ep collisions with the H1 experiment at HERA. As lepton flavour is conserved in the Standard Model (SM), any observation of LFV would clearly indicate evidence for new physical phenomena. With regard to promising theoretical models beyond the SM connecting the lepton sector and the quark sector, LFV may be induced by leptoquarks being resonantly produced in the hard scattering process of an electron and a quark from the proton. A search for a subsequent leptoquark decay to a muon-quark pair or a tau-quark pair is performed.

The data analysed in this thesis are recorded with the H1 detector during the years 1998 to 2000 corresponding to an integrated luminosity of $66.5\,\mathrm{pb}^{-1}$ for e^+p collisions and $13.7\,\mathrm{pb}^{-1}$ for e^-p collisions.

The search for processes in ep collisions exhibiting LFV of the kind $e \to \mu$ is based on the signal expectation of an isolated high-p_T muon *back-to-back* in ϕ with respect to the high-p_T hadronic jet from the struck quark of the proton. The performed selection achieves efficiencies up to 60% depending on the type and mass of the leptoquark that induces LFV. No data event is selected in the final sample. The expected SM background amounts to 1.03 ± 0.26 in the e^+p set and 0.18 ± 0.06 in the e^-p sample. From this result exclusion limits on all 14 leptoquark types in an extension of the Buchmüller-Rückl-Wyler effective model are derived. For a coupling of electromagnetic strength some models with leptoquark masses up to $453\,\mathrm{GeV}$ coupling to a muon-quark pair can be excluded at 95% confidence level depending on the leptoquark type. These limits represent the most stringent bounds on LFV processes of the form $e \to \mu$ at HERA so far.

Due to the short lifetime of the tau lepton ($\tau_\tau \approx 290\,\mathrm{fs}$) the search for $e \to \tau$ transitions in ep collisions is more complicated. To achieve a total signal selection efficiency of up to 32% depending on the type and mass of the leptoquark, both electronic and muonic decay channels of the tau are covered in this search as well as the hadronic tau decays. The search for muonic tau decays follows that for direct $e \to \mu$ transitions. The characteristic $p_{T,\mathrm{miss}}$-signature from the neutrinos in the event is exploited to identify electronic tau decays. The delicate discrimination between jets from a hadronic tau decay and those induced by quarks or gluons is optimised by using a neural network based on jet shape estimator variables.

The combination of the three exclusive tau decay channels yield in total 1 data event over an expected SM background of 4.78 ± 0.76 in the e^+p set and 1 data event in the e^-p set where 0.72 ± 0.16 are expected from SM.

Based on this search result stringent limits on the LFV transition $e \rightarrow \tau$ in ep collisions are deduced. Leptoquarks with a coupling of electromagnetic strength to a tau-quark pair and masses up to $371\ \mathrm{GeV}$ depending on the leptoquark type are ruled out at 95% confidence level.

Comparison with results from dedicated low-energy experiments show that the derived limits on high-mass leptoquarks in the contact interaction region are competitive and even more stringent in a few distinct scenarios. Published bounds from the ZEUS experiment are slightly more stringent for low and high mass leptoquarks due to a larger analysed data set. The transition region of LFV processes from the resonant leptoquark production to the contact interaction region is covered in this work for the first time at HERA. Earlier published H1 limits are at least about a factor 2 less stringent and therefore completely superceded by this analysis. In comparison to the limits from experiments at other colliders such as TEVATRON or LEP, the limits on LFV deduced from this search in ep collisions are competitive and complementary.

In the years 2001 to 2003 the HERA collider and its experiments were upgraded to allow for a larger specific luminosity[1] and a longitudinally polarised lepton beam. Since then, a prosperous and still ongoing data taking period (HERAII) has accumulated $e^{\pm}p$ data that amounts up to now to a total luminosity (HERAI+II) of more than $300\,\mathrm{pb}^{-1}$. The analysis of that data has already started and will benefit from the larger statistics compared to the HERAI data that is covered in this thesis. The longitudinally polarised lepton beam provides additional sensitivity to certain leptoquark scenarios.

By the end of 2007 the HERA collider operation comes to en end and the Large Hadron Collider (LHC) at CERN in Geneva, Switzerland, starts the first data taking period. With high-energy pp collisions reaching the TeV scale, new physical phenomena such as supersymmetry may show up and provide a solution to the hierarchy problem of the SM. The question about the existence of leptoquarks and LFV will be answered for masses up to $1\ \mathrm{TeV}$.

New physics may lurk around the corner.

---

[1] due to an enhanced collimation of the beams near the interaction points

Appendix A

Event displays

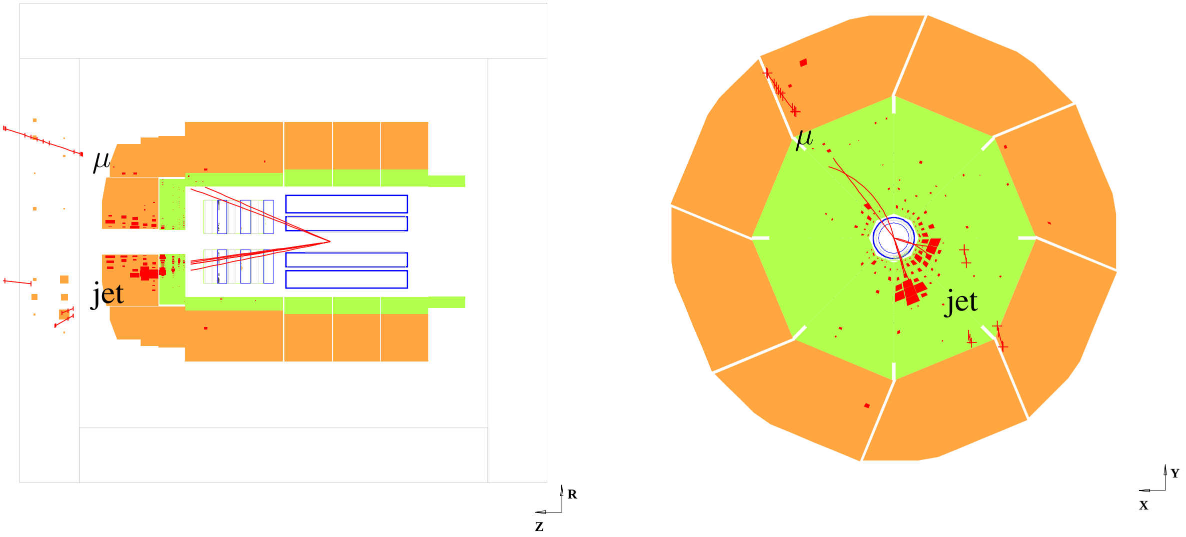

FIGURE A.1: Event display of an $e^{-}p$ data event after the isolated muon selection. The muon is flagged as *isolated*, because the adjacent lower-p_T track is not an inner track but forward. It fails the final selection criteria.

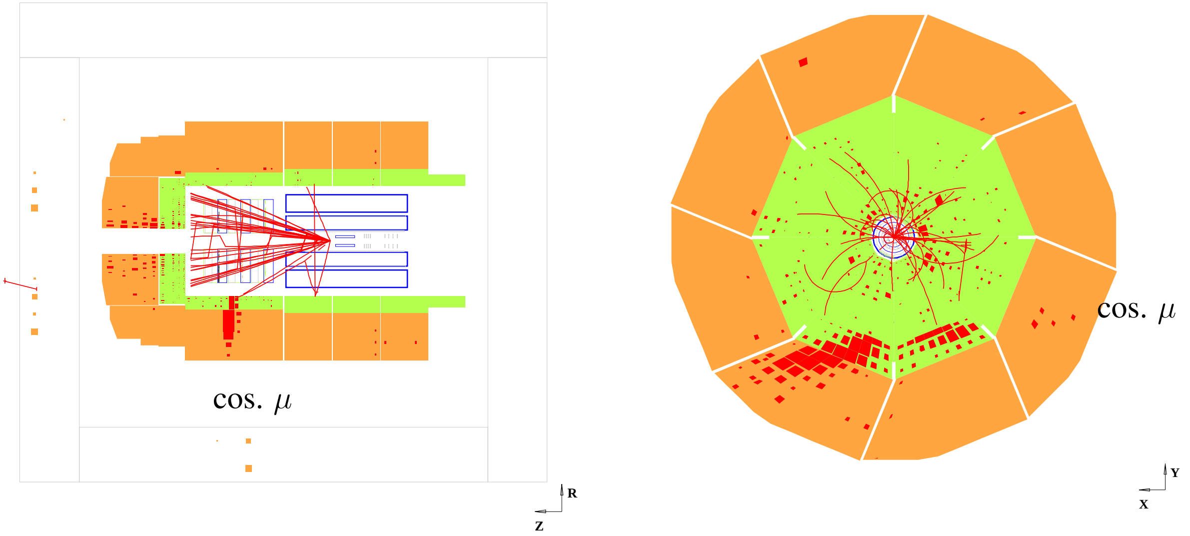

FIGURE A.2: Event display of an e^-p data event after the isolated muon selection. A cosmic muon showering in the LAr calorimeter is laid over an e^-p event. This event is cut in the final selection.

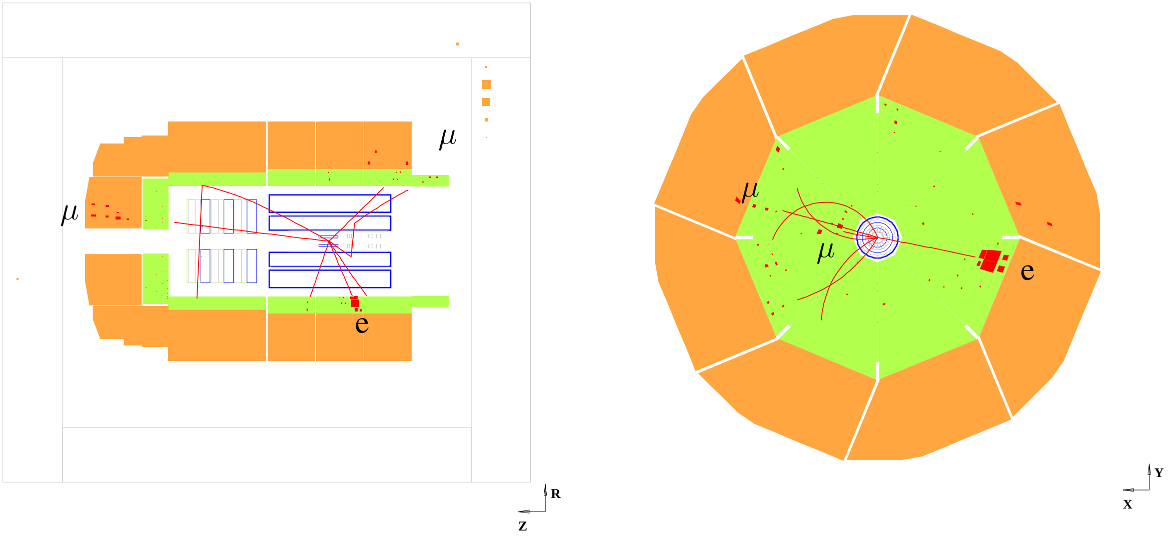

FIGURE A.3: Event display of an elastic $e^-p \rightarrow e\mu\mu X$ data event after the isolated muon selection. The forward muon is not detected by the muon system but has a characteristic calorimeter signature. As the proton remains intact and escapes the detector via the forward beam pipe punch through, the muons balance the transverse momentum of the electron.

Appendix B

Track quality criteria

Lee West track quality criteria		
forward	central	combined
$p_T > 1\,\mathrm{MeV}$	$p_T > 120\,\mathrm{MeV}$	$p_T > 120\,\mathrm{MeV}$
$6^\circ < \theta < 25^\circ$	$20^\circ < \theta < 160^\circ$	$0^\circ < \theta < 40^\circ$
$R_0 \leq 10\,\mathrm{cm}$	$\lvert\mathrm{dca}'\rvert \leq 2\,\mathrm{cm}$	$\lvert\mathrm{dca}'\rvert \leq 5\,\mathrm{cm}$
$\chi^2_{\mathrm{dtnv}} \leq 10$	$R_{\mathrm{start}} \leq 50\,\mathrm{cm}$	$R_{\mathrm{start}} \leq 50\,\mathrm{cm}$
$\chi^2_{\mathrm{dtra}} \leq 25$	$R_{\mathrm{length}} \leq 10\,\mathrm{cm}\;\forall\,\theta \leq 150^\circ$	$R_{\mathrm{length}} \geq 0\,\mathrm{cm}$
$n_{\mathrm{PrimSecPlanSeg}} \geq 1$	$R_{\mathrm{length}} \leq 5\,\mathrm{cm}\;\forall\,\theta > 150^\circ$	$\Delta p/p \leq 99999.9$
$n_{\mathrm{PlanRadSeg}} \geq 2$	$n_{\mathrm{CJC-hits}} \geq 0$	$n_{\mathrm{CJC-hits}} \geq 0$
$\Delta p/p \leq 9999.9$		$\chi^2_{\mathrm{dtra}} \leq 50$
$p \geq 0.5\,\mathrm{GeV}$		$\chi^2_{\mathrm{cent.-forw.}} \leq 50$

TABLE B.1: *Lee West* track quality criteria. For the details and definitons of the variables see [52].

List of Figures

List of Tables

Bibliography

[1] R. Rückl W. Buchmüller and D. Wyler. *Leptoquarks in lepton-quark collisions*. Phys. Lett. B **191** (1987) 442.

[2] S. Eidelman *et al.* [Particle Data Group]. *Searches for Higgs Bosons*. Phys. Lett. B **592** (2004) 1.

[3] M. Kobayashi and T. Maskawa [Kyoto U.]. *CP violation in the renormalizable theory of weak interaction*. Prog. Theor. Phys. **49** (1973) 652-657.

[4] R. Barate *et al.* [LEP Working Group for Higgs boson searches]. *Search for the Standard Model Higgs Boson at LEP*. Phys. Lett. B **565** (2003) 61.

[5] Z. Maki, M. Nakagawa, and S. Sakata. *Remarks on the Unified Model of Elementary Particles*. Prog. Theor. Phys. **28** (1962) 870.

[6] Y. Fukuda *et al.* [Super-Kamiokande Collaboration]. *Evidence for oscillation of atmospheric neutrinos*. Phys. Rev. Lett. **81** (1998) 1562 [hep-ex/9807003].

[7] Q.R. Ahmad *et al.* [SNO Collaboration]. *Direct Evidence for Neutrino Flavor Transformation from Neutral-Current Interactions in the Sudbury Neutrino Observatory*. Phys. Rev. Lett. **89** (2002) 011301 [nucl-ex/0204008].

[8] X.Y. Pham. *Lepton flavor changing in neutrinoless τ decays*. Eur. Phys. J. C **8** (1999) 513.

[9] R.P. Feynman. *Very high-energy collisions of hadrons*. Phys. Rev. Lett. **23** (1969) 1415.

[10] D.J. Gross. *The discovery of asymptotic freedom and the emergence of QCD*. Int. J. Mod. Phys A **20** (2005) 5717.

[11] C.G. Callan and D.J. Gross. *High-energy electroproduction and the constitution of the electric current*. Phys. Rev. Lett. **22** (1969) 156.

[12] A. Dubak. *Measurement of the e^+p Neutral Current DIS Cross Section and the F_2, F_L, xF_3 Structure Functions in the H1 Experiment at HERA*. Dissertation, Techn. Univ. München, Germany (2003).

[13] C. Adloff *et al.* [H1 Collaboration]. *Measurement and QCD Analysis of Neutral and Charged Current Cross Sections at HERA*. Eur. Phys. J. C **30** (2003) 1 [hep-ex/0304003].

[14] A.D. Martin *et al. Parton distributions incorporating QED contributions*. Eur. Phys. J. C **65** (2005) [hep-ph/0411040].

[15] J. Pumplin *et al.* [CTEQ Collaboration]. *New Generation of Parton Distributions with Uncertainties from Global QCD Analysis*. JHEP 0207 (2002) 012 [hep-ph/0201195].

[16] J.C. Pati and A. Salam. *Lepton Number as the Fourth Color*. Phys. Rev. D **11** (1974) 275.

[17] G.G. Ross. *Grand Unified Theories*. Benjamin/Cummings (1984) [ISBN 0-8053-6967-8].

[18] H. Georgi and S.L. Glashow. *Unity of all elementary particle forces*. Phys. Rev. Lett. **32** (1974) 438.

[19] P. Langacker. *Grand Unified Theories and Proton Decay*. Phys. Rep. **72** (1981) 185.

[20] S. Dimopoulos and L. Susskind. *Mass without Scalars*. Nucl. Phys. B **155** (1979) 237.

[21] S. Dimopoulos. *Technicolored Signatures*. Nucl. Phys. B **168** (1980) 69.

[22] E. Farhi and L. Susskind. *A Technicolored GUT*. Phys. Rev. D **20** (1979) 3404.

[23] E. Farhi and L. Susskind. *Technicolor*. Phys. Rep. **74** (1981) 277.

[24] B. Schrempp and F. Schrempp. *A Confining* $SU(2)_L \times SU(2)_R$ *Gauge Model of the Weak Interactions*. Nucl. Phys. B **231** (1984) 109.

[25] L.F. Abbott and E. Farhi. *Are the Weak Interactions strong?* Phys. Lett. B **101** (1981) 69.

[26] J. Wudka. *Composite Leptoquarks*. Phys. Lett. B **167** (1986) 337.

[27] M. Leurer. *New Bounds on Leptoquark Couplings*. Phys. Rev. Lett. **71** (1993) 1324 [hep-ph/9304211].

[28] M. Leurer. *Bounds on Vector Leptoquarks*. Phys. Rev. D **50** (1994) 536 [hep-ph/9312341].

[29] O. Shanker. $\pi l2$*,* $Kl3$ *and* $K^0 - \bar{K}^0$ *Constraints on Leptoquarks and Supersymmetric Particles*. Nucl. Phys. B **204** (1982) 375.

[30] S.P. Martin. *A supersymmetry primer*. Ed. G.L. Kane, Perspectives on supersymmetry, (1997) 1 [hep-ph/9709356].

[31] M. Ahmed *et al.* [MEGA Collaboration]. *Search for the Lepton Family Number Nonconserving Decay* $\mu^+ \to e^+\gamma$. Phys. Rev. D **65** (2005) 112002 [hep-ex/0111030].

[32] B. Aubert *et al.* [BABAR Collaboration]. *Search for Lepton Flavor Violation in the Decay* $\tau^\pm \to e^\pm\gamma$. Phys. Rev. Lett. (2005) [hep-ex/0508012].

[33] B. Aubert *et al.* [BABAR Collaboration]. *Search for Lepton Flavor Violation in the Decay* $\tau^\pm \to \mu^\pm\gamma$. Phys. Rev. Lett. **95** (2005) 041802 [hep-ex/0502032].

[34] S. Davidson, D.C. Bailey, and B.A. Campbell. *Model Independent Constraints on Leptoquarks from Rare Processes*. Z. Phys. C **61** (1994) 613 [hep-ph/9309310].

[35] E. Gabrielli. *Model Independent Constraints on Leptoquarks from Rare Muon and Tau Lepton Processes*. Phys. Rev. D **62** (2000) 055009 [hep-ph/9911539].

[36] I. Abt *et al.* [H1 Collaboration]. *The H1 Detector at HERA*. Nucl. Instrum. Meth. A **386** (1977) 310.

[37] I. Abt *et al.* [H1 Collaboration]. *The tracking, calorimeter and muon detectors of the H1 experiment at HERA*. Nucl. Instrum. Meth. A **386** (1997) 348.

[38] B.H. Wiik *et al.* [DESY Collaboration]. *Evidence for a new resonance PC and other recent results obtained at DORIS using DASP*. In Erice 1975, proceedings, New Phenomena In Subnuclear Physics, Part B*, New York 1977, 635-662.

[39] D.P. Barber *et al.* [DESY Collaboration]. *Discovery of three jet events and a test of quantum chromodynamics at PETRA energies*. Phys. Rev. Lett. **43** (1979) 830.

[40] B. Andrieu *et al.* [H1 Calorimeter Group]. *Beam tests and calibration of the H1 liquid argon calorimeter with electrons*. Nucl. Instrum. Meth. A **350** (1994) 57.

[41] B. Andrieu *et al.* [H1 Calorimeter Group]. *Results from pion calibration runs for the H1 liquid argon calorimeter and comparisons with simulations*. Nucl. Instrum. Meth. A **336** (1993) 499.

[42] R. Brun and F. Carminati. *GEANT Detector Description and Simulation Tool*. Cern Program Library W5013 (1993).

[43] E. Chabert *et al.* [CPPM Marseille]. *QBGFMAR: An updated PHAN Package for Cosmic and Halo Muon Topological Rejection in High* P_T *Physics Analysis*. H1 internal notes H1-IN/98-556 (1998).

[44] I. Negri *et al.* [CPPM Marseille]. *A Minimal Comprehensive Set of Muon Background Topological Finders for High* P_T *Physics Analysis*. H1 internal notes H1-IN/96-498 (1996).

[45] C. Veelken [Liverpool University]. *H1NonepBgFinder - Rejection of Cosmic Muon and Beam-Halo Events in the H1OO Framework*. H1 internal notes H1-IN/02-603 (2002).

[46] M. Ismail. *A Search for the Lepton Favour Violation Process $e \rightarrow \mu$ via Leptoquarks in $e^{\pm}p$ Scattering with the H1 Detector at HERA*. Dissertation, Univ. Manchester, UK (2005).

[47] C. Adloff *et al.* [H1 Collaboration]. *Measurement of Neutral and Charged Current Cross Sections in Electron-Proton Collisions at high Q^2*. Eur. Phys. J. C **19** (2001) 269 [hep-ex/0012052].

[48] B. Leissner. *Muon Pair Production in Electron-Proton Collisions*. Dissertation, RWTH Aachen, Germany (2002).

[49] B. Heinemann. *Measurement of Charged Current and Neutral Current Cross Sections in Positron-Proton Collisions at $\sqrt{s} = 300\,\mathrm{GeV}$*. Dissertation, Univ. Hamburg, Germany (1999).

[50] P. Bruel. *Recherches d'interactions au-delà du Modèle Standard á HERA*. Dissertation, LLR - École Polytechnique, Palaiseau, France (1998).

[51] C. Adloff *et al.* [H1 Collaboration]. *Measurement of Neutral and Charged Current Cross-Sections in Positron-Proton Collisions at Large Momentum Transfer*. Eur. Phys. J. C **13** (2000) 609 [hep-ex/9908059].

[52] The H1 OO group. *The H1 OO Physics Analysis Project*. Available on the www: https://h1web01.desy.de/icas/oop/current/oo.ps.gz (2005).

[53] M. Peez *et al.* [CPPM Marseille]. *An energy flow algorithm for Hadronic Reconstruction in OO: Hadroo2*. H1 internal notes H1-IN/05-616 (2005).

[54] J.M. Butterworth *et al.* *KTJET: A C++ implementation of the k-perpendicular clustering algorithm*. Comput. Phys. Commun. **153** (2003) 85 [hep-ph/0210022].

[55] S.D. Ellis and D.E. Soper. *Successive Combination Jet Algorithm For Hadron Collisions*. Phys. Rev. D **48** (1993) 3160 [hep-ph/9305266].

[56] M.H. Seymour. *Jets in QCD*. 10th Topical Workshop on Proton-Antiproton Collider Physics, Batavia, IL, May 9-13, 1995 [hep-ph/9506421].

[57] S. Bentvelsen *et al.* *Reconstruction of (x, Q^2) and extraction of structure functions at HERA*. Physics at HERA vol. 1, W. Buchmüller and G. Ingelmann (eds.), Hamburg (1991).

[58] H. Jung. *Hard Diffractive Scattering in High-Energy ep Collisions and the Monte Carlo Generation RAPGAP*. Comput. Phys. Commun. **86** (1995) 147.

[59] T. Sjöstrand. *The Lund Monte Carlo for Jet Fragmentation and e^+e^- Physics: JETSET Version 6.2*. Comput. Phys. Commun. **39** (1986) 347.

[60] H. Spiesberger. *HERACLES and DJANGOH: Event generation of ep Interactions at HERA Including Radiative Processes*. Available on the www: http://wwwthep.physik.uni-mainz.de/∼hspiesb/djangoh/djangoh_m.4.6.6.ps.gz.

[61] G. Gustafson and U. Pettersson. *Dipole Formulation of QCD Cascades*. Nucl. Phys. B **306** (1988) 746.

[62] B. Andersson *et al. Coherence Effects in Deep Inelastic Scattering*. Z. Phys. C **43** (1989) 625.

[63] T. Sjöstrand. *High-energy Physics Event Generation with Pythia 5.7 and Jetset 7.4*. Comp. Phys. Comm. **82** (1994) 74.

[64] M. Glück *et al.* [Univ. Dortmund]. *Photonic Parton Distributions*. Phys. Rev. D **46** (1992) 1973.

[65] C. Adloff *et al.* [H1 Collaboration]. *Measurement of Dijet Cross Sections in Photoproduction at HERA*. Eur. Phys. J. C **25** (2002) 13 [hep-ex/0201006].

[66] U. Baur *et al. Electroweak Vector Boson Production in High-Energy ep Collisions*. Nucl. Phys. B **375** (1992) 3.

[67] K. Rosenbauer. *Suche nach Leptoquarks und Leptogluonen im H1-Experiment bei HERA*. Dissertation, RWTH Aachen, Germany (1995).

[68] G. Altarelli and G. Parisi. *Asymptotic Freedom in Parton Language*. Nucl. Phys. B **126** (1977) 298.

[69] V.N. Gribov and L.N. Lipatov. *Deep Inelastic ep Scattering in Perturbation Theory*. Sov. J. Nucl. Phys.**15** (1972) 438.

[70] Y.L. Dokshitzer. *Calculation of the Structure Functions for Deep Inelastic Scattering and e^+e^- Annihilation by Perturbation Theory in Quantum Chromodynamics*. Sov. Phys. JETP **46** (1977) 641.

[71] A. Aktas *et al.* [H1 Collaboration]. *Search for Leptoquark Bosons in ep collisions at HERA*. Phys. Lett. B **629** (2005) 9 [hep-ex/0506044].

[72] M. Botje. *A QCD analysis of HERA and fixed target structure function data*. Eur. Phys. J. C **14** (2000) 285 [hep-ph/9912439].

[73] S. Chekanov *et al.* [ZEUS Collaboration]. *Search for lepton-flavor violation at HERA*. Eur. Phys. J. C **44** (2004) 463 [hep-ex/0501070].

[74] C. Adloff *et al.* [H1 Collaboration]. *A Search for Leptoquark Bosons and Lepton Flavor Violation in Positron-Proton Collisions at HERA*. Eur. Phys. J. C **11** (1999) 447 [Erratum-ibid. C **14** (2000) 553] [hep-ex/9907002].

[75] M. Reece and H. Frisch. *Using Track Impact Parameter to Distinguish Hadronically-Decaying Taus in Top Quark Decays from Light Quark Jets*. CDF Note: CDF/ANAL/TOP/CDFR/6203 (2002).

[76] A. Aktas *et al.* [H1 Collaboration]. *Measurement of $F_2^{c\bar{c}}$ and $F_2^{b\bar{b}}$ at Low Q^2 and x using the H1 Vertex Detector at HERA*. Eur. Phys. J. C **45** (2006) 23 [hep-ex/0507081].

[77] A. Aktas *et al.* [H1 Collaboration]. *Measurement of Charm and Beauty Dijet Cross Sections in Photoproduction using the H1 Vertex Detector at HERA*. submitted to Eur. Phys. J. (2006) [hep-ex/0605016].

[78] C. Veelken. *Search for Events with Isolated Leptons and Large Missing Transverse Momentum in ep Collisions at HERA*. Dissertation, Univ. Liverpool, UK (2006).

[79] A. Aktas *et al.* [H1 Collaboration]. *Tau Lepton Production in ep Collisions at HERA*. DESY 06-029, submitted to Eur. Phys. J. (2006) [hep-ex/0604022].

[80] R.O. Duda *et al.* *Pattern Classification*. Wiley Interscience (2^{nd} Ed.), New York, US (2000) ISBN: 0-471-05669-3.

[81] R. Sedgewick. *Algorithms in C++*. Addison Wesley Professional, Boston, US (1992) ISBN: 0-201-51059-6.

[82] P. De Wilde. *Neural Network Models: Theory and Projects (Communications & Control Engineering)*. Springer-Verlag, Berlin, Germany (1997) ISBN: 3-540-76129-2.

[83] G. Zech. *Frequentist and Bayesian Confidence Intervals*. Eur. Phys. J. direct C **4** (2002) 12 [hep-ex/0106023].

[84] A.L. Read. *Optimal statistical analysis of search results based on the likelihood ratio and its application to the search for the MSM Higgs boson at $\sqrt{s} = 161$ and $172\,\mathrm{GeV}$*. DELPHI 97-158 PHYS 737 (1997) [http://hep.fuw.edu.pl/delphi/higgs/link_delphi.html].

[85] A. Aktas *et al.* [H1 Collaboration]. *Search for Squark Production in R-Parity Violating Supersymmetry at HERA*. Eur. Phys. J. C **36** (2004) 425 [hep-ex/0403027].

[86] J. Haller. *Search for Squark Production in R-Parity Violating Supersymmetry at HERA*. Dissertation, Univ. Heidelberg, Germany (2003).

[87] G.J. Feldman and R.D. Cousins. *A Unified Approach to the Classical Statistical Analysis of Small Signals*. Phys. Rev. D **57** (1998) 3873 [physics/9711021].

[88] C. Genta. *Search for new physics in events with high-p_T leptons at HERA*. Dissertation, Univ. Firenze, Italy (2005).

[89] P. Bock. *Computation of Confidence Levels for Exclusion or Discovery of a Signal with the Method of Fractional Event Counting*. e-Print (2004) [hep-ex/0405072].

[90] V.M. Abazov *et al.* [DØ Collaboration]. *Search for Pair Production of Second Generation Scalar Leptoquarks in $p\bar{p}$ Collisions at $\sqrt{s} = 1.96\,\mathrm{TeV}$*. Phys. Lett. B **636** (2006) 183 [hep-ex/0601047].

[91] D. Acosta *et al.* [CDF Collaboration]. *Search for Third Generation Vector Leptoquarks in Run II*. CDF Preliminary http://www-cdf.fnal.gov/physics/exotic/r2a/20060323.3genvlq.

[92] G. Abbiendi *et al.* [OPAL Collaboration]. *Search for pair-produced leptoquarks in e^+e^- interactions at $\sqrt{s} = 189 - 209\,\mathrm{GeV}$*. Eur. Phys. J. C **31** (2003) 281 [hep-ex/0305053].

[93] G. Abbiendi *et al.* [OPAL Collaboration]. *Tests of the Standard Model and Constraints on New Physics from Measurements of Fermion-pair Production at $183\,\mathrm{GeV}$ at LEP*. Eur. Phys. J. C **6** (1999) 1 [hep-ex/9808023].

Danke! - Thanks! - Merci! Grazie! - Gracias! - Спасибо!

This thesis would not have been possible without the kind support of many people I am much obliged to at this point.

The first person to thank is my advisor Prof. Dr. Ulrich Straumann who gave me the opportunity to work on this subject in form of a thesis at the University of Zürich. His helpful advice, fair comment and remarkable patience are essential for this work.

I thank Prof. Dr. Peter Truöl for the employment in his working group and for taking the chair at the conferral of the doctorate.

My sincere thanks also go to Dr. Emmanuelle Perez, who is indisputably one of the best experimental physicists in this field, for valuable discussions and her external expert's report.

Special thanks go to my H1 working group of the University of Zürich, namely Prof. Dr. Ulrich Straumann, Dr. Katharina Müller, Dr. Stefania Xella-Hansen, Dr. Stefan Schmitt, Dr. Max Urban, Krzysztof Nowak and Carsten Schmitz. In weekly video conferences, office discussions and quite some hours in the experimental hall we have solved one problem after another together as a team. In particular, I am much obliged to Dr. Stefan Schmitt whose work and ideas are essential for our successful CIP2K project and which have also a significant impact on this thesis.

For proof-reading and the best humour in the H1 collaboration I thank my English colleagues Dr. Paul Laycock and Dr. David South.

The work with all the scientists at the H1 experiment is very enjoyable, in particular with the *Rare and Exotics* working group chaired by Dr. Emmanuel Sauvan, Dr. André Schöning, Dr. Cristinel Diaconu and Dr. Martin Wessels.

It is a great pleasure and honour to have the best friends, Dr. Johannes Haller, Lars Finke and Carsten Schmitz around day by day.

For her love and understanding I kiss Julia Biallas.

I thank my parents and my family for their everlasting support and trust they put in me whatever weird stuff I am working on.

This work has been supported by the Swiss National Science Foundation.

Curriculum Vitae

PERSÖNLICHE DATEN

Name:	Linus Lindfeld
Geburtsdatum:	2. Februar 1976 in Münster/Westf., Deutschland
Familienstand:	ledig
Staatsangehörigkeit:	deutsch

BILDUNGSWEG

Aug 86 - Mai 95	Hittorf-Gymnasium, Münster/Westf., Abschluss: Abitur
Aug 95 - Sep 96	Zivildienst, Malteser Hilfsdienst e.V., Münster/Westf.
Okt 96 - Aug 98	Grundstudium Diplom Physik, RWTH Aachen
Sep 98 - Jul 99	Auslandsstudium Physik, University of Edinburgh, UK
Aug 99 - Sep 99	Forschungspraktikum, Fraunhofer IAF, Freiburg *Aufbau und Inbetriebnahme von Messapparaturen zur elektro-optischen Charakterisierung GaN-basierender LEDs und Diodenlaser*
Okt 99 - Mär 01	Hauptstudium Diplom Physik, RWTH Aachen
Apr 01 - Apr 02	Diplomarbeit, DESY Hamburg Prof. Dr. Ch. Berger, I. Phys. Inst. RWTH Aachen *Untersuchungen zur Elektronenstreuung bei sehr kleinen Impulsüberträgen*
Mai 02	Studienabschluss Diplom Physik, RWTH Aachen
Feb 03 - Aug 06	Promotion, Universität Zürich/DESY Hamburg Prof. Dr. U. Straumann, Phys. Inst. Universität Zürich *Search for lepton flavour violation with the H1 experiment at HERA*

Hamburg, den 25. Oktober 2006